Maximal Use of Kinematic Information for the Extraction of the Mass of the Top Quark in Single-lepton $t\bar{t}$ events at DØ.

by
Juan Cruz Estrada Vigil

Submitted in Partial Fulfillment
of the
Requirements for the Degree
Doctor of Philosophy

Supervised by
Professor Thomas Ferbel

Department of Physics
The College
Arts and Sciences
University of Rochester Rochester, New York

2001

To my wife, Daniela.

Curriculum Vitae.

The author was born in Buenos Aires, Argentina on August 21, 1972. He attended Universidad de Buenos Aires from 1990 to 1993, and later transfered to Instituto Balseiro, in Bariloche Argentina, where he graduated with a Licenciado en Ciencias Fisicas degree in 1997 after finishing his Lic. thesis in cosmology. Juan Estrada joined the University of Rochester in the spring of 1998 and began graduate studies in Experimental High Energy Physiscs at Fermilab on the DØ experiment. He received a Marshak Fellowship in 1998. He collaborated in the upgrade of the DØ detector for Run II of the Tevatron, working on the Visible Light Photon Counter (VLPC) system used to readout the Central Fiber Tracker and the Preshower detectors. He also contributed to the development of the Level-3 trigger tool for electron identification at DØ. His Ph.D. research is based on an analysis of data from Run I of the Tevatron for a new measurement of the mass of the top quark. It was performed under the direction of Professor Thomas Ferbel and supervised at Fermilab by Dr. Gaston Gutierrez. Estrada received a Master of Arts degree in June 2000.

Acknowledgements.

I thank the University of Rochester for giving me the opportunity to work at Fermilab and to learn about Experimental High Energy Physics. The University has been very helpful making my life, and the life of my wife, easier during our stay at Rochester and in Batavia, Il. Tom Ferbel has been an excellent person to deal with, helping me in all the academic field and other issues. I am extremely fortunate to have had the benefit of his guidance and support. I also thank all the Rochester group at DØ for giving me the support a student needs in such a large experiment.

This analysis would have been impossible without all the great work done by the people responsible of the previously published measurement of the mass of the top quark. I thank specially Scott Snyder and Frank Hsieh for their theses and the extensive documentation of their analysis.

Many colleagues took the time to explain to me the basic and not-so-basic ideas about the experiment, physics and hardware issues. George Ginther, who mentored me from the very beginning and gave me my first view of the experiment, Stefan Gruenendahl, Marek Zielinski, Vishnu Zutshi, Erik Ramberg, Volker Buescher, Jadzia Warchol, and more, from whom I have learned. I thank all of them.

I especially thank Gaston Gutierrez, who in the summer of 1999 started spending

time teaching me about hardware and then shared with me a brilliant idea that formed the basis of this thesis.

Thanks to my saintly wife Daniela, who at this point knows as much about physics as I do, but she does not really like it! It is not easy to be the wife of a foreign graduate student, and it is not easy to be around physicists all the time.

Thanks to my mother, my father, my brothers and my sisters. Without their support from Argentina, their visits to Batavia and their emails, it would have been much harder to complete this work.

I could write for a long while acknowledging help from all my friends at Fermilab, but I do not expect them to read this thesis, I will rather thank them personally. I am sure that will be more fun.

Abstract.

The mass of the top (t) quark has been measured in the lepton+jets channel of $t\bar{t}$ final states studied by the DØ and CDF experiments at Fermilab using data from Run I of the Tevatron $p\overline{p}$ collider. The result published by DØ is 173.3 $\pm$ 5.6(stat) $\pm$ 5.5(syst) GeV. We present a different method to perform this measurement using the existing data. The new technique uses all available kinematic information in an event, and provides a significantly smaller statistical uncertainty than achieved in previous analyses. The preliminary results presented in this thesis indicate a statistical uncertainty for the extracted mass of the top quark of 3.5 GeV, which represents a siginificant improvement over the previous value of 5.6 GeV. The method of analysis is very general, and may be particularly useful in situations where there is a small signal and a large background.

Contents

1 Introduction. **1**

1.1 The Experiment. 1

1.2 Production and Detection of the Top Quark. 3

1.3 Measurement of the Mass of the Top Quark. 4

2 Top Quark **6**

2.1 The Top Quark in the Standard Model. 8

2.2 Mass of the Top Quark and Other Electroweak Parameters. 10

3 Fermilab and DØ **13**

3.1 The accelerator and the beam. 13

3.2 The DØdetector. 19

3.3 Coordinates system. 20

3.4 The Central Tracker 22

3.4.1 Drift Chambers 23

3.4.2 Transition Radiation Detector (TRD). 26

3.5 The Calorimeter. 28

3.5.1 Central and End Calorimeters. 33

3.6 Muon Spectrometer. 33

4 Reconstruction and Particle Identification 39

4.1 Electron Identification. 40

4.1.1 Candidate Construction. 40

4.1.2 Covariance Matrix χ^2 41

4.1.3 Isolation. 43

4.1.4 Significance of a Track-match. 44

4.1.5 Track Ionization. 44

4.1.6 Kinematic Criteria and Summary. 45

4.1.7 Electron Energy Corrections. 45

4.2 Muon Identification. 46

4.2.1 Reconstruction of Muon Trajectory. 46

4.2.2 Impact Parameters. 47

4.2.3 Cosmic Ray Veto. 48

4.2.4 Track Timing. 48

4.2.5 Hit Multiplicity. 49

4.2.6 Isolation and Confirmation in the Calorimeter. 49

4.2.7 Kinematic Criteria and Summary. 49

4.3 Jet Reconstruction. 50

4.3.1 Jet Energy Corrections. 51

5 Mapping Between Jet and Parton Energies. 57

5.1 Transfer function and production probability. 58

5.2 Parameterization of the transfer functions. 60

5.3 Test of the Transfer Function. 62

6 The Method of Analysis. 71

6.1 Introduction. 71

6.2 The General Method. 73

6.2.1 Definition of Extended Likelihood. 73

6.2.2 Detector Acceptance Corrections. 77

6.2.3 Normalizing $\boldsymbol{P(x)}$ 80

6.2.4 Maximum Likelihood for Signal and Background 81

6.3 General Calculation of $\boldsymbol{P(x)}$ 82

6.4 Calculation for Single-Lepton $\boldsymbol{t\bar{t}}$ Events 85

6.4.1 The Matrix Element $|\boldsymbol{M}|^{\mathbf{2}}$ 86

6.4.2 The Measurement Probability $\boldsymbol{W(y,x)}$ 89

6.4.3 The Phase Space 90

6.4.4 Calculation of P(x) for $\boldsymbol{t\bar{t}}$ Events 93

7 Performace of the Method in Simulated Experiments. 95

7.1 MC Samples Defined in this Analysis. 95

7.2 Event simulation. 98

7.3 Test of Linearity. 99

7.4 Ensemble Tests with Sample 1. 101

7.5 Ensemble Tests with Sample 2. 106

7.6 Esemble Tests with Sample 1 and Transfer Functions. 108

7.7 Measurement of the Mass of the W boson. 110

8 Conclusions 115

A Understanding the improvement in the calculation of the top-quark mass using the full matrix element 119

A.1 Introduction 119

A.2 The model. 120

A.3 Two possible paths for the analysis. 120

A.4 The result. 122

A.5 Conclusion. 122

B Phase Space Calculation for Single Lepton $t\bar{t}$ Events **127**

Bibliography **132**

List of Figures

1.1 Quark and an antiquark can annihilate to produce a gluon, which in turn breaks up into a different quark-antiquark pair, in this case a $t\bar{t}$ pair. 3

2.1 The three generations of quarks and leptons in the Standard Model. . 7

2.2 Leading order diagrams for $t\bar{t}$ production. 9

2.3 Decay of the top (t) quark into a W boson and a bottom (b) quark. . 10

2.4 Electroweak precision measurements [6]. The straight lines corrspond to different choices for the Higgs mass in the S.M. 12

3.1 Schematic of the accelerator complex 15

3.2 Schematic of DØ, a multipurpose detector assembled to investigate $p\bar{p}$ collisions at the Tevatron. 21

3.3 Schematic of the DØcentral tracker. 23

3.4 The r-ϕ view of a quadrant of the Vertex Drift Chamber (VTX). . . . 25

3.5 Schematic of the FDC. Two Θ modules with a Φ module in between. 27

3.6 Schematic of the DØcalorimeter 31

3.7 Side view of the DØcalorimeters. Rays of fixed η relative to the center of the detector are given in the sketch. 34

3.8 Unit cell in the DØcalorimeter. 35

3.9 Muon Spectrometer in the DØdetector. 36

4.1 Effect of the out-of-cone radiation. The reconstructed jets have on average less energy than the original parton, this is the motivation for the out-of-cone corrections, which are based on the comparison of parton energies and energies of reconstructed jets in $t\bar{t}$ events (circles). The correction attempts to provide a 1:1 correspondence (given by the dashed line). 52

4.2 Dependence of the deviation in the jet energy scale (ΔS) for γ+jets data and $t\bar{t}$ MC events, as a function of $|\eta|$ [45]. 55

5.1 Distributions in $\delta_E = E_{jet} - E_{parton}$ for different parton energy ranges (E range 1: 15 GeV $< E_{parton} <$ 60 GeV, E range 2: 60 GeV $< E_{parton} <$ 100 GeV, E range 3: 100 GeV $< E_{parton} <$ 140 GeV, for jets in $t\bar{t}$ event with $0.2 < |\eta| < 0.6$). The distributions have an extended tail for $\delta_E < 0$, which corresponds to the effect of hadronization and radiation. 59

5.2 Top: lego plot of E_{parton} vs E_{jet} for a sample of jets associated with partons in $t\bar{t}$ Monte Carlo events, using full DØdetector simulation (CAFIX corrections included). Bottom: lego plot of E_{parton} vs E_{jet}), where E_{parton} is predicted using $n(E_{parton})$ and the transfer function described in Eq.(5.2). The jets are in the region of $0.2 < |\eta| < 0.6$. 63

5.3 Contour plots corresponding to Figure 5.2. The different shadings correspond to different number of events (40, 30, 20, 10 and 5). 64

5.4 Slices of E_{jet} from the plots in Figure 5.2. The filled histogram correspond to predictions using $n(E_{parton})$ and the transfer function, and the lines correspond to the original MC simulated events. 65

5.5 Same as Figure 5.4, but now the slices in E_{parton} 66

5.6 Slices in E_{jet}, same plots as in Figure 5.4, but now for jets in the region $1.3 < |\eta| < 2.0$. 67

5.7 Distribution of the invariant mass of three jets with full DØsimulation and CAFIX energy corrections (jets identified in Monte Carlo as coming from the hadronic decay of the top quark) is compared with the prediction from the transfer function. The comparison is done for events simulated with m_t=160 GeV. The mean and RMS values correspond to the hatched histogram. 69

5.8 Same as Figure 5.7, but now m_t=175 GeV. 70

7.1 Most probable values of the mass of the top quark obtained for simulated experiments of 1000 events, generated with a m_t=160, 175 and 190 GeV. The standard DØjet energy corrections were used in this study. 100

7.2 Most probable values of the mass of the top quark obtained for simulated experiments of 1000 events, generated with a m_t=160, 170, 175, 180 and 190 GeV. The complete transfer functions were used in this study. 102

7.3 -ln(Likelihood) for 4 Monte Carlo experiments with 24 signal events and 40 background events, all generated at $M_t = 175$ GeV. The numbers in parentheses indicate the most probable value of the mass of the top quark for each experiment. The x-axis on the plots has been offset to give the minimum always around $x = 0$ and a constant was subtracted to the likelihood function for convenience. 103

7.4 Esemble tests with Sample 1. The upper plot shows the results for the most probable mass extracted in different MC experiments, and lower plot shows the pull distribution in the mass. 105

7.5 Esemble test with Sample 1. The displayed statistical uncertainty is obtained from the width of the likelihood for each experiment. 106

7.6 Esemble test with Sample 2. The upper plot shows the results of the most probable mass obtained in different experiments, and the lower plot shows its pull distribution. 107

7.7 Esemble test with Sample 2. The displayed statistical error is obtained from the width of the likelihood for each experiment. 109

7.8 Esemble tests with Sample 1 using the transfer functions to account for the hadronization process. The hatched histogram is the distribution of most probable masses for each experiment, the Gaussian curve fitted to this distribution has a σ=5.5 GeV and is also shown here. The other Gaussian in the plot, with σ=8.0 GeV and the same total area, corresponds to the results obtained in the previous analysis by DØ[45] and is here only to compare the result of this test with those of an equivalent test done for the Neural Network analysis. 111

7.9 Two examples of likelihood as a function of the mass of the W boson in the hadronic channel for a sample of 24 signal $t\bar{t}$ events with no background. 113

7.10 Ensemble tests for the determination of the mass of the W boson in the hadronic branch of the $t\bar{t}$ event. Each experiment is simulated using 24 signal $t\bar{t}$ events and no background, with $M_t = 175$ GeV. . . 114

8.1 Top left(right): Likelihood as a function of $m_t(m_W)$ for 46 e + 4 jets events in the DØRun I data. Bottom left(right): Likelihood as a function of $m_t(m_W)$ for 46 e+4 jets and 41 muon+4 jets events in DØRun I data. 118

A.1 Histrograms of estimators of $< x >$ obtained from 80 samples of 30 events using Method I (top) and Method II (bottom). All events have the same width for their probability distributions. As expected, the plots show no difference between these two procedures. 123

A.2 Histrograms of estimators of $< x >$ obtained from 80 samples of 30 events using Method I (top) and Method II (bottom). The input events have large differences in uncertainties. 124

A.3 Histrograms of estimators of $< x >$ obtained from 80 samples of 30 events using Method I (top) and Method II (bottom). The input events have small differences in uncertainties. 125

B.1 Feymann diagram for the single-lepton $t\bar{t}$ event. 128

Chapter 1

Introduction.

In this chapter we present a brief introduction to the broad ideas that underly this work.

1.1 The Experiment.

The experiment described in this thesis is based on studies performed at a particle accelerator called the Tevatron. It is located in the western suburbs of Chicago at the Fermi National Accelerator Laboratory.

The Tevatron is a wondrous machine. It consists of a ring with a radius of about 1 km, where protons and antiprotons circulate in opposite directions. Protons are the familiar components of the atomic nucleus, and antiprotons are their antimatter

counterparts.

Protons and antiprotons produce collisions inside the Tevatron at two large detectors, each operated by ≈ 400 physicists, who study these collisions. This dissertation is based on research performed at the DØ experiment, one of these collisions.

Protons and antiprotons are not quite elementary particles. They contain quarks that are held together by gluons. Quarks and gluons are the fundamental constituents, and, up to now, there is no evidence that they have additional substructure. This means that when protons and antiprotons collide, all their components (quarks and gluons) can interact.

As we currently understand, there are six kinds of quarks, and each of these quarks has its corresponding antimatter-counterpart antiquark. The six quarks are called up (u), down (d), charm (c), strange (s), top (t), and bottom (b). These quarks have baryon numbers of $\frac{1}{3}$, and electric charges of $+\frac{2}{3}$ (for u, c and t) and $-\frac{1}{3}$ (for d, s and b). Protons are formed of one d and two u quarks, and all the atomic nuclei are formed from these "first generation" kinds of quarks. Antiprotons are formed from anti-u and anti-d (usually written as $\overline{u}$ and $\overline{d}$).

When two constituent particles interact, they can often produce different kinds of particles. For example, a quark and its antiquark can annihilate to produce a gluon, which can in turn break up into a different quark-antiquark pair, as depicted in Figure 1.1. In this way, one can produce different and new kinds of particles from

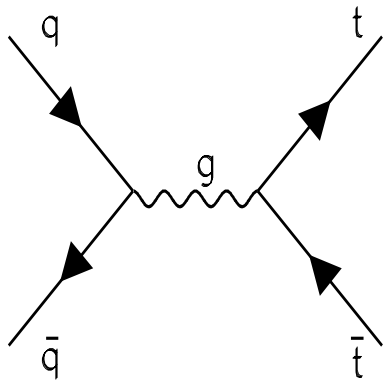

Figure 1.1: Quark and an antiquark can annihilate to produce a gluon, which in turn breaks up into a different quark-antiquark pair, in this case a $t\overline{t}$ pair.

proton-antiproton collisions.

1.2 Production and Detection of the Top Quark.

The production of top quarks is achieved mainly as sketched in Figure 1.1. A quark constituent of the proton and an antiquark constituent of an antiproton can interact to produce a gluon, which in turn produces a t and $\overline{t}$. Because of conservation of electric (and other kinds of) charge, one can usually produce a quark only with its corresponding antiquark (and no other antiquark). Starting from a gluon, one could not produce a pair such as a t and a $\overline{c}$.

Once a $t\overline{t}$ pair is produced, a top quark can be observed in a detector through its decay into a b quark and a W boson. The electrically charged W boson is a particle that can decay into a $q\overline{q}'$ pair (q and q' representing different generic quarks), or

into a charged lepton and a neutrino.

A neutrino is also a fundamental particle (a "lepton"), with no electric charge, that interacts very weakly, and escapes the detector without being observed. There are three types of charged leptons, one of them is the common electron, and the other two are the muon (μ) and the τ.

The signature for a t in the final state is therefore a b quark and a W, where the W decays either into two quarks, or into a charged lepton and a particle that escapes the detector (neutrino).

The DØ detector was designed primarily to observe quarks and the two lighter kinds of leptons (electrons and muons). The neutrino is "observed" as a missing piece in the collision.

1.3 Measurement of the Mass of the Top Quark.

By measuring the energies of the decay products of the top quark, one can determine its rest (or invariant) mass. If the top quark were produced with no kinetic energy (at rest), the sum of the energies of its decay products would equal the mass of the top quark. Unfortunately, this is not the general situation, and certain transformations are needed to account for the movement of the top quark at production, but this involves purely well understood relativistic kinematics.

DØ and the other major Tevatron experiment (CDF) were able to measure the top quark mass with excellent precision. This was very important because the mass of the top quark turned out to be 30 times larger than the next heaviest quark, the b quark. The uncertainty in this measurement was in part due to the small number of $t\bar{t}$ pairs produced at the Tevatron. Of the order of 30 good candidates were observed by DØ. This work is intended to maximize the use of information in this small sample of events, and thereby reduce the uncertainty on the mass measurement.

Chapter 2

Top Quark

As mentioned in the Introduction, there are six quarks known in nature. The quarks are arranged in three pairs of generations, as shown in Figure 2.1. Each member of a pair can be transformed into its partner via the charged-current weak interaction carried by the W boson. Together with the six known leptons (electron, muon, τ and their associated neutrinos, also in Figure 2.1), the six quarks constitute all of the matter in the universe (with the possible exception of the mysterious "dark matter" and "dark energy"). It is therefore essential that we understand the properties of the leptons and quarks in detail.

The top quark was discovered in 1995 at Fermilab by the CDF [1] and DØ [2] experiments using the Tevatron accelerator, a proton antiproton collider with center of mass energy $\sqrt{s} = 1.8$ TeV (the Tevatron is discussed in Chapter 3).

$$\text{Quarks:} \quad \begin{pmatrix} u \\ d \end{pmatrix} \quad \begin{pmatrix} c \\ s \end{pmatrix} \quad \begin{pmatrix} t \\ b \end{pmatrix}$$

$$\text{Leptons:} \quad \begin{pmatrix} \nu_e \\ e^- \end{pmatrix} \quad \begin{pmatrix} \nu_\mu \\ \mu^- \end{pmatrix} \quad \begin{pmatrix} \nu_\tau \\ \tau^- \end{pmatrix}$$

Figure 2.1: The three generations of quarks and leptons in the Standard Model.

The simplest model that describes the properties of quarks and leptons is called the Standard Model (SM) of the strong and electroweak interactions (an updated view of the SM can be found in Ref. [3]). However, the SM merely accommodates these particles and their masses, but does not explain their origin. The top quark is an interesting particle for investigating the origin of mass because it has a mass much larger than the rest of the quarks and leptons. The mystery of this large mass (≈ 174 GeV), with the next heaviest b quark having a mass of only about 5 GeV, almost demands greater study in order to find or unlock other mysteries.

The short lifetime of the top quark (yet to be determined) is another characteristic that provides the possibility for measurement that has no analogue in the other quarks. In contrast to the lightest quarks, which are confined permanently in bound states with other quarks and antiquarks, the top quark decays so quickly that it does not have time to form bound hadronic states (analogous to protons or π mesons). There is also insufficient time prior to the decay to change the spin character of a top quark, and its decays therefore reflects the underlying dynamics.

Thus, the top quark is largely free of many complications associated with the strong interaction, and it presents novel experimental challenges and opportunities that require innovative ideas and techniques.

2.1 The Top Quark in the Standard Model.

The top quark was discovered in data obtained at the Tevatron during Run I, between 1992-1996, in which approximately 100 events/pb of luminosity was collected at the CDF and DØ detectors. The SM suggests that the top quark has a very short lifetime of about 5×10^{-25} s, and it can therefore only be detected indirectly via its decay products.

The most likely means of producing top quarks is through the color (gluon) interaction, and since this strong interaction conserves quark "flavor" quantum numbers, the top quark must be produced in $t\overline{t}$ pairs. The top quark can also be produced singly through the weak interaction, but these kind of processes will not concern us here.

The leading order diagrams for top quark production are shown in Figure 2.2, the two major production channels involve $q\overline{q}$ annihilation and gluon fusion. Because it is more likely for a significant fraction of the proton or antiproton momentum to be carried by a quark than by a gluon, the $q\overline{q}$ channels dominates the production rate

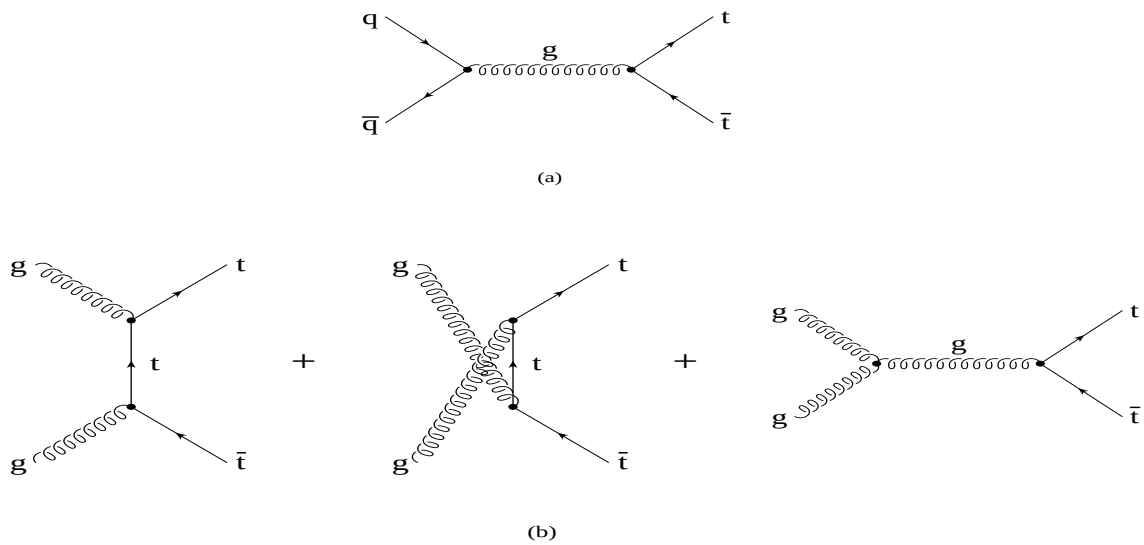

Figure 2.2: Leading order diagrams for $t\overline{t}$ production.

for the relatively massive top quarks at the energy of the Tevatron.

The only interaction that does not conserve quark flavor is the weak interaction, and it is therefore the only route open for top quark decay in the Standard Model. The vertices of relevance are of the type shown in Figure 2.3. For a top mass larger than the W mass, the top quark must decay mainly into a W and a b quark. The b quark fragments and hadronizes, forming a jet of final state particles (mainly π and K mesons). The decay of the W can proceed through any pair of particles forming a quark or lepton doublet (e.g., $W^- \rightarrow e^-\overline{\nu_e}$, $\overline{c}s$, etc., except for the kinematically forbidden $\overline{t}b$ doublet). Because the masses of the particles from W decay are far smaller than the W mass, the probability for decay into any doublet is nearly equal.

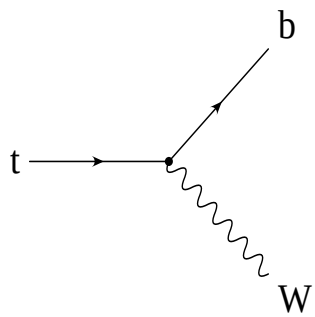

Figure 2.3: Decay of the top (t) quark into a W boson and a bottom (b) quark.

Moreover, because quarks come in three colors, each of the $q\overline{q}$ modes is three times more likely than any of the $l\overline{\nu_l}$ modes.

2.2 Mass of the Top Quark and Other Electroweak Parameters.

This work will describe a new technique to measure the mass of the top quark. The mass has already been measured by the DØ[4] and CDF[5] collaborations to be

$$m_t = 172.1 \pm 7.1 \text{ GeV} \quad (\text{DØ}), \text{ and} \tag{2.1}$$

$$m_t = 176.0 \pm 6.5 \text{ GeV} \quad (\text{CDF}). \tag{2.2}$$

An important issue is what precision should be sought for m_t. One way to address this question is in the context of precision measurements of other electroweak

parameters [6]. These are summarized in Figure 2.4 in a plot of the mass of the W boson (m_W) versus m_t, for different values of the unkown mass of the Higgs boson (m_H). In the Stardard Model, the value of m_t can be used to constrain m_H. Indirect constraints from LEP, SLD and ν-nucleon interactions [6] are given by the conical ellipse (solid line). The dotted ellipse is the 1 standard deviation contour in m_t and m_W. Since the contour spans about ± 8 GeV along the m_t axis, it can be concluded that the 5 GeV uncertainty in the top mass is not a critically limiting factor in the constraint on m_H. However, the measurement of m_W will improve significantly in the future, with an uncertainty of 20 MeV being a realistic goal for Run II of the Tevatron (for a luminosity 30 event/fb). If this uncertainty is projected on a line of constant Higgs mass in Figure 2.4, the 20 MeV uncertaninty in m_W corresponds to an uncertainty of 3 GeV in the mass of the top quark. Thus an uncertainty less than 3 GeV in the mass of the top quark would allow to make maximun use of the other precision electroweak measurements.

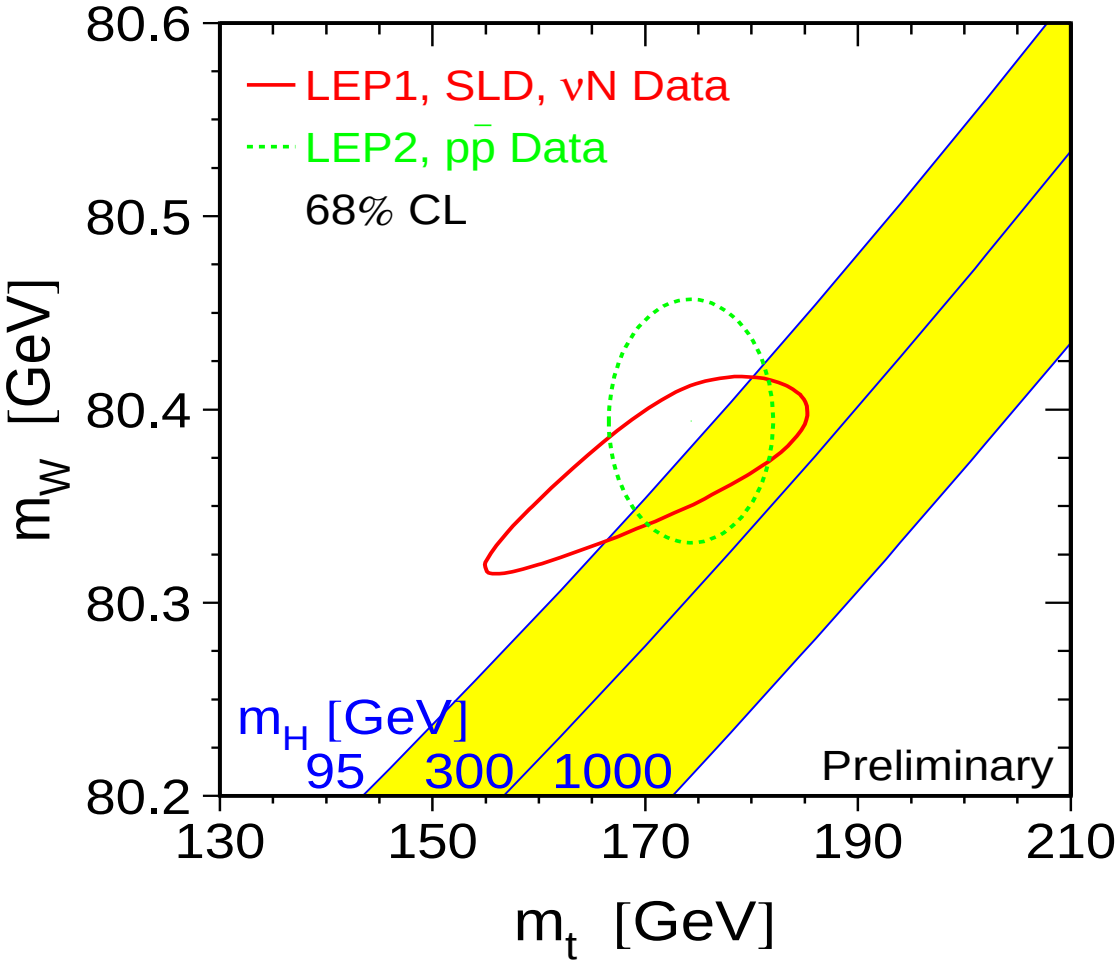

Figure 2.4: Electroweak precision measurements [6]. The straight lines corrspond to different choices for the Higgs mass in the S.M.

Chapter 3

Fermilab and DØ

This chapter contains a brief description of the accelerator complex and the elements of the DØ detector. A more complete discussion of the latter can be found in Ref. [7].

3.1 The accelerator and the beam.

Because of the large value of m_t, the production of pairs of top quark requires a large center-of-mass (CM) energy, and the Tevatron $p\overline{p}$ collider is the ideal accelerator for this purpose. The drawback in using a $p\overline{p}$ collider is that protons, unlike electrons, are objects composed of quarks and gluons, and this complicates the analysis of the collisions, and means that only a fraction of the total CM energy is available in any

particular $p\overline{p}$ collision.

The Fermi National Accelerator Laboratory (Fermilab), located in Batavia, Illinois, about 40 miles west from Chicago, is the home of the Tevatron accelerator.

The data used in this analysis were collected in what is called 'Run I' of the Tevatron, which started in 1992 and finished in 1996. During most of that time the accelerator ran at the world's highest center-of-mass energy of 1800 GeV. Since the end of Run I, the accelerator has been upgraded for a new run that started in March 2001.

A schematic of the accelerator complex used in Run I is shown in Fig. 3.1. The Tevatron is effectively a proton storage ring, containing superconducting magnets. In Run I, the Tevatron was filled with six bunches of protons and antiprotons that circulated in opposite directions. The trajectories of these two beams were set to produce collisions at the B0 and D0 experimental areas. A sophisticated series of processes are used to accumulate these p and $\overline{p}$ beams in the Tevatron Ring, and to make them collide, and we provide a brief description of this below. More details can be found in Refs. [8, 9, 10, 11].

The first step involves the preaccelerator, where H^- ions are formed and accelerated to 750 keV by an electrostatic Cockroft-Walton accelerator. This accelerator operates in a pulsed mode with a frequency of 15 Hz. The preaccelerator is the ion source for the Linac.

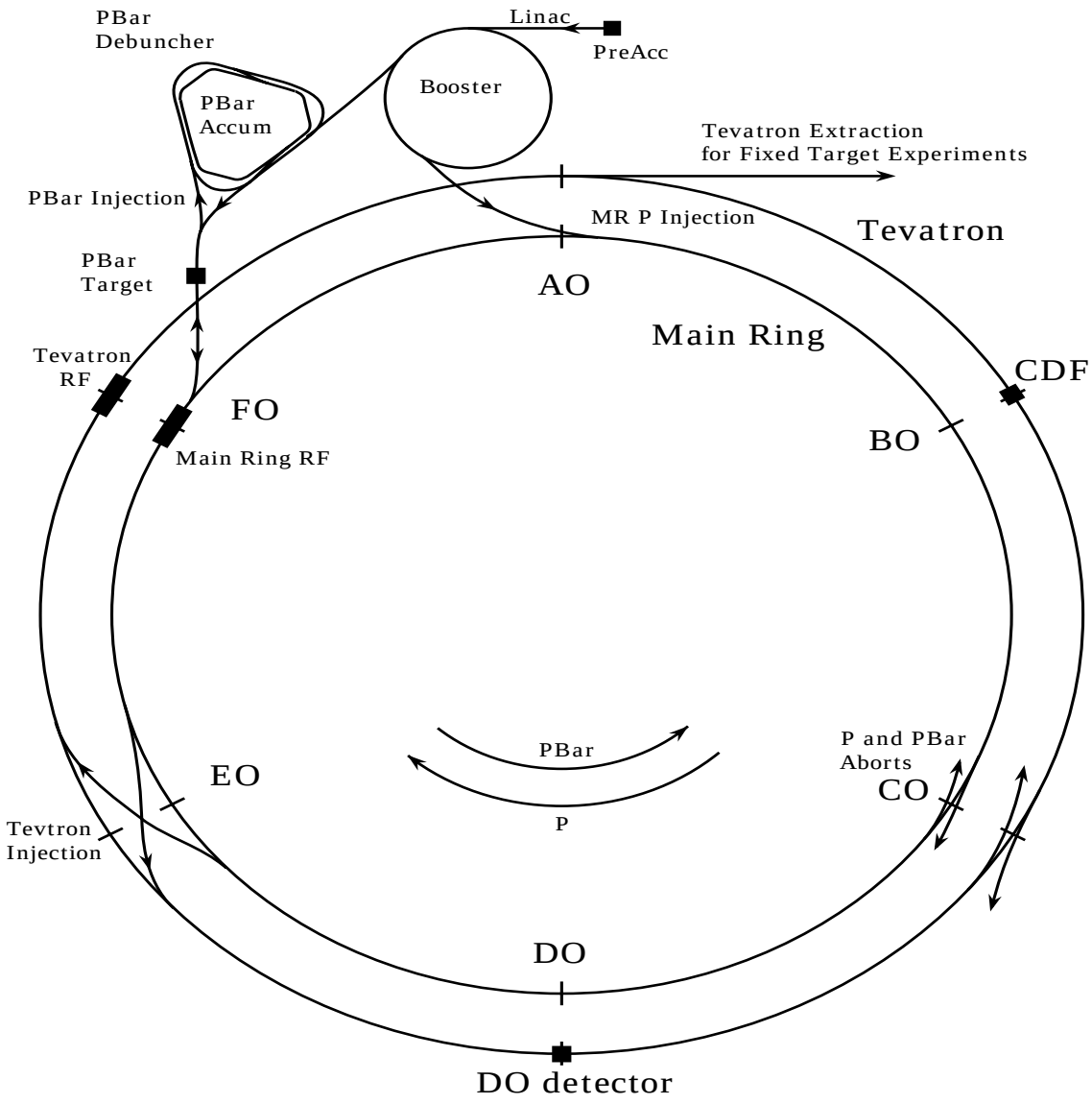

Figure 3.1: Schematic of the accelerator complex

The Linac is a 150 m linear accelerator that boosts the energy of the ions to 400 MeV. At the end of the Linac, there is a carbon foil that strips off the electrons from the H^-, leaving bare protons. The protons at the end of the Linac are then injected into the Booster.

The Booster is a synchrotron accelerator 151 m in diameter. As in any synchrotron, the charged particles are confined in a closed orbit with bending magnets. RF cavities along the booster are used to increase the energy of the charged particles, and, as the energy increases, the field in the confining magnets is increased to keep the particles in the same orbit. The Booster accelerates the protons to an energy of 8 GeV, and these are then injected into the main Main Ring.

The Main Ring is also a synchrotron (radius of ≈ 1 km) that has conventional (not superconducting) magnets. The original ring was deformed at B0 and D0 with over-passes to accommodate the CDF and DØ detectors. The protons in the Main Ring are accelerated to ≈ 120 GeV, at which point they can be used to make antiprotons, or they can be injected for further acceleration in the Tevatron Ring.

The antiproton source is a major element of the accelerator complex. It is used to produce and store antiprotons for collisions in the Tevatron. While collisions are occurring at the Tevatron, typically, the antiproton source is running continuously at a production cycle 2.4 s. To prodice antiprotons the 120 GeV protons in the Main Ring are extracted onto a nickel target. These collisions produce a spray of

Table 3.1: Accelerator parameters

Accelerator radius	1000 m
Maximum beam energy	900 GeV
Injection energy	150 GeV
Peak luminosity	$10^{31} cm^{-2} s^{-1}$
Number of bunches	$6p$,$6\overline{p}$
Intensity per bunch	$\approx 100 \times 10^9 p$, $\approx 50 \times 10^9 \overline{p}$
Crossing angle	0
Bunch length	50 cm
Transverse beam radius	43 μm
Energy spread	0.15×10^{-3}
RF frequency	53 MHz
$\overline{p}$ stacking rate	$\approx 3.5 \times 10^{10}$/hour
Beam crossing frequency	290 kHz
Period between crossings	3.5 μs

nuclear debris, which includes some antiprotons. Immediately following this target, there is a lithium "lens", a cylindrical piece of lithium through which a large current (0.5 MA) can be passed. This generates an azimuthal magnetic field that focuses negatively-charged particles passing though its center. Following the lens, there is a bending magnet that selects negatively-charged particles with energies of 8 GeV, and transports them to the Debuncher. The Debuncher is a storage ring in which antiprotons are rotated in phase space from a configuration with a small time spread and large momentum spread to one with large time spread but small momentum spread (this process is called 'debunching'). A further step to reduce the momentum spread is performed after the Debuncher, and is called stochastic cooling. Stochastic

cooling [12, 13] operates by measuring the trajectory of a collection of particles relative to the desired orbit. From this information, a correction signal is derived and passed across the ring to kicker electrodes to apply a force on the particles to move them back to the desired orbit. The effect on any single particle is very small because of the incoherent distribution of the other particles in the beam, but when repeated over a large number of turns, the effect becomes significant. The antiprotons are kept in the Debuncher until just before the arrival of the next pulse, which is about 2.4 s later. The antiprotons are then transfered to the Accumulator, another storage ring that is located along the Debuncher. There, cooling continues for several hours, and eventually the antiprotons settle into a dense core near the inner radius of the Accumulator. When enough antiprotons have been accumulated to fill the Tevatron (typically of the order of 10^{12} particles), they are extracted from the Accumulator, accelerated to 150 GeV in the Main Ring, and injected in bunches into the Tevatron.

The Tevatron is a proton synchrotron made from superconducting magnets [8, 9, 10, 11]. It sits bellow the Main Ring in the accelerator tunnel, and has a maximum beam energy of 1000 GeV. The Tevatron can be operated in one of two modes. In the fixed-target mode, the Tevatron is filled with protons that are accelerated and then extracted and directed to different experimental areas. This cycle can be repeated about every minute. In the collider mode, the Tevatron is filled with six bunches of

protons and six bunches of antiprotons of 120 GeV , traveling in opposite directions. The beams are then accelerated to the maximum possible energy (about 900 GeV in Run I), and made collide at the B0 and D0 accelerator sectors. There are other points where the beam can collide, and there special electrostatic separators are used to keep them apart. The beams are kept colliding typically for about 20 hours, after which time the machine is emptied and refilled with new batches of protons and antiprotons. The Tevatron parameters are sumarized in Table 3.1.

3.2 The DØ detector.

As mentioned in Chapter 2, the top quark decays into electrons, muons, neutrinos and jets, and a detector capable to identify and measure these particles is needed for studying the top quark.

DØ [7] is a multipurpose detector assembled to investigate $p\overline{p}$ collisions at the Tevatron [8, 9, 10, 11]. It has been running since 1992, a schematic of the detector with an indication of its scale is shown in Fig. 3.2. It features good electron and muon identification, and excellent calorimetry that provides a good measurement of energies for electrons, photons and hadrons (jets). The DØ detector did not have a central magnetic field in Run I, and relied on its calorimetry to measure energies and to identify electrons and photons. The detector consists of three parts: the central

tracker, the calorimeter and the muon spectrometer. These units will be discussed below.

3.3 Coordinates system.

For clarity, we will begin with a description of the coordinate system for the detector. The z-axis of the Cartesian coordinates is defined as the direction of the proton beam, and the y-axis is upward. The x-axis is then fixed by the right hand rule. The radial distance in the transverse plane is defined by $r = \sqrt{x^2 + y^2}$. The azimuthal angle ϕ is measured relative to the x-axis in the plane transverse to the beam. The polar angle θ is measured relative to the z-axis.

Instead of using θ, we define the more convenient coordinate, the pseudorapidity

$$\eta = -\ln(\tan\frac{\theta}{2}) \quad . \tag{3.1}$$

In the ultrarelativistic limit, i.e. $m/E \to 0$, η approximates the true rapidity:

$$y = \frac{1}{2}\ln(\frac{E + p_z}{E - p_z}) \quad . \tag{3.2}$$

Using η, the invariant inclusive cross section for producing any particle of energy

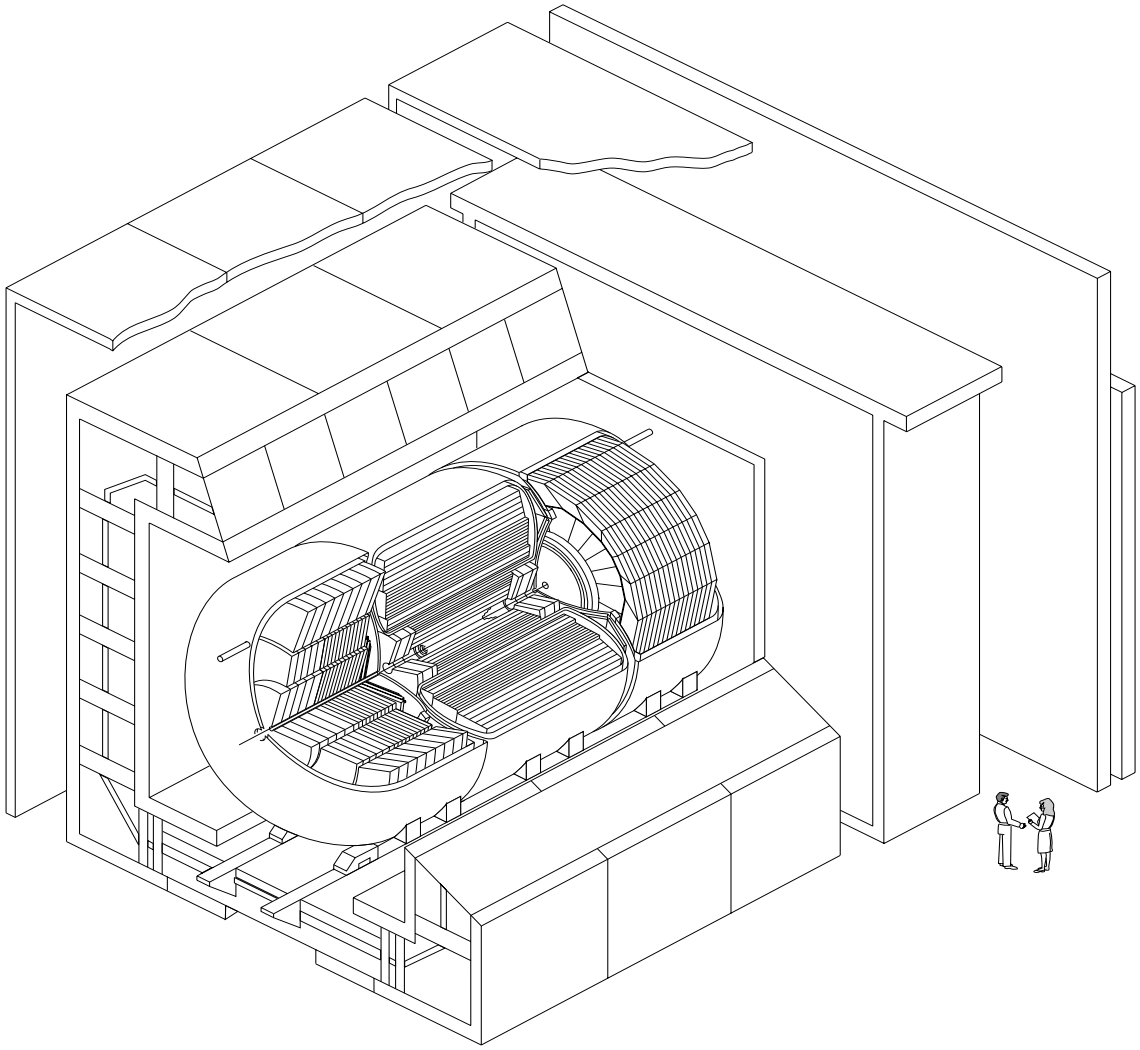

Figure 3.2: Schematic of DØ, a multipurpose detector assembled to investigate $p\overline{p}$ collisions at the Tevatron.

E and momentum $\overrightarrow{p}$, can be expressed as

$$E\frac{d\sigma}{d^3p} = \frac{1}{2\pi}\frac{d\sigma}{p_T dp_T dy} \cong \frac{1}{2\pi}\frac{d\sigma}{p_T dp_T d\eta} \quad , \tag{3.3}$$

where p_T is the transverse momentum of the particle, and the distribution in ϕ is assumed isotropic (for unpolarized beams).

3.4 The Central Tracker

The central tracker is in the innermost section of the detector. This subdetector is used to reconstruct charged-particle tracks, to determine positions of interaction vertexes, and to measure the ionization of charged particles to distinguish a singly charge particle from photon conversions ($\gamma \rightarrow e^+e^-$) in the detector. The tracker is composed of three types of gaseous drift chambers: a vertex drift chamber (VTX), a central drift chamber (CDC), and two forward drift chambers (FDC). The central tracker also contains a transition radiation detector (TRD). The arrangement of the tracker is shown in Fig. 3.3.

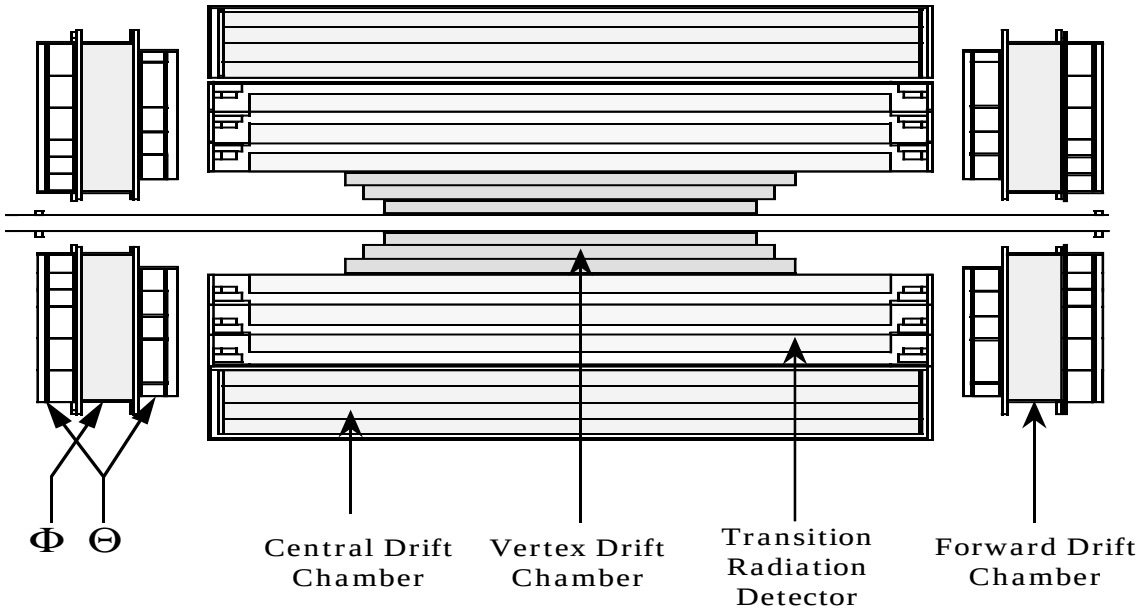

Figure 3.3: Schematic of the DØ central tracker.

3.4.1 Drift Chambers

Drift chambers are designed to detect ionization liberated by a charged particle passing through the gas-filled region. The produced ionization is proportional to the total energy deposited by the particle, and it depends on the ionization potential of the gas. The typical number of ions pairs is of the order of 50 per cm of traversed gas, and corresponds to primary ionization electrons.

When a voltage is applied across the sensitive region, the free electrons drift toward the anode. The energy gained by the electrons drifting in the electric field comes quickly into equilibrium with that lost due to collisions with atoms, and the drift velocity, on average, becomes constant.

The number of drift electrons that eventually reach the anode is far too small to produce an observable signal. However, if the anode is a sufficiently thin wire (typically 20 μm diameter), it creates a large electric field ($10^4 - 10^5$V/cm) very close to the wire. In the region where this field is large enough, the energy gained by the electrons between atomic collisions will exceed the ionization potential of the gas, creating an avalanche of secondary ionization. The number of secondary electron-ion pairs is typically 10^5 times that of the primary ionization, and such a gain is sufficient to produce a detectable signal.

If a drift chamber is constructed to have the potential gradient approximately constant across the region of transverse electron drift, then the relation between the arrival time of the signal and distance to the original ionization will be linear. This timing feature is used to measure the trajectory of a charged particle through a drift chamber.

For further details on drift chambers see Refs. [14], [15] and [16].

Vertex Chamber (VTX).

The Vertex Chamber [17] has an inner radius of 3.7 cm, and an outer radius of 16.2 cm. It consists of three layers of concentric cells, as shown in Figure 3.4. The innermost layer has 16 cells in azimuth, and the outer two have 32 cells each. The sense wires have a resistivity 1.8 kΩ/m, and provide a measurement of the

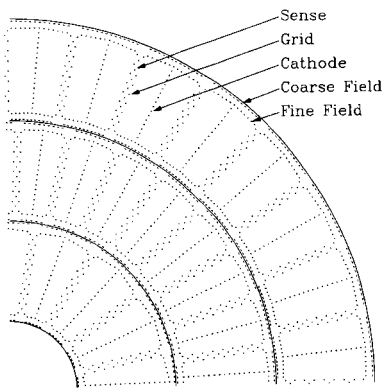

Figure 3.4: The r-ϕ view of a quadrant of the Vertex Drift Chamber (VTX).

z-coordinate from the pulse height read out at both ends. The ϕ position of a hit is determined from the drift time. The spatial resolution along the azimuth $r\delta\phi$ is $\approx 60\mu$m and, the resolution in z is ≈ 1.5 cm.

Central Drift Chamber (CDC).

The Central Drift Chamber [18] is located between the TRD and the central calorimeter. The CDC consists of a cylindrical shell, 184 cm long, and with radii ranging between 49.5 cm and 74.5 cm. It has four concentric rings of 32 azimuthal cells per ring. Each cell has 7 equally spaced sense wires at the same ϕ coordinate. These wires are parallel to the z-axis, and are read out at one end to measure the ϕ coordinate of the track. There are delay lines embedded in the inner and outer shelves of each cell. The delay lines propagate signals to both ends, indexed from the nearest

neighboring anode wire. The z coordinate of a track can be obtained from the difference in the arrival times of signals at the two ends. The $r\delta\phi$ resolution is $\cong$ 180 μm, and the resolution in z is $\cong$ 3 mm.

Forward Drift Chambers (FDC).

The Forward Drift Chambers [19] are located at either end of the concentric barrels of the VTX, TRD and CDC, and just before the inner walls of the end calorimeters. They extend the coverage for charge-particle tracking down to $\theta = 5^o$. Each FDC package consists of three separate chambers, as shown in Figure 3.5. The Φ module has radial sense wires used to measure the ϕ coordinate. It is sandwiched between a pair of Θ modules, whose sense wires determine the θ coordinate. The geometry of the FDC is more complicated than that of the CDC, but the operating principle is similar, and the chamber gas is the same. The position resolution is about 200 μm in $r\delta\phi$ and 300 μm in $r\delta\theta$.

3.4.2 Transition Radiation Detector (TRD).

The Transition Radiation Detector [20] is located between the VTX and the CDC. It provides independent electron identification, in addition to that given by the calorimeter and the tracking chambers. When highly relativistic charged particles($\gamma = E/m > 10^3$) traverse boundaries between media of different dielectric constants,

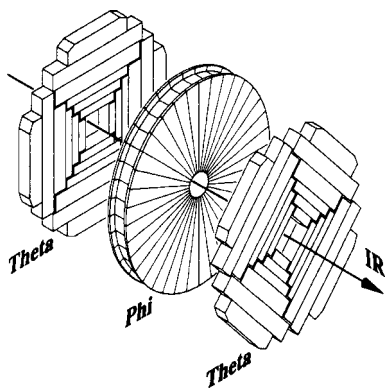

Figure 3.5: Schematic of the FDC. Two Θ modules with a Φ module in between.

transition-radiation X-rays are produced at a cone with an opening angle of $\approx 1/\gamma$. The energy flux of the radiation is proportional to γ. These characteristics can be use to distinguish particles that have similar energies but different masses.

The TRD consists of many thin dielectric foils (polypropylene), with gaps of nitrogen gas between them. Charged particles tranversing such an array produce X-ray radiation. A radial-drift proportional wire chamber containing xenon gas acts as the X-ray conversion medium and also collects the resulting ionization charges that drift radially towards the sense wires. The magnitude and arrival time of the charge clusters are used to distinguish electrons from hadrons. Because if its low detection efficiency, this device was not used in all analyses.

3.5 The Calorimeter.

Because of the absence of an inner tracking magnet, we rely on the calorimeter to identify electrons, photons and jets, and to reconstruct their energies. The detected energies in the calorimeter are used to determine the transverse momenta (or transverse energies, $P_T \approx E_T = E \sin\theta$) of jets, and the imbalance in an event (often called "missing E_T" or $\not{E}_T$). In general, this can be associated with neutrinos that escape detection.

The DØ calorimeter is a sampling calorimeter. A typical configuration of the sampling calorimeter is a stack of dense metallic plates ("absorber material") in which particles interact and loose energy, interleaved with regions of sensitive material where any deposited ionization energy can be sampled and measured. The energy deposited in the active layers accounts for only a fraction of the total energy, usually 1-10%, and this fraction is almost independent of incident energy. Therefore, through proper calibration, a sampling calorimeter can provide a precise value of incident particle energy. The DØ calorimeters use liquid argon as the sensitive material, and primarily uranium and copper as absorber.

There are two types of particle-induced showers that can be distinguished in a calorimeter: electromagnetic showers, which deposit most of their energy in the upstream sections of a calorimeter, and are produced by energetic electrons or photons,

and hadronic showers, which deposit most of their energy in the downstream part of the calorimeters and are initiated by hadrons.

An electromagnetic shower consists of a cascade of electrons, positrons, and photons that result from bremsstrahlung and e^-e^+ pair production initiated by incident photons or electrons, as they travel through and interact in the calorimeter. The number of secondary particles increases geometrically, until electrons reach the "critical energy", at which point the electrons loose the same amount of energy through radiation as through ionization of the medium. After that, the number of particles decreases and their energy gradually dissipates through the process of ionization.

Unlike electromagnetic showers, the physical processes that cause the propagation of hadronic showers are mainly strong interactions between hadrons and nuclei. A considerable fraction of the hadron energy is transferred to the intervening nuclei, and causes the production of secondary hadrons, which in turn produce more hadrons. This cascade develops until the energies of the secondary hadrons are exhausted through ionization, or the particles are absorbed in nuclear break-up processes. Neutral pions (π^0) can be produced as secondary hadrons, and then decay into two photons, which gives rise to an electromagnetic component within a hadronic shower.

Hadronic showers tend to spread more laterally, and are more penetrating longitudinally than electromagnetic showers. Also, the greater variety of hadronic interactions implies larger fluctuations in the measurement of their energies.

The longitudinal development of electromagnetic showers is characterized by the radiation length of the intervening material (X_0), which corresponds to the mean distance over which an electron loses all but $1/e$ of its energy (mainly by bremsstrahlung). The length scale appropriate for hadronic showers is the nuclear interaction mean free path (λ_I), which is the distance over which the probability that an incident hadron interacts inelastically with the intervening calorimeter material is $(e-1)/e \approx 0.63$. Both the radiation length and the nuclear interaction mean free path depend on the nature of the material of the calorimeter, and can be approximated by the empirical formulae [21]:

$$X_0 \approx \frac{716.4\ \mathrm{A}}{Z(Z+1)\ln(287/\sqrt{Z})}\ \mathrm{g/cm^2} \quad \text{and} \tag{3.4}$$

$$\lambda_I \approx 35A^{\frac{1}{3}}\ \mathrm{g/cm^2} \quad , \tag{3.5}$$

where Z and A are, respectively, the atomic number and the atomic weight of the medium. Typically, $\lambda_I \gg X_0$. Dense absorbers such as steel ($X_0 = 1.76$ cm, $\lambda_I = 16.76$ cm) or uranium ($X_0 = 0.32$ cm, $\lambda_I = 10.5$ cm) are often used to minimize

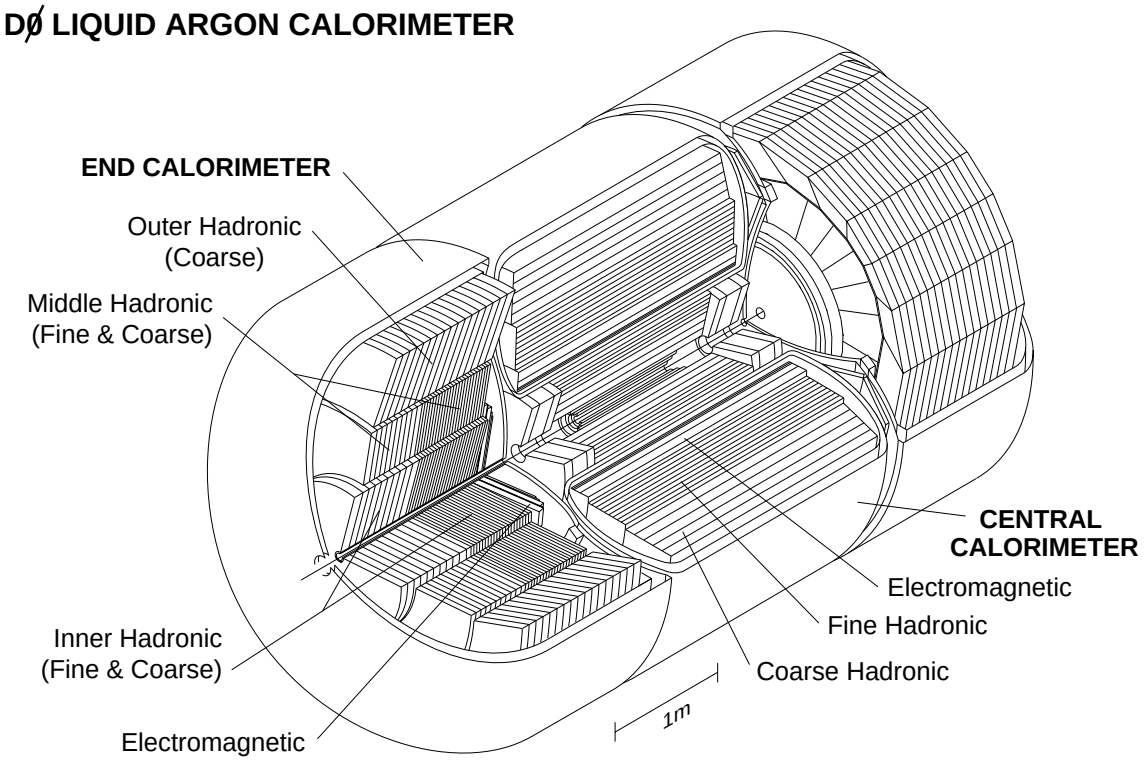

Figure 3.6: Schematic of the DØ calorimeter

the size of a calorimeter.

The DØ liquid argon calorimeters consist of a central calorimeter (CC) and two end calorimeters (EC), as shown in Figure 3.6. Each calorimeter is contained within a separate cryostat, and each contains an inner electromagnetic (EM) section, a fine hadronic (FH) section, and a coarse hadronic (CH) section. The intercryostat detector (ICD), made of scintillator, is located between the CC and the EC cryostats, and is used to improve the energy resolution of jets in that region.

The EM section of each cryostat of the DØ calorimeter is roughly 21 radiation

lengths deep, and is divided into four longitudinal layers, in order to provide information on the profile of the showers. Depending on η, the hadronic sections present an extra 6 to 9 nuclear interactions lengths to an incident nucleon, beyond the ≈ 1.0 λ_I of material of the EM section. These sections are divided in four (CC) or five (EC) layers. As shown in Figure 3.7, the calorimeter is segmented into towers of $\Delta\eta \times \Delta\phi = 0.1 \times 0.1$. The third layer of the EM section, which is where the maximum number of particles in electromagnetic showers are expected to occur, has a finer segmentation of $\Delta\eta \times \Delta\phi = 0.05 \times 0.05$.

The performance of the calorimeter has been studied at a test-beam facility [22, 23] with electron and pion beams, for energies between 10 and 150 GeV. From these studies it has been concludes that the relative resolutions are [22, 23]:

$$\frac{\sigma(E)}{E} = \frac{16\%}{\sqrt{E(GeV)}} \oplus 0.3\% \quad \text{for electrons and} \tag{3.6}$$

$$\frac{\sigma(E)}{E} = \frac{41\%}{\sqrt{E(GeV)}} \oplus 3.2\% \quad \text{for pions.} \tag{3.7}$$

Where $\sigma(E)$ is the resolution as a function of energy E, and $\oplus$ means to be added in quadrature.

3.5.1 Central and End Calorimeters.

The central calorimeter (CC) covers the pseudorapidity range $|\eta| \leq 1$. It is comprised of three concentric cylindrical shells of 32 EM modules in the inner ring, 16 FH modules in the surrounding ring, and 16 CH modules in the outer ring. In order to reduce the energy loss in intermodular "cracks", the EM, FH, and CH module boundaries are arranged so that no projective ray encounters more that one intermodular gap.

A unit cell of a calorimeter module consists typically of two liquid-argon gaps, an absorber plate, and a signal board (with laminated Cu pads), as shown in Figure 3.8. Each signal board has a surface coated with fine resistive epoxy. The electric field in the cell is established by connecting the resistive surfaces of the boards to a high positive voltage (2.0-2.5 kV), and grounding the absorber plates. The electron drift time across the 2.3 mm Argon gap is ≈ 450 nsec.

The two mirror-image end calorimeters (ECs) extend the coverage to $|\eta| \approx 4$.

3.6 Muon Spectrometer.

In order for a particle to pass through the material in the calorimeter, it must have a sufficiently long lifetime to travel several meters before decaying, it must not have strong interactions (and thereby cause a hadronic shower), and be unlikely to

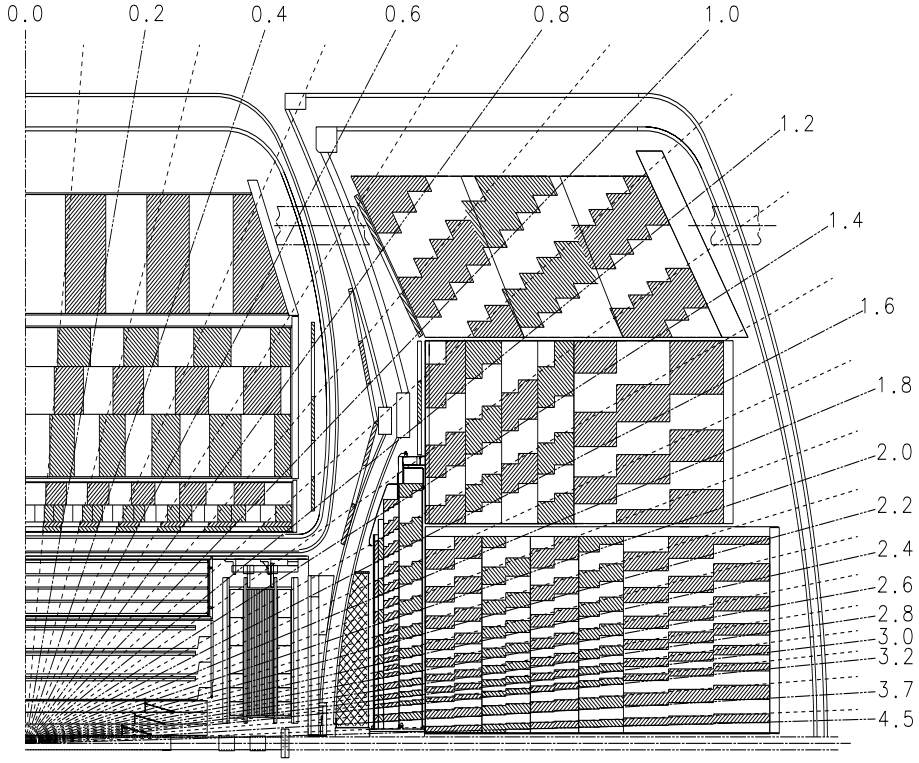

Figure 3.7: Side view of the DØ calorimeters. Rays of fixed η relative to the center of the detector are given in the sketch.

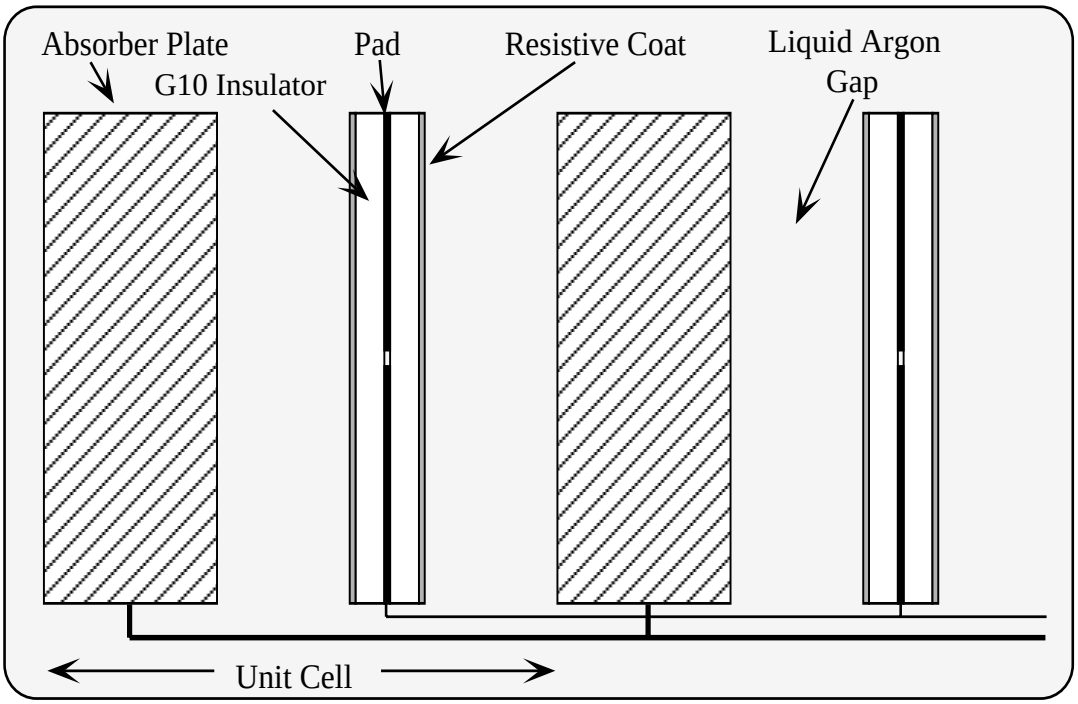

Figure 3.8: Unit cell in the DØ calorimeter.

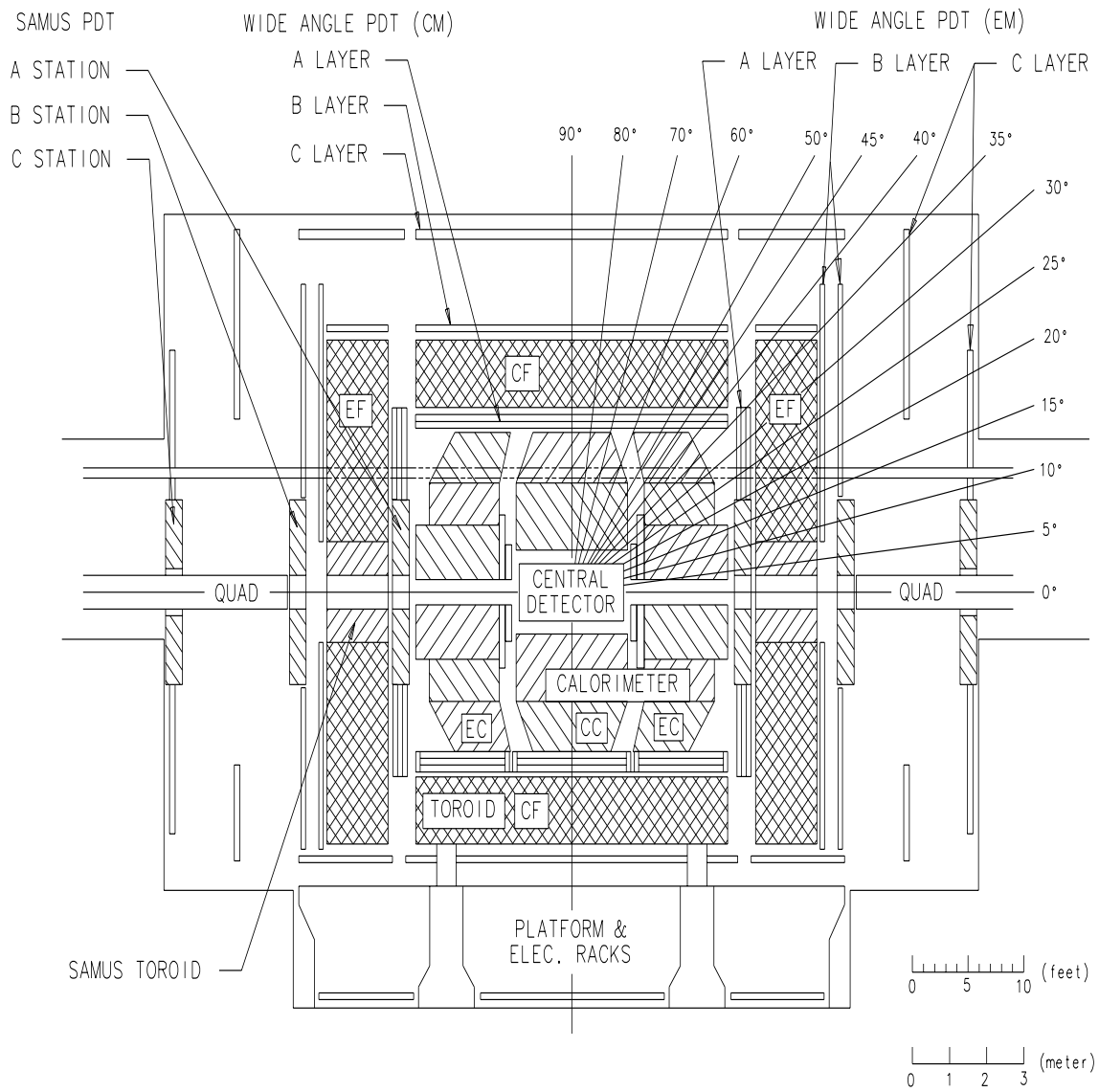

Figure 3.9: Muon Spectrometer in the DØ detector.

lose substantial energy to bremsstrahlung (which would produce an electromagnetic shower). The only charged particle with such properties is the muon, and that is why a subdetector was constructed outside of the calorimeter, expressly to detect muons. The Muon Spectrometer is shown in Figure 3.9.

Since usually muons deposit only little energy in the calorimeter (mainly through ionization), a magnetic spectrometer is used to measure their momenta. This consist of layers of proportional drift tubes (PDTs) surrounding magnetized iron toroids. A measurement of the particle direction before and after the toroid, determines the muon momentum. The additional material outside the calorimeter makes it extremely unlikely that any particle other than a muon will reach the outer layers of the drift tubes.

The Central Muon Spectrometer at DØ, or the Wide-Angle Muon Spectrometer (WAMUS), is formed of three planes of proportional drift tubes (PDTs), the first layer (A) is mounted on the inner surface of the magnetized iron toroid, the second (B) layer on the outer surface, and the final (C) layer ≈ 1.4 m beyond this. The A layer consist of four layers of PDTs, providing measurement of the incident muon direction to 0.6 mrad. Additional information from the reconstructed event vertex, the track in the central detector, and the muon energy deposited in the calorimeter, can be used to improve the measurement of the original direction. The B and C layers, each have three layers of PDTs, which determine the outgoing position and

direction to 0.17 mm and 0.2 mrad. The WAMUS PDTs cover the region of $|\eta| < 1.7$.

The Small Angle Muon Spectrometer (SAMUS) covers the region of $1.7 < |\eta| < 3.6$. Due to the high occupancy in the forward region, the SAMUS system uses small drift tubes. It is composed of three stations, each consisting of three planes of drift tubes. Each plane is composed of two subplanes, offset by half a tube diameter, each containing a single sense wire of 50 μm in diameter.

The resolution of the muon momentum measurement is limited largely by multiple coulomb scattering in the toroids and by the hit-position resolution in the drift chambers. The resolution was determined by comparing $Z \to \mu^+\mu^-$ data with similar Monte Carlo events where the resolution was degraded until the width of the $\mu^+\mu^-$ invariant mass for the Z matched that observed in the data. The resolution is approximately Gaussian in $1/p$, and can be parameterized as [25]:

$$\sigma(\frac{1}{p}) = \frac{0.18(p-2)}{p^2} \oplus 0.003 \quad , \tag{3.8}$$

where p is the momentum in GeV.

Chapter 4

Reconstruction and Particle Identification

After an interesting event is selected for offline study by the DØ trigger system (see Ref.[26, 27, 28, 29, 30]), all digital information is stored on tape cassettes (ADC counts for the calorimeters, TDC counts for the drift chamber, etc.), and combined to obtain offline the kinematic parameters of the physical objects present in the event. The process of turning the detector data into description of physical objects, such as leptons and jets, is called event reconstruction.

The reconstruction process can be divided in two steps.

- Tracking and Clustering. In this step, hits in each subdetector are correlated, and used to construct objects. The hits in the calorimeter are clustered and the

information in the tracking chambers is used to construct particle trajectories.

- Particle Identification. During this step, information from all parts of the detector is combined to produce candidate electrons, jets and muons.

In this work, we will describe only particle identification (ID). For other steps in event reconstruction at DØ see Ref. [31].

4.1 Electron Identification.

Electrons are defined as localized depositions of energy associated with a track pointing back through the central tracker to an interaction vertex. Details can be found in Ref. [32, 33, 34].

4.1.1 Candidate Construction.

Electron candidates are identified as follows:

- Using a nearest neighbor algorithm, clusters are formed from calorimeter towers.

- A cluster is required to have at least 90% of its energy in the electromagnetic calorimeter, and at least 60% of the energy must be contained in a single 0.1×0.1 tower.

- The centroid of the cluster is computed using the cells in the third electromagnetic layer.

- The reconstruction program searches for a track from the central detector pointing from the interaction vertex to the calorimeter cluster. The match is required to be within $\Delta\eta < 0.1$ and $\Delta\phi < 0.1$. If such track is found, the cluster is identified as an electron candidate, otherwise it becomes a photon candidate.

Up to this point, the requirements for an electron candidate are not very restrictive. Any ensuing analysis applies additional criteria tailored to the particular situation of interest. Selections for the analysis of $t\bar{t}$ events are described below.

4.1.2 Covariance Matrix χ^2

A covariance matrix[32, 33, 34] is defined for quantifying the information contained in the shape of an electromagnetic shower, as follows. We define a training sample by N observations of events of some given type, where each observation consists of M variables: $\mathbf{x^i} = (x_1^i, ..., x_M^i)$, and $i = 1, ..., N$. In term of the parameters, we can construct the covariance matrix $\mathbf{V}$ as:

$$\mathbf{V} = \frac{1}{N}\sum_{i=1}^{N}(\mathbf{x^i} - \bar{\mathbf{x}})^T(\mathbf{x^i} - \bar{\mathbf{x}}) \quad , \tag{4.1}$$

where $\bar{\mathbf{x}} = (\bar{x}_1, ..., \bar{x}_M)$, and $\bar{x}_j = \frac{\sum_{i=1}^{N} x_j^i}{N}$. The "H-matrix" is defined as the inverse of the covariance matrix

$$\mathbf{H} = \mathbf{V}^{-1} \quad . \tag{4.2}$$

For any subsequent similar measurement $\mathbf{y}$, one can define a χ^2 that quantifies the consistency of $\mathbf{y}$ with the training sample:

$$\chi^2 = (\mathbf{y} - \bar{\mathbf{x}})\mathbf{H}(\mathbf{y} - \bar{\mathbf{x}})^T \quad . \tag{4.3}$$

For the problem of electron identification, the training sample consists of Monte-Carlo generated single electron showers. A total of $M = 41$ observables is used in $\mathbf{V}$, consisting of the fractional energies in Layers 1,2, and 4 of the EM calorimeter, the fractional energies in each cell of a 6x6 array in the third EM layer (centered on the most energetic tower in the cluster), the z-position of the interaction vertex, and the logarithm of the total energy of the cluster. A separate matrix is constructed for each ring of calorimeter cells (i.e., as a function of the η coordinate). A good

electron is defined by $\chi^2 < 100$.(For distributions of this χ^2 variable see Ref. [35].)

4.1.3 Isolation.

Because of the large energy release in $W \to e\nu$ decay, the decay electron from a W tends not be close in space to any other object in the event. This criterion is quantified as the "isolation fraction" for the shower, as follows: If $E_{tot}(0.4)$ represents the energy deposited in all the calorimeter cells within a cone of $R = \sqrt{(\Delta\eta)^2 + (\Delta\phi)^2} < 0.4$ around the electron direction, and $E_{EM}(0.2)$ is the energy deposited in the electromagnetic calorimeter within a cone of radius $R < 0.2$, then the isolation fraction is defined by:

$$f_{iso} = \frac{E_{tot}(0.4) - E_{EM}(0.2)}{E_{EM}(0.2)} \quad . \tag{4.4}$$

For the present analysis, good electron candidates are required to have $f_{iso} < 0.1$. The distributions of f_{iso} for Monte Carlo simulated objects can be found in Ref. [35].

4.1.4 Significance of a Track-match.

A significant source of background to electrons are photon showers. A photon does not produce a track in the central detector, but it might appear to have an associated track when there is some charged particle emitted close to its direction. Such background to electrons can be reduced by requiring that the reconstructed track point accurately to the centroid of the calorimeter cluster. This selection is quantified by using a significance for the track matching:

$$S = \sqrt{\frac{\Delta\phi}{\sigma_\phi} + \frac{\Delta z}{\sigma_z}} \quad , \tag{4.5}$$

where $\Delta\phi$ and Δz are the differences in coordinate between the centroid of the cluster and the point at which the trajectory of the track extrapolates to the calorimeter, and σ_ϕ and σ_z are the corresponding measurement resolutions. For this analysis, good electron candidates are define as those with $S < 5$. A distribution of track significance for Monte Carlo simulated objects can be found in Ref. [35]

4.1.5 Track Ionization.

Because DØ has no central magnetic field, e^+e^- pairs resulting from photon conversion do not diverge very much from each other, and their trajectories are often

reconstructed as a single track. However, away from the point of conversion, the energy deposition per unit length will be twice that for a single electron (which is called one MIP, minimum ionizing particle). This background can be reduced by removing events in the region > 2 MIPs. Distributions of the energy deposition can be found in Ref.[35].

4.1.6 Kinematic Criteria and Summary.

In addition to the above quality criteria, the $t\bar{t} \rightarrow e+$jets analysis requires electrons with $E_T > 20$ GeV and $|\eta^{det}| < 2$ (where det refers to η defined relative to the center of the detector). This is done to reduce background (it has very little impact on signal). The final efficiency for identifying single acceptable isolated electrons with these selections is about 72% in the CC and 43% in the EC, and is essentially idependent of the electron energy.

4.1.7 Electron Energy Corrections.

The absolute energy scale of the calorimeter was originally based on calibration data obtained in a test beam. However, due to a possible difference between the test beam module (never used in the DØ detector) and the modules installed at DØ, this calibration did not provide the correct mass of the Z boson in $Z \rightarrow e^+e^-$ events. Because this mass is known very accurately from LEP experiments [36],

the measured electron energies were consequently scaled up so that the mass peak in $Z \to e^+e^-$ matched the LEP value. This correction is about 5% in the central calorimeter, and 1-2% in the end calorimeter.

4.2 Muon Identification.

Muons are identified as tracks in the muon chamber that point back to the interaction vertex. There are two major backgrounds to consider: cosmic-ray muons and hadronic showers that extend beyond the calorimeter. The latter background is important only in the transition region between the cryostats, where there in not as much absorber material as in the rest of the detector. Further details can be found in Ref. [37].

4.2.1 Reconstruction of Muon Trajectory.

Track segments are formed separately before and after the magnet. These segments are matched, and the muon momentum determined by the bend in the track through the magnet.

The momentum resolution of the muon spectrometer is not very good, but it can be improved if the muon trajectory can be associated with a track in the central detector and with an interaction vertex. This provides a more accurate muon

trajectory before the magnet.

The measured muon momentum is the momentum of the particle after it passes the calorimeter. Typically, a muon deposits several GeV of energy in the calorimeter. This energy loss can be estimated through a Monte Carlo calculation and added to the measured momentum. The energy deposited in the calorimeter is also useful for rejecting background to muon candidates.

4.2.2 Impact Parameters.

Good muon candidates have requirements that their trajectories point to the interaction vertex. These criteria are used to reduce background from cosmic rays. In particular, an impact parameter is defined in the non-bend view by projecting the muon track into the x,y plane, and extrapolating the trajectory formed by the B and C layers towards the center of the detector. The impact parameter is then calculated between this extrapolated track and the interaction vertex, and in this analysis it is required to be less that 40 cm. A similar impact parameter in the bend-view is obtained by projecting the muon trajectory onto the bend-plane, and calculating the impact parameter of this trajectory at the interaction vertex. For an acceptable muon, the impact parameter is required to be less than 25 cm.

4.2.3 Cosmic Ray Veto.

A cosmic ray muon that penetrates the entire detector leaves hits in the muon chambers on both sides of an interaction vertex. Therefore, a track in the central region ($|\eta| < 1$) is rejected if there is another track, or an excessive number of hits, aligned with it in the opposite hemisphere.

4.2.4 Track Timing.

The time T_0 at which a particle goes through a drift chamber is needed for determining the drift time and thereby the location of a track. Normally, this is calculated relative to the time at which the beams cross. For tracks caused by cosmic rays, this value will not be correct, since they are not synchronized with the accelerator. In fact, for a cosmic-ray muon, the quality of the track usually improves by using a T_0 different from the one based on a beam crossing. This provides another way to reject cosmic rays. A χ^2 fit to any muon track is therefore minimized with respect to T_0, and the result is compared with the nominal T_0 for the beam crossing. If the difference is larger than 100 nsec, the track is rejected.

4.2.5 Hit Multiplicity.

Depending on the region of the detector, a muon track will typically have hits in 7-10 drift tubes. High-p_T muons in the end regions are required to have at least 5 hits (there is no explicit requirement for the central region).

4.2.6 Isolation and Confirmation in the Calorimeter.

A muon passing through the detector will deposit typically between 1 and 3 GeV of energy in the calorimeter. An acceptable muon track is required to have at least 1 GeV of energy deposited along its trajectory in the calorimeter. Also, a good muon must be separated from any jet by a minimum distance of $R = 0.5$.

4.2.7 Kinematic Criteria and Summary.

Accepted muons are required to have trajectories contained entirely in the WAMUS system, that is, in the region of $|\eta| < 1.7$. Our $t\bar{t}$ analysis also requires that muons from W decays have $E_T > 15$ GeV. The efficiency for finding isolated muons in $t\bar{t}$ events with these set of criteria is $\approx 41\%$. A different set of requirements is used for identifying muons associated with b quarks.

4.3 Jet Reconstruction.

When a quark or gluon leaves the site of a hard scattering, QCD hadronization and fragmentation effects produce a collection of colorless hadronic particles that are emitted in a cone around the direction of the momentum of the initial parton. These secondaries interact in the calorimeter, and the final cluster of energy is called a calorimeter jet.

This analysis uses the cone-clustering algorithm for reconstructing jets [38, 39, 40, 41]. It is a standard algorithm used in previous experiments, and will not be discussed any further. For the $t\bar{t}$ mass analysis the jets are formed using $R = \sqrt{(\Delta\phi)^2 + (\Delta\eta)^2} = 0.5$ cones, where $\Delta\phi$ and $\Delta\eta$ correspond, repectively, to the sizes of the clusters in azimuth and pseudorapidity. A first level of energy corrections is applied before the events are selected, and this is used in most DØ analyses (see in Ref. [42] for details). These "CAFIX" corrections will not be discussed any further. In the rest of this chapter, we will concentrate on the next levels of jet energy corrections that are needed to improve the resolution in $t\bar{t}$ events.

4.3.1 Jet Energy Corrections.

The DØ Standard.

Figure 4.1 displays a scatter plot of the energies of generated partons and their reconstructed jets in lepton+jets $t\bar{t}$ Monte Carlo events. As can be seen, the cone algorithm yields jets of smaller energy than carried by the original partons. A correction is therefore required to account for this effect for cases where the quantity of interest is the original parton energy, as is the case in our analysis of the mass of the top quark.

DØ has a standard way to make such corrections, and these are described in detail in Refs. [43], [44] and [45]. The general idea is to modify the energy of the reconstructed jet to recover, on average, the energy of the parton. The corrections are made in two steps:

1. "Out-of-cone" corrections are made to compensate for the radiation of particles outside the cone considered in the clustering algorithm. These corrections are derived from a comparison of the energy of reconstructed jets in MC simulated $t\bar{t}$ events with the energy of the corresponding partons. The correction is different for b quarks and for light quarks, and depends on η. The corrected energy E_{corr} is expressed in terms of the reconstructed jet energy E_{jet}

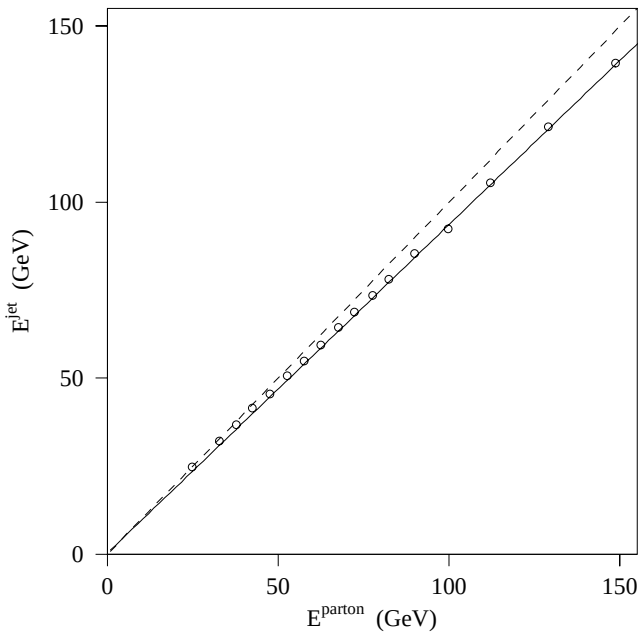

Figure 4.1: Effect of the out-of-cone radiation. The reconstructed jets have on average less energy than the original parton, this is the motivation for the out-of-cone corrections, which are based on the comparison of parton energies and energies of reconstructed jets in $t\bar{t}$ events (circles). The correction attempts to provide a 1:1 correspondence (given by the dashed line).

Table 4.1: Parameters for parton-level jet corrections. $E_{corr} = (E_{jet} - A)/B$.

	Light quark jets		Untagged b jets	
η region	A (GeV)	B	A (GeV)	B
$0.0 < \lvert\eta_{\rm det}\rvert < 0.2$	0.322	0.933	-0.672	0.907
$0.2 < \lvert\eta_{\rm det}\rvert < 0.6$	0.635	0.930	-1.34	0.914
$0.6 < \lvert\eta_{\rm det}\rvert < 0.9$	1.86	0.883	0.002	0.868
$0.9 < \lvert\eta_{\rm det}\rvert < 1.3$	1.70	0.933	-0.548	0.904
$1.3 < \lvert\eta_{\rm det}\rvert$	4.50	0.882	2.46	0.859

as follows:

$$E_{corr} = \frac{E_{jet} - A}{B} \tag{4.6}$$

where A is the intercept and B is the slope (obtained from Figure 4.1), theese parameters are derived for different regions of η, and the results are shown in Table 4.1. There is a separate set of corrections for those b quarks that are tagged by soft muons, and these corrections are also described in Refs. [43], [44] and [45], but we will concentrate only on the untagged b quarks in this dissertation.

2. The η-dependent corrections, unlike the out-of-cone corrections that depend only on Monte Carlo simulated $t\bar{t}$ events, are data driven, and used to ensure the consistency of MC with data. These are also part of the standard $t\bar{t}$ mass analysis in the single-lepton channel at DØ.

The η-dependent corrections are obtained after applying the out-of-cone corrections, and are based on events with only one "photon" and one jet (γ+jet). These are not pure direct-photon events, but rather any highly electromagnetic γ-like showers produced in association with an opposing jet. Because the electromagnetic energy scale is well calibrated, the jet E_T is compared with that of the photon. The deviation from unity in jet energy scale can be measured by the fractional difference (ΔS) in E_T between the jet and the photon:

$$\Delta S = \frac{E_T(jet) - E_T(\gamma)}{E_T(\gamma)} \quad . \tag{4.7}$$

The value of ΔS is averaged over large samples of events, as a function of η, and the results are shown in Fig. 4.2 for data and for MC simulations. These plots provide two functions, one to correct the data and one to correct the MC events, and define the final corrected jet energies (independent of jet type).

The η-dependent corrections are referenced to all the previous levels of energy corrections, those intrinsic to the simple-cone clustering algorithm [42] and to the out-of-cone corrections [43, 44, 45]. If those are changed, then the η-dependent corrections must be re-examined as well.

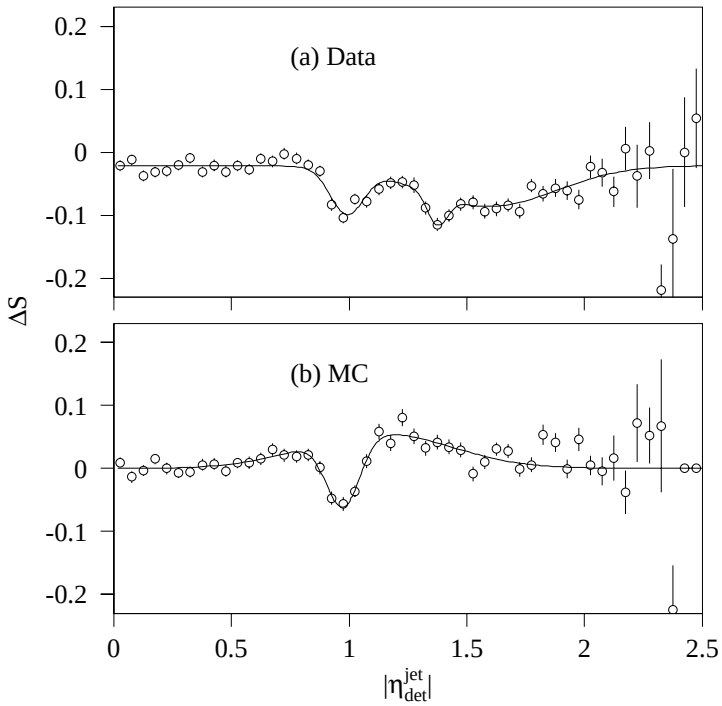

Figure 4.2: Dependence of the deviation in the jet energy scale (ΔS) for γ+jets data and $t\bar{t}$ MC events, as a function of $|\eta|$ [45].

The Transfer Functions.

In our analysis we also consider an alternative approach to the problem of jet energy corrections. We take account of the fact that energy losses due to hadronization and radiation are strongly asymmetric relative to the original parton energy. This will be described in Chapter 5.

Chapter 5

Mapping Between Jet and Parton Energies.

The standard jet energy corrections used in previous top quark mass measurements at DØ correct the energies of a jet (rather than E_T values) in such a way that, for a given η-region and a given parton energy range, the difference between the corrected jet energy (E_{corr}) and the parton energy E_{parton} has a mean equal to 0, that is

$$< \delta_E^{corr} >=< E_{corr} - E_{parton} >_{\eta, E_{parton}} = 0 \quad . \tag{5.1}$$

However, these corrections do not account for the shape of the uncorrected $\delta_E = E_{jet} - E_{parton}$ distribution shown in Figure 5.1. These distributions are clearly not

symmetric, with a significant tail at negative values. Consequently, correcting for the mean, and then considering just a Gaussian resolution around the corrected energy, can often yield to an underestimation of jet energy.

Because an extraction of the correct mass of the top quark requires unbiased parton energies to be estimated from the energies of the jets, it is important to consider the asymmetries in Figure 5.1.

5.1 Transfer function and production probability.

Each of the plots shown in Figure 5.1 corresponds to a distribution in $N(\delta_E)$ that can be calculated as follows

$$N(\delta_E) = \int n(E_{parton}) W(E_{parton}, E_{parton} + \delta_E) dE_{parton} \quad , \tag{5.2}$$

where $n(E_{parton})$ is the original density distribution function of parton energies in the sample, and $W(E_{parton}, E_{parton} + \delta_E)$ is the probability density to have $E_{jet} = E_{parton} + \delta_E$, given a parton energy E_{parton}. The mapping between parton energies and jet energies is determined by $W(E_{parton}, E_{jet})$, and to extract it from Eq.(5.2) requires knowledge $n(E_{parton})$.

Because $W(E_{parton}, E_{jet})$ should not depend on the mass of the top quark, a large sample of jets was generated using $t\bar{t}$ events for m_t = 140, 160, 175, 190 and

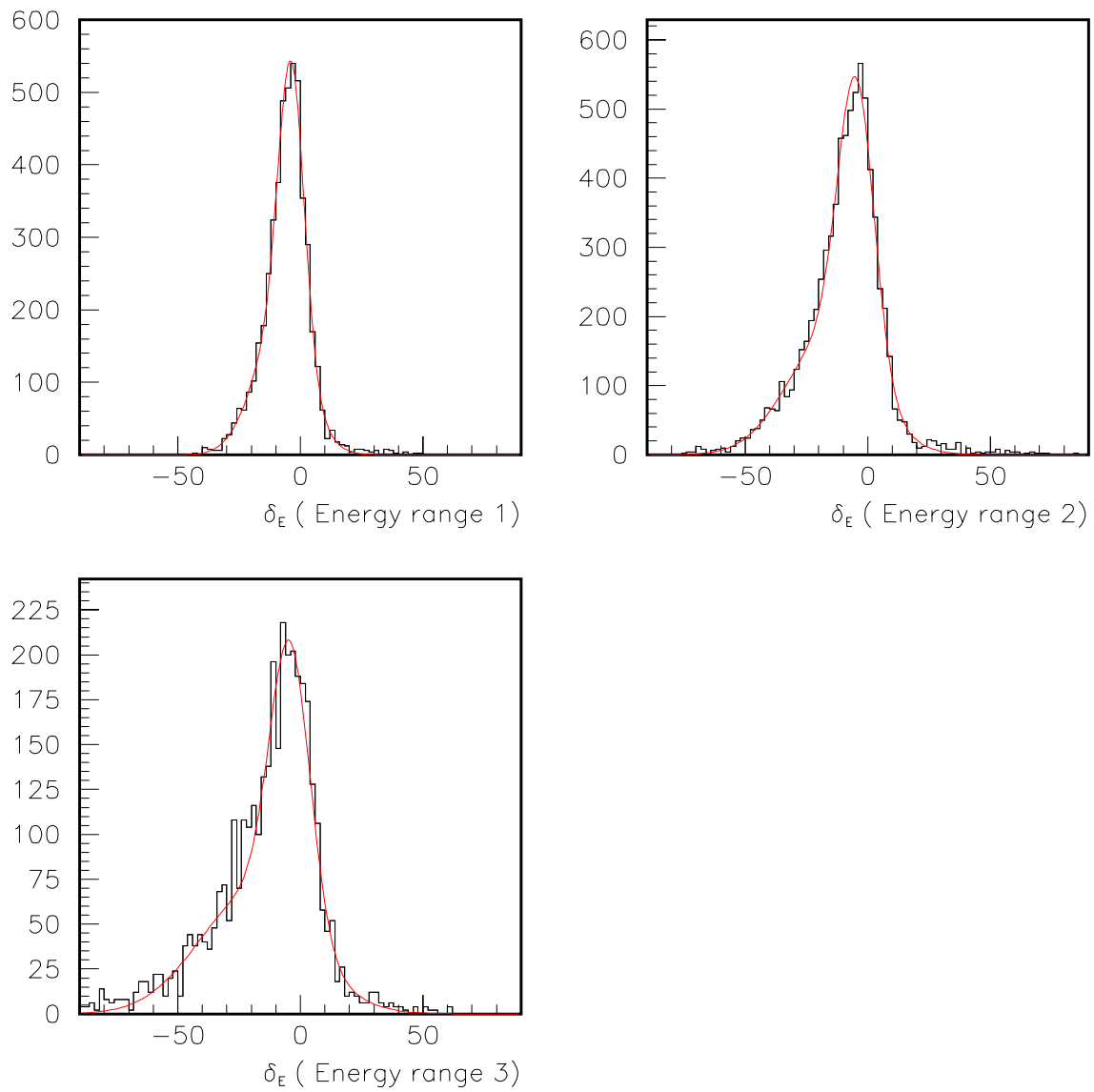

Figure 5.1: Distributions in $\delta_E = E_{jet} - E_{parton}$ for different parton energy ranges (E range 1: 15 GeV $< E_{parton} <$ 60 GeV, E range 2: 60 GeV $< E_{parton} <$ 100 GeV, E range 3: 100 GeV $< E_{parton} <$ 140 GeV, for jets in $t\bar{t}$ event with $0.2 < |\eta| < 0.6$). The distributions have an extended tail for $\delta_E < 0$, which corresponds to the effect of hadronization and radiation.

200 GeV. Only those jets that could be matched to partons were selected for further study. The distribution $n(E_{parton})$ was then parameterized for the remaining partons in terms of E_{parton} and η, and, with the known the shape of $N(\delta_E)$, used to obtain $W(E_{parton}, E_{parton} + \delta_E)$.

5.2 Parameterization of the transfer functions.

The smooth lines in Figure 5.1 correspond to fits to the histograms using the functions:

$$F(\delta_E) = [\exp \frac{-(\delta_E - p_1)^2}{2p_2^2} + p_3 \exp \frac{-(\delta_E - p_4)^2}{2p_5^2}] \quad . \tag{5.3}$$

$F(\delta_E)$ is simply a sum of two Gaussians, one to account for the sharp peak and the other to fit the asymmetric tails, used to approximate $N(\delta_E)$. The transfer function is then defined as $W(E_{parton}, E_{jet}) = F(E_{jet} - E_{parton})$.

As can be seen in Figure 5.1, the parameters for Eq.(5.3) depend on parton energy. This could be accounted for in the ensuing by binning jets in energy and then calculating p_i for each bin. In this way a transfer function would be generated for each energy range, in the manner of the standard DØ energy corrections of Section 4.3.1. Instead of doing the binning in energy, we account for the variation

Table 5.1: Parameters for $W(E_{parton}, E_{jet})$

	Light quark jets		Untagged b jets	
$p_i = a_i + b_i \times E_{parton}$	a_i	b_i	a_i	b_i
p_1 (GeV)	-1.65	-0.038	-3.41	-0.0333
p_2 (GeV)	2.84	0.067	3.98	0.0673
p_3 (dimensionless)	0.000	0.0013	0.000	0.00179
p_4 (GeV)	11.56	-0.302	3.36	-0.227
p_5 (GeV)	10.73	0.173	15.17	0.138

by assuming a linear dependence of the p_i on E_{parton}, that is,

$$p_i = a_i + b_i E_{parton} \quad . \tag{5.4}$$

This yields a total of 10 parameters $(a_1, b_1, ..., a_5, b_5)$ defining the transfer function.

The values of a_i and b_i where found from a likelihood fit to the whole sample of jets associated with partons, using the $n(E_{parton})$ density as discussed in the previous section. The fits were done separately for light quarks and for b quarks. The results are given in Table 5.1.

The quality of the parameterization can be checked by comparing the two-dimensional distributions in (E_{parton}, E_{jet}) with the prediction using the transfer functions and $n(E_{parton})$, as given in Eq. (5.2). Figure 5.2 shows "lego" plots for the region $0.2 < |\eta| < 0.6$, and the corresponding contour plots are shown in Figure 5.3. It is hard to compare two-dimentional histograms, and for this reason representative slices of E_{parton} and E_{jet} are shown in Figures 5.4 and 5.5, repectively. These plots

indicate that the parametrization is indeed excellent for $0.2 < |\eta| < 0.6$. However, for the region $1.3 < |\eta| < 2.0$, the parameterization does not reproduce the distribution in the MC sample, as can be seen in Figure 5.6. There is a significant excess in regions where the jet energy is higher than the parton energy, which is not the case for more central jets. This effect may be due to the presence of initial-state radiation that overlaps the jet cone of forward jets, and requires further study. The impact of this bias on our analysis is not very strong because jets from $t\bar{t}$ events are produced mainly at central η values.

5.3 Test of the Transfer Function.

The point of the transfer functions is to model the smearing in jet energies produced by the combined effects of radiation, hadronization, measurement resolution and jet reconstruction algorithm. One way to check that such a function is correct, is to use it to smear the energies of objects generated at the parton level, and see whether the distributions of the modified kinematic variables agree with those obtained from jets reconstructed via full detector simulation.

Once the parameterization of the transfer function $W(E_{jet}, E_{parton})$ is obtained, it can be used to predict distributions of any reconstructed quantities in Monte Carlo $t\bar{t}$ events. As an example, the distribution of the invariant mass of three reconstructed

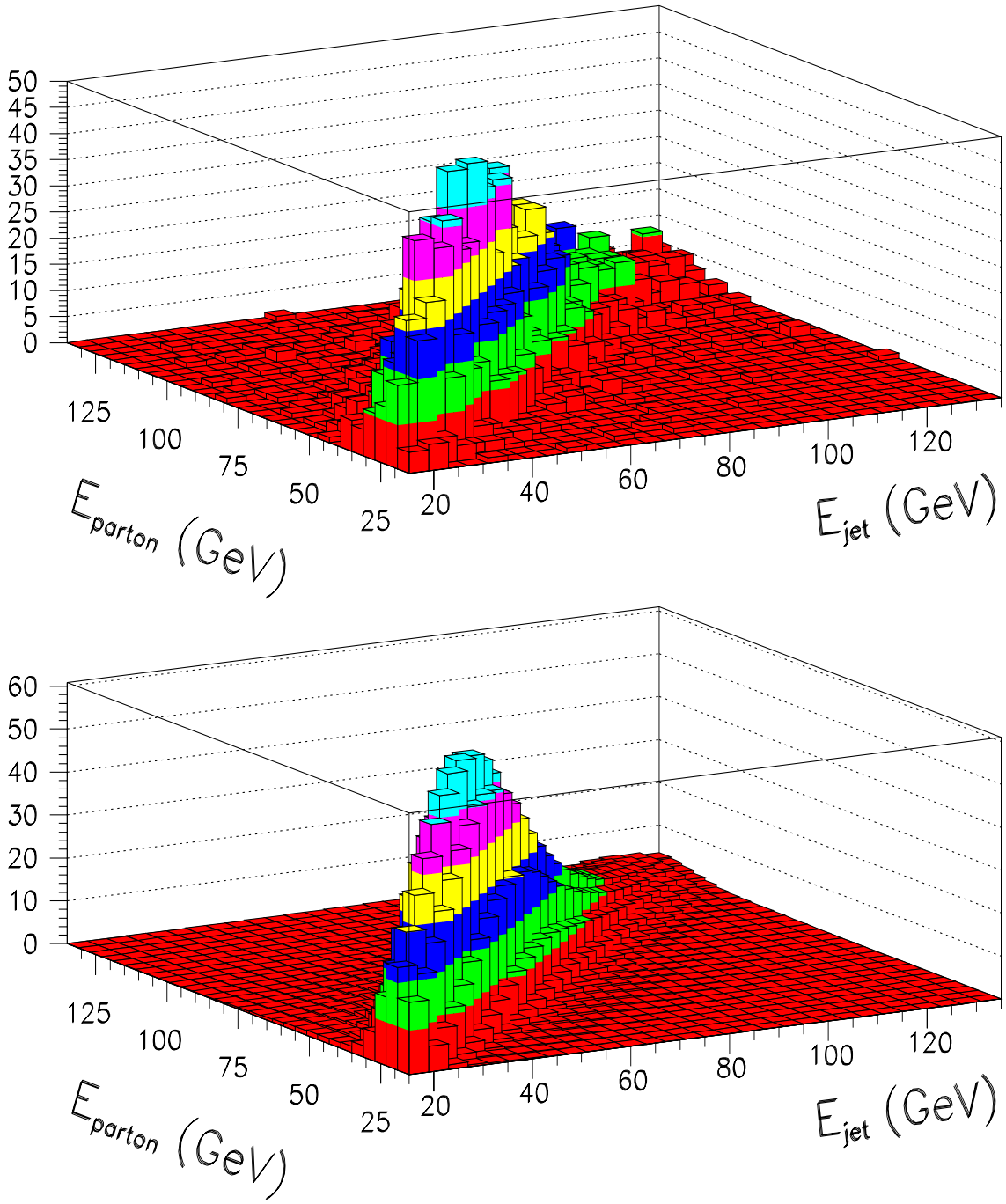

Figure 5.2: Top: lego plot of E_{parton} vs E_{jet} for a sample of jets associated with partons in $t\bar{t}$ Monte Carlo events, using full DØ detector simulation (CAFIX corrections included). Bottom: lego plot of E_{parton} vs E_{jet}), where E_{parton} is predicted using $n(E_{parton})$ and the transfer function described in Eq.(5.2). The jets are in the region of $0.2 < |\eta| < 0.6$.

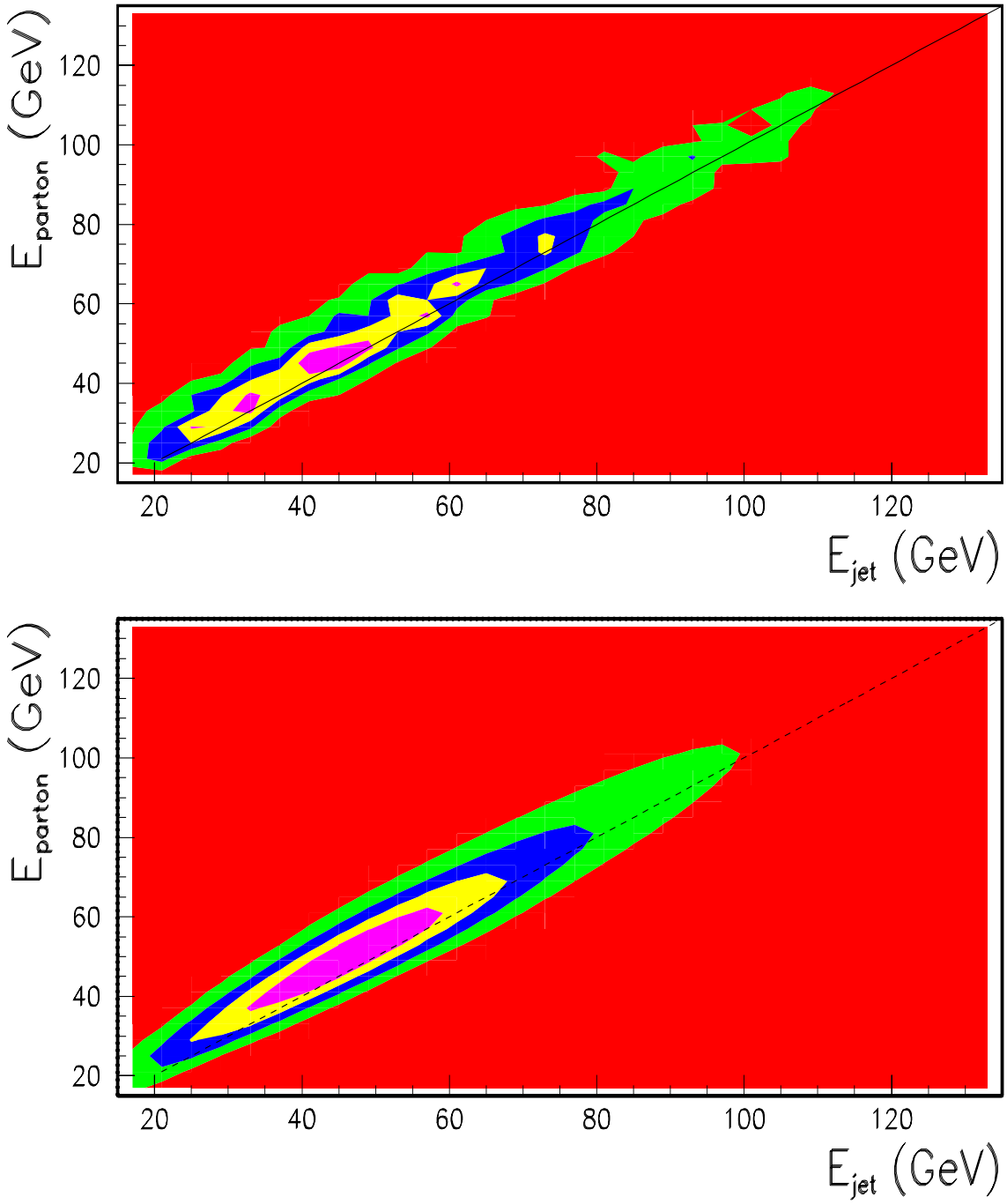

Figure 5.3: Contour plots corresponding to Figure 5.2. The different shadings correspond to different number of events (40, 30, 20, 10 and 5).

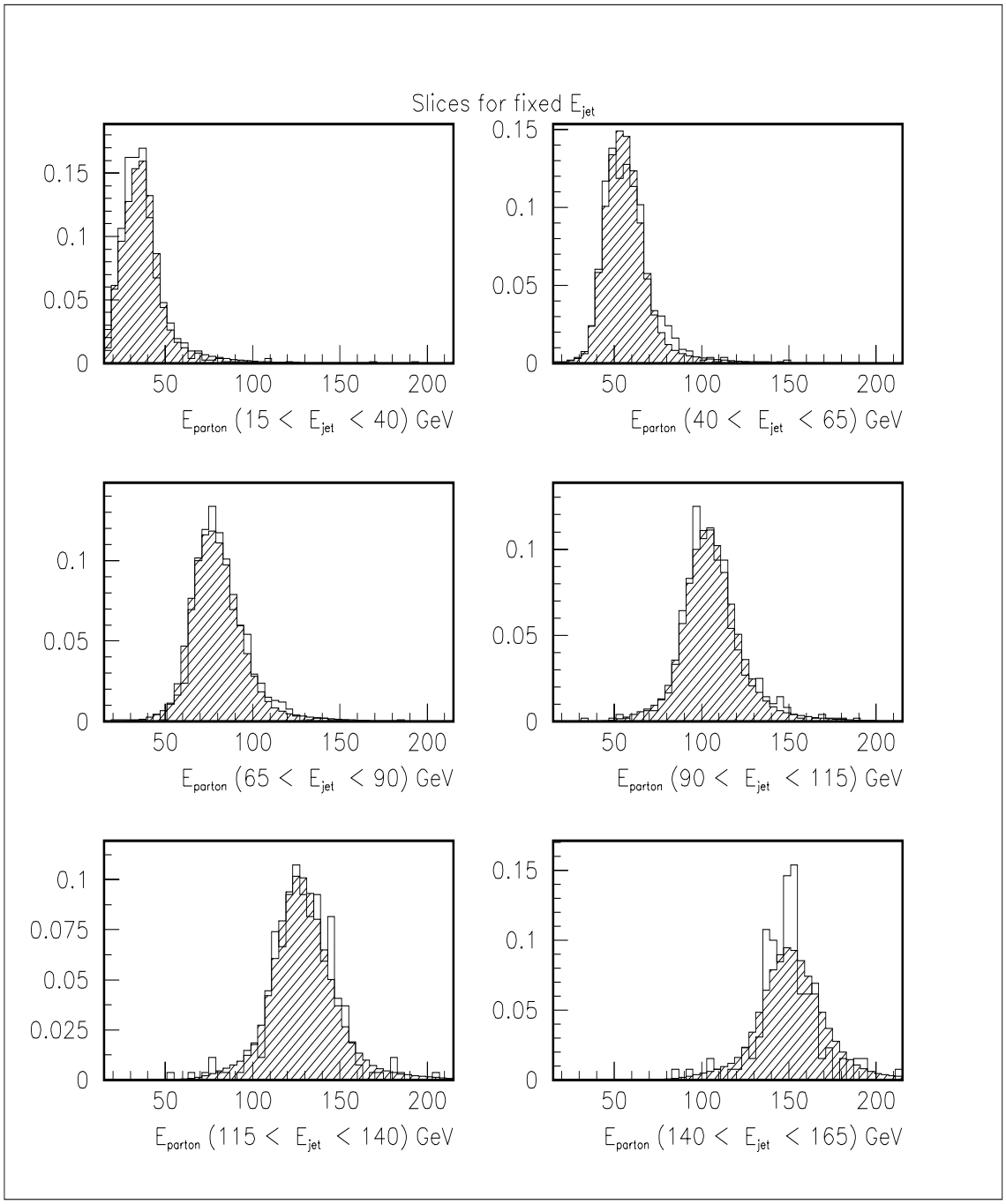

Figure 5.4: Slices of E_{jet} from the plots in Figure 5.2. The filled histogram correspond to predictions using $n(E_{parton})$ and the transfer function, and the lines correspond to the original MC simulated events.

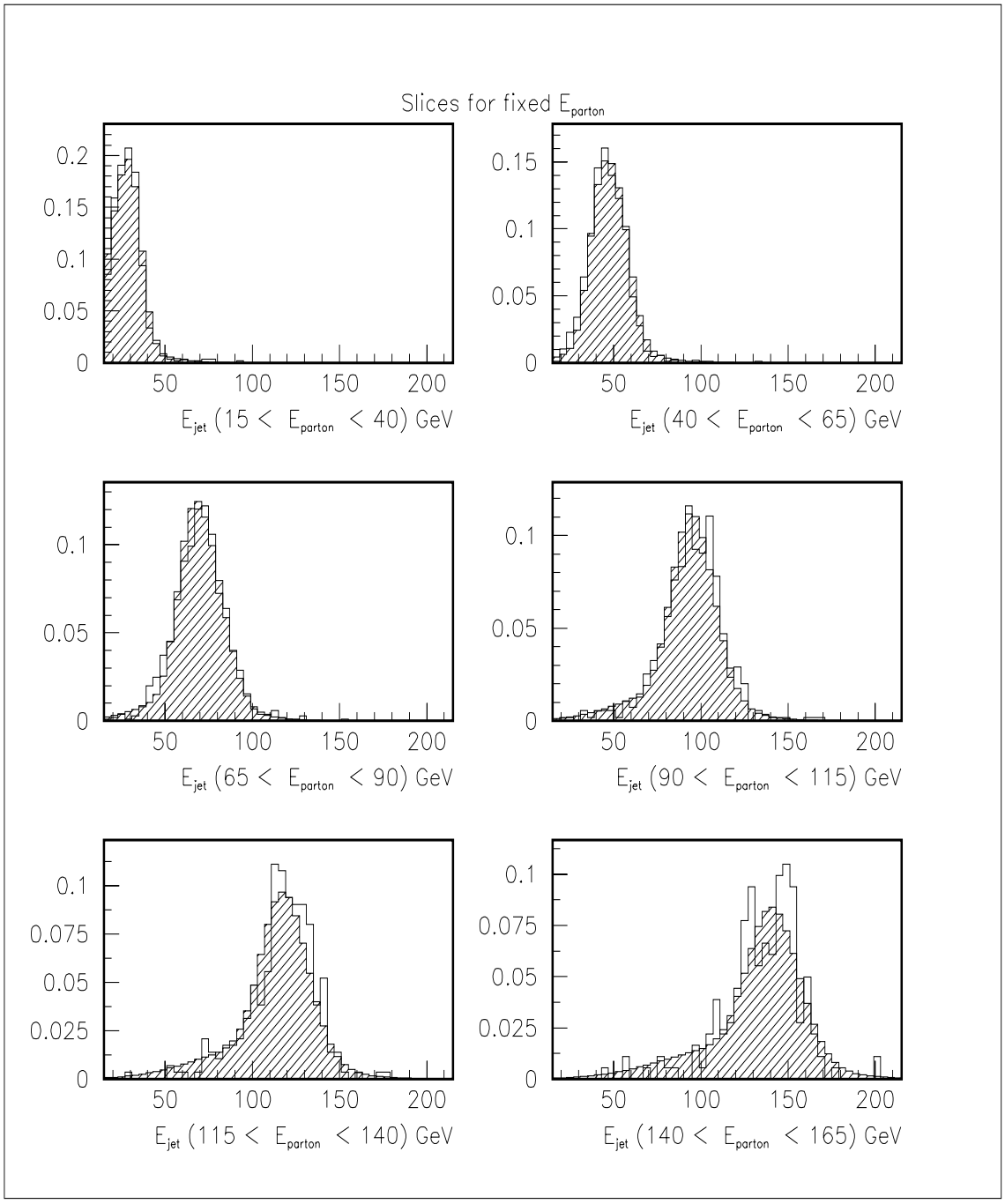

Figure 5.5: Same as Figure 5.4, but now the slices in E_{parton}

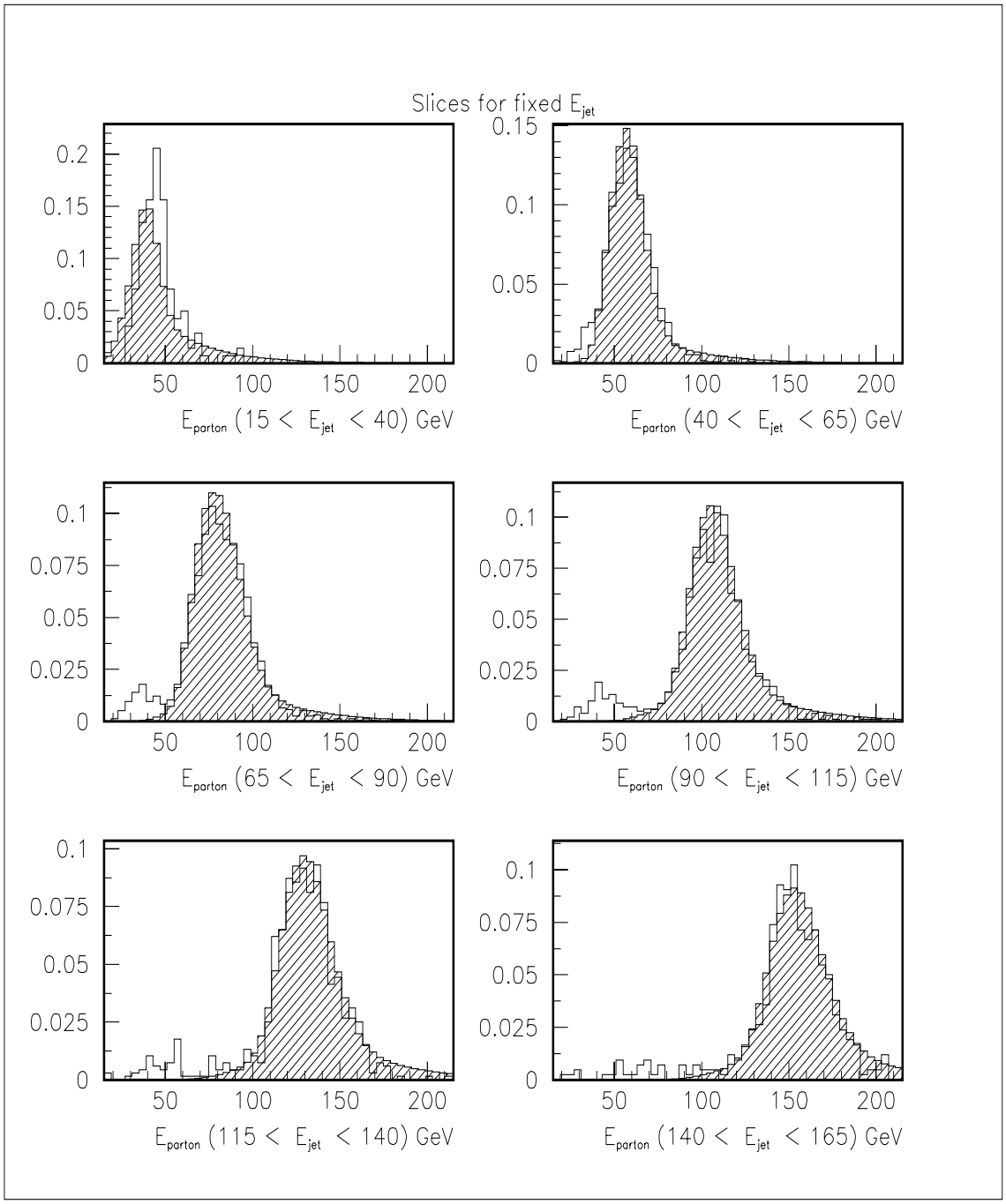

Figure 5.6: Slices in E_{jet}, same plots as in Figure 5.4, but now for jets in the region $1.3 < |\eta| < 2.0$.

jets with CAFIX corrections only (the jets being identified in the MC as coming from the hadronic decay of the top quark) is compared with the prediction using our transfer function in Figures 5.7 and 5.8. Good agreement is observed between the full D0 simulation (histograms) and the predictions from the transfer function (smooth curves) for the shapes of the distributions. However, there is apparent a small difference ($\approx$ 2 GeV shift in the means). The origin of this discrepancy has yet to be investigated.

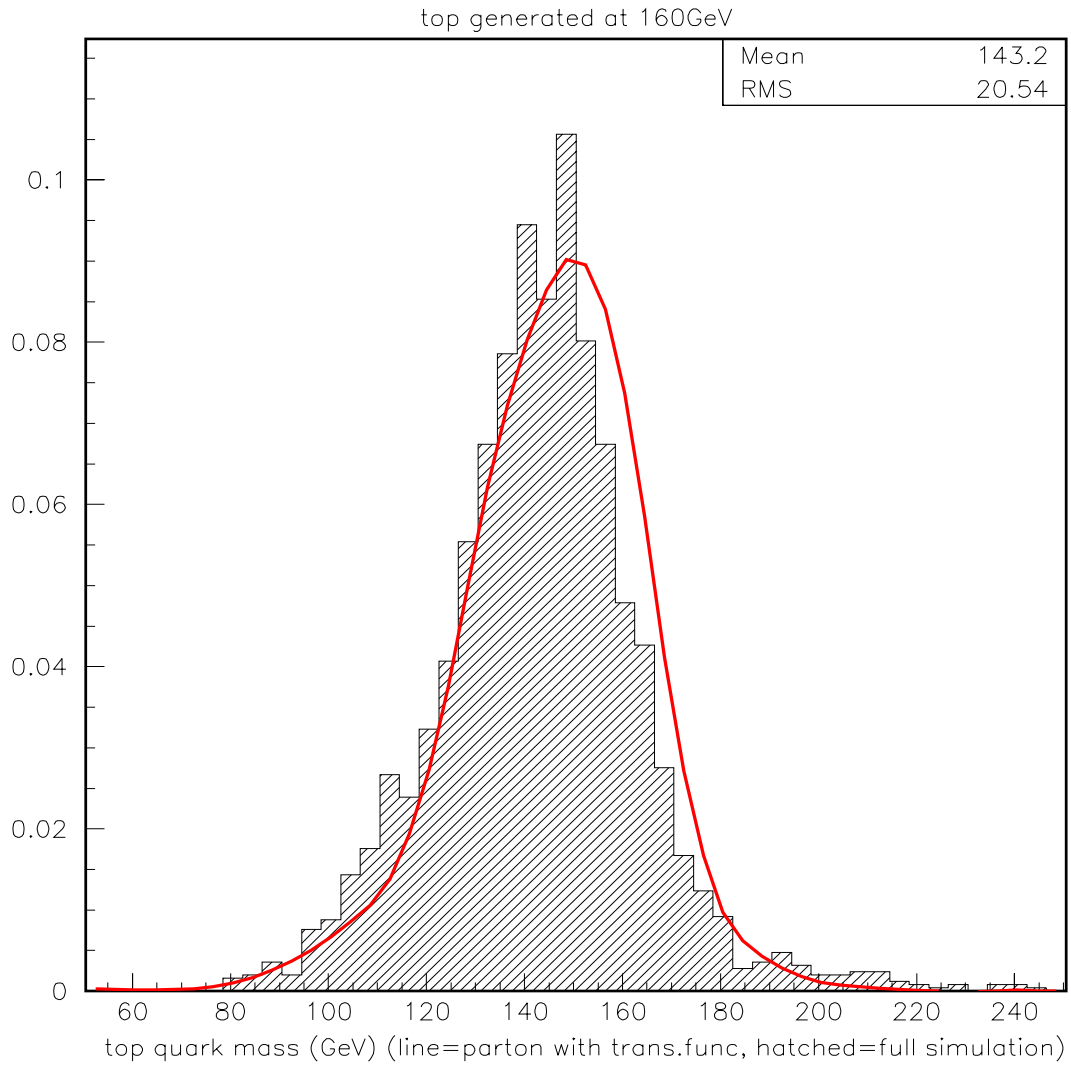

Figure 5.7: Distribution of the invariant mass of three jets with full DØ simulation and CAFIX energy corrections (jets identified in Monte Carlo as coming from the hadronic decay of the top quark) is compared with the prediction from the transfer function. The comparison is done for events simulated with m_t=160 GeV. The mean and RMS values correspond to the hatched histogram.

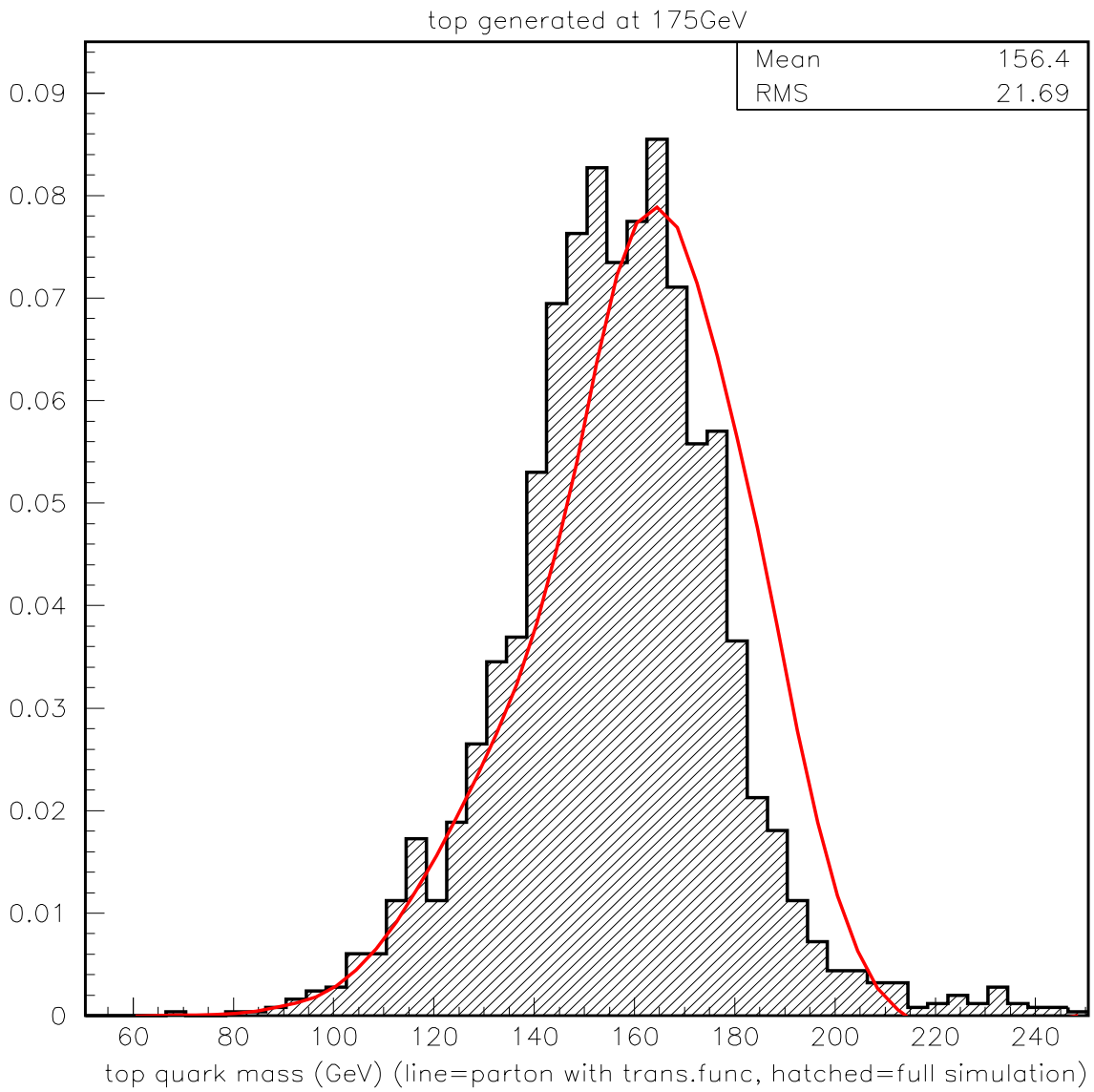

Figure 5.8: Same as Figure 5.7, but now m_t=175 GeV.

Chapter 6

The Method of Analysis.

6.1 Introduction.

In searching for new physics, one is often faced with the challenge of extracting a small signal from a much larger background. In such situations, it is desirable to use as many variables as possible to differentiate between signal and background events.

In the top studies carried out by DØ[45], or in methods proposed to search for the Higgs boson [46], a reduced set of variables is used to characterize individual events. Examples of the variables normally used in such analyses are eigenvalues of the momentum tensor in an event (e.g., aplanarity), transverse momentum imbalance (missing E_T), the sum of the scalar E_T of jets in an event (H_T), etc. Using Monte Carlo (MC) techniques, probabilities for an event being background or signal are

then calculated as a function of these variables, and in the extraction of signals the events are "weighted" according to these probabilities, for example, by using a Neural Network discriminant [45].

A reduced set of variables is often chosen because of the expense of generating enough MC events to get an accurate parameterization of a function of many variables. For example, for single-lepton $t\bar{t}$ events, with $t\bar{t} \rightarrow W^{+}bW^{-}\overline{b} \rightarrow l\overline{\nu}_{l} + \overline{q}q'bb$ (lepton + 4 jets), 15 variables are needed to fully characterize the event. If all 15 variables were used, and only 3 points per variable were sampled, then $3^{15} \sim 1.4 \times 10^{7}$ MC events would have to be generated to parameterize the probability.

It is worth pointing out that the MC programs used to generate events for parameterizing these probabilities, for example for training Neural Networks, already have such probabilities embedded in the event generator. It can therefore be argued that the best way to handle situations in which the background cannot be eliminated by using simple cutoffs, is to use the probabilities provided in the MC. In this way, all the variables in an event can be used to characterize the event, which maximizes the input information that goes into the analysis, and can therefore reduce statistical uncertainties in the measurement of any quantitative feature or parameter.

Our general method will be discussed in Section 6.2. The calculation of probabilities will be addressed in Section 6.3. Section 6.4 will cover the calculation of the probability for single-lepton $t\bar{t}$ events. The calculation of background from

W+jets will be addressed in Section 6.2.4. And, finally, several examples of analyses based DØ MC events will be given in Chapter 7. For completeness, more details for selected calculations are included in the Appendices.

6.2 The General Method.

6.2.1 Definition of Extended Likelihood.

Let us assume that we have a full event specified by a set of coordinates x_1 in a volume dx_1, another with coordinates x_2 in volume dx_2, a third one with coordinates x_3 in volume dx_3, etc, as shown in the following sketch:

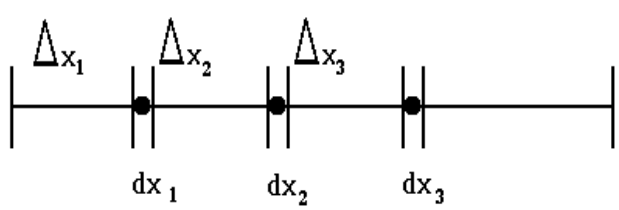

The coordinates of each x_i represent any relevant set of variables that are needed to specify an event in a unique way. The probability (up to a normalization constant) for obtaining any configuration of N observed events within the infinitesimal phase space volume elements dx_i, containing empty finite elements Δx_i, with $i = 1, 2, ..., N$, can be written as

$$
\begin{aligned}
P(\text{configuration}) = & Prob\begin{pmatrix} 0 & \text{events} \\ \text{in} & \Delta x_0 \end{pmatrix} \times Prob\begin{pmatrix} 1 & \text{event} \\ \text{in} & dx_1 \end{pmatrix} \\
& \times Prob\begin{pmatrix} 0 & \text{events} \\ \text{in} & \Delta x_1 \end{pmatrix} \times Prob\begin{pmatrix} 1 & \text{event} \\ \text{in} & dx_2 \end{pmatrix} \quad \ldots.
\end{aligned} \tag{6.1}
$$

Using Poisson statistics, the probabilities for having zero and one event, when the expected average is $\overline{n}$, are

$$
P_{0,\overline{n}} = e^{-\overline{n}} \quad \text{and} \quad P_{1,\overline{n}} = \overline{n}e^{-\overline{n}} \quad . \tag{6.2}
$$

If N is the number of observed events, and $\overline{P}(x)$ is the probability density for all coordinates (which we will not normalize to unity for the most general case), then the average number of events expected in any volume Δx is

$$
\overline{n} = N \int_{\Delta x} \overline{P}(x) dx \quad , \tag{6.3}
$$

and the probability of having 0 events in the region Δx is

$$P_0(\Delta x) = e^{-N \int_{\Delta x} \overline{P}(x) dx} \quad . \tag{6.4}$$

Similarly, the probability of having 1 event in the differential region dx around x is

$$P_1(x)dx = N\overline{P}(x)dx \quad e^{-N\overline{P}(x)dx} \quad . \tag{6.5}$$

The total probability in Eq.(6.1) will then be given by the product off all such terms:

$$P(\text{configuration}) = e^{-N \int_V \overline{P}(x) dx} \prod_{i=1}^{N} N\overline{P}(x_i) dx_i \quad , \tag{6.6}$$

where V is the volume of our entire space.

Although a one dimensional sketch was used to motivate Eq. (6.6), the result is clearly general. If $\overrightarrow{x}_i$ is a point in a k-dimensional volume (V), then the probability for having no events in the volume defined by V, but corrected for the infinitesimal elements ("holes") around the N points $\overrightarrow{x}_i$, is

$$e^{-N\int_{V-holes}\overline{P}(\overrightarrow{x}_i)d^k\overrightarrow{x}_i} \quad , \tag{6.7}$$

and the probability for having one event in each of the N holes is

$$\prod_{i=1}^{N} N\overline{P}(\overrightarrow{x}_i)d^k\overrightarrow{x}_i \quad e^{-N\overline{P}(\overrightarrow{x}_i)d^k\overrightarrow{x}_i} \quad . \tag{6.8}$$

The multiplication of Eqs. (6.7) and (6.8), yields Eq.(6.6) for the case of many dimensions. To simplify the notation, the vectorial arrows will be dropped, but the x_i will always refer to a point in a multidimensional space.

$P(x_1...x_N)$ is the probability density for observing the N events characterized by $x_1, x_2, ..., x_N$, and it should always be at (or very near) its maximum value. If this were not the case, then a very different set of events would have been observed. In most applications, the single-event probability $\overline{P}(x)$ can be specified only as a function of some unknown set of parameters α. That set is then estimated by maximizing the "extended" likelihood function $P(x_1...x_N)$. Terms that do not depend on α (e.g. N^N) are usually not included in $P(x_1, ..., x_N)$, because they do not affect the values of the parameters α that maximize the likelihood. It can be shown that

the best (unbiased) estimate of a given set of parameters is obtained through the maximization of a differential likelihood [21]:

$$L(\alpha) = e^{-N\int \overline{P}(x;\alpha)dx} \prod_{i=1}^{N} \overline{P}(x_i;\alpha) \quad . \tag{6.9}$$

$L(\alpha)$ usually varies rapidly as a function of α, and consequently it is easier to maximize $\ln L$. In fact, it is common practice to minimize $-\ln L$:

$$-\ln L(\alpha) = -\sum_{i=1}^{N} \ln \overline{P}(x_i;\alpha) + N \int \overline{P}(x;\alpha)dx \quad . \tag{6.10}$$

6.2.2 Detector Acceptance Corrections.

Because the parameters are estimated using observed events, $\overline{P}(x)$ is a "measured" probability distribution. This probability density receives contributions from all the processes that lead to the final state observed in the detector. For example, an event with four jets, an electron and missing E_T, can be a $t\bar{t}$ event, or a W + 4-jets, or a five-jet event in which one jet was not properly reconstructed or it fluctuated to mimic an electron, or it can be a W + 3-jets event in which a jet split in two, etc.

In general, the probability that an event is accepted as a candidate for further

study will depend only on the specific characteristics of that event, and it will be independent of the process that produced it. The measured differential probability can be related to the "production", or inherent, probability distribution $P(x, \alpha)$ through the acceptance of the detector:

$$\overline{P}(x;\alpha) = Acc(x)\ P(x;\alpha) \quad , \tag{6.11}$$

where $Acc(x)$ includes all conditions for accepting or rejecting an event, such as the geometric acceptance, trigger efficiencies, reconstruction efficiencies, selection criteria, etc. Clearly, the detector acceptance is independent of the α parameters that are to be estimated. For example, if an electron is detected with a certain momentum $\overrightarrow{p_e}$, the detector should be insensitive to whether the electron came from a W decay or a Z decay or any other process. The "production" probability is calculated using the differential cross section, summed over all processes that contribute to the same final state, and this is convoluted with the resolution and acceptance of the detector.

The result of inserting Eq.(6.11) into Eq.(6.10) is

$$\boxed{-\ln L(\alpha) = -\sum_{i=1}^{N} \ln P(x_i;\alpha) + N \int Acc(x) P(x;\alpha) dx} \quad . \tag{6.12}$$

where the term $-\sum \ln Acc(x_i)$ has been dropped because it is independent of the α parameters, and will therefore not affect the minimization. The integral in Eq.(6.12) is calculated using Monte Carlo techniques, where the value of $Acc(x)$ is 1 if the event is accepted, and 0 otherwise. The integral is sampled through random numbers generated uniformly in dx, and can be written as:

$$\int Acc(x) P(x;\alpha) dx = [\int dx] \sum_{j=accep.} P(x_j;\alpha) \quad , \tag{6.13}$$

where the sum is over the events accepted in the sample.

To simplify the notation, the specific mention of α will frequently be dropped from our expressions. However, in general, it should be recognized that: 1) the variables x_i used to specify the ith event are constants during the minimization process, and 2) that $P(x)$ is always a function of the α parameters that are estimated by minimizing Eq.(6.12).

6.2.3 Normalizing $P(x)$

When $\overline{P}(x;\alpha)$ is normalized to unity, the integral in Eq.(6.10) and Eq.(6.12) can be dropped. Very often, however, $\overline{P}(x;\alpha)$ is a complex function of several parameters, and the normalization usually depends on the acceptance, which has uncertainty. In such cases, it is unwise to normalize $\overline{P}(x;\alpha)$ during the minimization process, but rather to allow the normalization to float, making it an additional parameter in the minimization. Nevertheless, the minimization procedure will assure a properly normalized probability. This can be seen by replacing $\overline{P}(x;\alpha)$ by $c\overline{P}(x;\alpha)$ in Eqs. (6.11) and (6.12), and minimizing with respect to c:

$$-\ln L = -N\ln c - \sum_{i=1}^{N} \ln P(x_i;\alpha) + Nc\int Acc(x)P(x;\alpha)dx \tag{6.14}$$

$$\frac{\partial(-\ln L)}{\partial c} = -\frac{N}{c} + N\int Acc(x)P(x;\alpha)dx = 0 \quad \Rightarrow \quad \frac{1}{c} = \int Acc(x)P(x;\alpha)dx \tag{6.15}$$

that is, $c = \frac{1}{\int AccPdx}$, which normalizes the probability.

At times, the normalization parameter may be correlated with the other parameters. In such cases, the uncertainties on the parameters α can increase, and it is therefore advantageous to keep the probability normalized.

6.2.4 Maximum Likelihood for Signal and Background

For analyses in particle physics, it is usually not possible to completely separate signal events from background. A significant amount of background makes it difficult to extract information about the events of interest.

The maximum likelihood method can be generalized to encompass background by considering that the probability of observing x_i that can originate from several components:

$$P(x) = \sum_{j=1}^{K} \beta_j P(x; j) \quad , \tag{6.16}$$

where $j = 1, 2, .., K$ represent all possible contributions to the total result, and $P(x; j)$ is the probability of measuring x from a particular type of source of events j. The normalization constraint gives

$$\sum_{j=1}^{K} \beta_j = 1 \tag{6.17}$$

The main background for this analysis is from production W+jets. This background probability was calculated by F.A. Berends, H. Kuijf, B. Tausk and W.T. Giele, and implemented in a subroutine that is part of VECBOS [48]. We use this subroutine to obtain the probability of an event being W+jets.

For any event, the probability is now

$$P(x; c_1, c_2, \alpha) = c_1 P_{t\bar{t}}(x; \alpha) + c_2 P_{vecbos}(x) \tag{6.18}$$

For each value of α (the mass of the top quark in our analysis), we find the most probable values of c_1 and c_2, then we search for the most probable mass. The probability $P(x; c_1, c_2, m_t)$ is automatically normalized after the minimization process.

6.3 General Calculation of $P(x)$

If the resolution of the detector is very good, and the beam energies are well known, then the differential probability $P(x)$ for any signal is proportional the differential

production cross section. When the reaction is initiated by partons, and the resolution of the detector cannot be ignored, then the cross section has to be multiplied by the parton distribution functions and the detector resolution, and then integrated over the production variables. Following the Particle Data Group (PDG), the differential cross section will be written as [36]:

$$d^n\sigma = \frac{(2\pi)^4|M|^2}{4\sqrt{(q_1.q_2)^2 - m_1^2 m_2^2}} \quad d\Phi_n(q_1 + q_2; p_1, ..., p_n) \quad , \tag{6.19}$$

where $d\Phi_n$ is an element of n-body phase space, q_i are the incident and p_i the final-state momentum four-vectors, M is the transition matrix element, and m_1 and m_2 are the masses of the incident partons.

The phase space factor can be written as:

$$d\Phi_n(Q; p_1, ..., p_n) = \delta^4(Q - \sum_{i=1}^{n} p_i) \prod_{i=1}^{n} \frac{d^3 p_i}{(2\pi)^3 (2E_i)} \quad , \tag{6.20}$$

where Q is the four-vector for the incident partons, and E_i are the energies of the final state objects. If $f(q)dq$ is the probability that a parton carries a momentum between q and $q + dq$, then

$$P(x) = \int d^n\sigma(y) dq_1 dq_2 f(q_1) f(q_2) W(y,x) \quad , \tag{6.21}$$

where $y = (p_1, ..., p_n)$ represents all the variables needed to specify the reaction, and $W(y,x)$ is the probability of measuring x when y was produced. W equals 1.0 when the final state object is not measured, as is the case for neutrinos, it is a Gaussian-like function when the resolution is to be taken into account, and it is a δ-function for variables that are very well measured.

When any contributing processes can interfere in a final state, all their amplitudes must be added coherently. If the processes do not interfere, then jut the probabilities can be added. Because, in general, it is not possible to distinguish jets in a $t\overline{t}$ final state, e.g., which jets are b quarks and which are remnants of $W \rightarrow q'\overline{q}$ decay, the probability must be evaluated for all possible combinations of jets that comprise the $t\overline{t}$ final state. Thus, the probability must be summed over all possible combinations, with their respective weights. In general, probabilities for all processes that can be attributed to the observed final state must be calculated and used in the final likelihood. As mentioned previously, the background to $t\overline{t}$ production in the lepton + 4-jets final state has contributions from $W+$ jets and from all-jets events. However, in this analysis we will calculate the likelihood considering

only the W+jets contribution to single-lepton $t\overline{t}$ events. Consequently, $P(x)$ will be defined purely by a sum of the $t\overline{t}$ signal and the W+jets background.

An explicit treatment of the background from jet production can only improve the sensitivity of this analysis, and will be developed in the near future.

6.4 Calculation for Single-Lepton $t\overline{t}$ Events

For $t\overline{t}$ events observed by CDF and DØ [45], the top (antitop) quark decays into W^+b ($W^-\overline{b}$) in a rapid decay process. This is followed by the W^+ (W^-) hadronic $u\overline{d}, c\overline{s}$ ($\overline{u}d, \overline{c}s$) or leptonic $l^+\nu$ ($l^-\overline{\nu}$) decays. The sum of the hadronic modes is approximately six times the rate for each of the leptonic channels.

When both W^+ and W^- decay leptonically, the signature involves two isolated leptons, two jets (b quarks) and missing energy from the neutrinos that are not detected. These are the so-called dilepton events, and DØ observed seven events of this type in Run I [47].

As mentioned before, when only one W decays leptonicaly, the signature is one lepton, missing E_T, and at least four jets. This signal is not as clean as that for dileptons, but has better statistics, and the background is far smaller than for the case when both W^+ and W^- decay into jets. DØ has 29 events that are candidates for $t\overline{t}$ in the lepton + jets process [45], and we will concentrate on this sample.

6.4.1 The Matrix Element $|M|^2$

The square of the matrix element for the production and decay process $q\overline{q} \to t\overline{t}$ $\to (W^+b)(W^-\overline{b}) \to (\overline{e}\nu b)(d\overline{u}\overline{b})$ (this process corresponds to 90Tevatron), averaged over initial quark color and spins, and summed over the final colors and spins, is given by (see Ref. [49]):

$$
\begin{aligned}
|M|^2 =& \frac{g_s^4}{9} F\overline{F}\Bigg((2-\beta^2 s_{qt}^2) - \\
& \frac{(1-c_{\overline{e}q}c_{d\overline{q}}) - \beta(c_{\overline{e}t}+c_{d\overline{t}}) + \beta c_{qt}(c_{\overline{e}q}+c_{d\overline{q}}) + \frac{1}{2}\beta^2 s_{qt}^2(1-c_{\overline{e}d})}{\gamma^2(1-\beta c_{\overline{e}t})(1-\beta c_{d\overline{t}})} \Bigg) \quad ,
\end{aligned}
\tag{6.22}
$$

where s_{ij} and c_{ij} are the sine and cosine of the angle between particles i and j calculated in the $q\overline{q}$ center of mass (CM), g_s is the strong coupling constant ($g_s^2/4\pi = \alpha_s$), β is the top quark's velocity (relative to the speed of light) in the $q\overline{q}$ CM, and $\gamma = (1-\beta^2)^{-1/2}$. The second line in Eq.(6.22) reflects the $t\overline{t}$ spin correlations. F reflects the production and leptonic-decay kinematics of the top quark ($t \to W^+b \to \overline{e}\nu_e b$):

$$
F = \frac{g_w^4}{4}\left[\frac{m_t^2 - m_{\overline{e}\nu}^2}{(m_t^2 - M_t^2)^2 + (M_t\Gamma_t)^2}\right]\left[\frac{m_t^2(1-\hat{c}_{\overline{e}b}^2) + m_{\overline{e}\nu}^2(1+\hat{c}_{\overline{e}b})^2}{(m_{\overline{e}\nu}^2 - M_W^2)^2 + (M_W\Gamma_W)^2}\right] \quad , \tag{6.23}
$$

where $\hat{c}_{\overline{e}b}$ is the cosine of the angle between $\overline{e}$ and b in the W^+ rest frame, $m_{\overline{e}\nu}$ is the invariant mass of the positron-neutrino system, (M_t,Γ_t) and (M_W,Γ_W) are the masses and widths of the top quark and W boson, and g_w is the weak coupling constant ($G_F/\sqrt{2} = g_w^2/8M_W^2$). Similarly, $\overline{F}$ corresponds to the decay $\overline{t} \to W^-\overline{b} \to d\overline{u}\overline{b}$):

$$\overline{F} = \frac{g_w^4}{4}\left[\frac{m_t^2 - m_{d\overline{u}}^2}{(m_t^2 - M_t^2)^2 + (M_t\Gamma_t)^2}\right]\left[\frac{m_t^2(1-\hat{c}_{d\overline{b}}^2) + m_{d\overline{u}}^2(1+\hat{c}_{d\overline{b}})^2}{(m_{d\overline{u}}^2 - M_W^2)^2 + (M_W\Gamma_W)^2}\right] \quad , \tag{6.24}$$

where $\hat{c}_{d\overline{b}}$ is the cosine of the angle between d and $\overline{b}$ in the W^- rest frame, and $m_{d\overline{u}}^2$ is the invariant mass of the d-$\overline{u}$ system.

None of the current Monte Carlo programs include $t\overline{t}$ spin correlations. Since the examples in this Thesis will deal only with MC events that were generated without the correlation term in Eq.(6.22), this will also be ignored in our analysis. Consequently, Eq.(6.22) reduces to:

$$|M|^2 = \frac{g_s^4}{9}F\overline{F}(2 - \beta^2 s_{qt}^2) \quad . \tag{6.25}$$

It will be assumed that the parton q originated from the proton and $\overline{q}$ with the

antiproton. (We are ignoring the $gg \to t\bar{t}$ component that corresponds to $\approx 10-15\%$ of the yield.) The electron's charge was not measured during D0's Run I, it is therefore not possible to distinguish between t and $\bar{t}$ objects. But since $s^2_{qt} = s^2_{q\bar{t}}$, when there is no gluon radiation, to first order, Eq.(6.25) is invariant with respect to the exchange $t \leftrightarrow \bar{t}$. Also, in the hadronic W decay, it is not possible to differentiate between the two jets. The wrong combination will give $\hat{c}_{\overline{u}\overline{b}} = -\hat{c}_{d\overline{b}}$, which changes Eq.(6.24) to

$$\overline{F} = \frac{g_w^4}{4}\left[\frac{m_t^2 - m_{d\overline{u}}^2}{(m_t^2 - M_t^2)^2 + (M_t\Gamma_t)^2}\right]\left[\frac{m_t^2(1-\hat{c}^2_{d\overline{b}}) + m_{d\overline{u}}^2(1+\hat{c}^2_{d\overline{b}})}{(m_{d\overline{u}}^2 - M_W^2)^2 + (M_W\Gamma_W)^2}\right] \quad , \tag{6.26}$$

For the Monte Carlo examples in this thesis, the matrix element will be given by Eq. (6.25), with F [$\overline{F}$] given by Eq. (6.23) [Eq.(6.26)]. Only twelve assignments of jets to quarks will be relevant, because the combination that interchanges the jets assigned to the W has been considered already, and the exchange $t \leftrightarrow \bar{t}$ leaves the equations invariant. (We will focus on the events that do not have extra jets beyond the canonical four, which reduces statistics, but also reduces the influence of event with any additional gluon radiation.)

6.4.2 The Measurement Probability $W(y, x)$

As indicated previously, $W(y, x)$ is the probability of measuring the set of variables x when the set of variables y was produced. $W(y, x)$ is a δ-function for quantities that are well measured, a Gaussian-like function when measurement error is included, and 1.0 when no measurement is possible (e.g., neutrinos).

The set y represents all the final-state particle momenta at the parton level. For single-lepton $t\bar{t}$ events $y = (\overrightarrow{p}_{quarks}, \overrightarrow{p}_e, \overrightarrow{p}_\nu)$. Since the neutrino is not measured, $x = (\overrightarrow{p}_{jets}, \overrightarrow{p}_e)$. Because of the excellent granularity of the electromagnetic and hadronic calorimeters, the angles can be considered well measured. Also, since the energy of electrons is measured much better than the energy of jets, the momentum of electrons can also be considered as well measured. Momentum smearing will be significant for jets. For $W \to \mu\nu$ events the muon momentum is often not well measured. This correction has not been implemented, and should eventually improve the sensitivity of the analysis.

In this thesis two versions of $W(y, x)$ are used, the difference between them being the way the smearing in jet energies is realized. The first one is based on the standard DØ jet energy corrections described in Section 4.3.1. Here $W(y, x)$ is

$$W(y,x) = \delta^3(\overrightarrow{p}_e - \overrightarrow{p}_e^x) \prod_{i=1}^{4} \frac{1}{\sigma_i\sqrt{2\pi}} \exp\left[-\frac{(p_i - p_i^x)^2}{2\sigma_i^2}\right] \prod_{j=1}^{4} \delta^2(\Omega_j - \Omega_j^x) \qquad (6.27)$$

where $p_i = |\overrightarrow{p}_{quarks}|$ refers to the momenta of the produced quarks, $p_i^x = |\overrightarrow{p}_{jets}^x|$ to the corrected jet momenta, and Ω_j and Ω_j^x are the quark and jet angles. The variables in Eq.(6.27) refer to the overall $p\overline{p}$ center of mass.

The other $W(y,x)$ is derived from the transfer function discussed in Chapter 5. Here the simple Gaussians for the jet energies in Eq.(6.27) are replaced by $F(\delta_E)$ from Eq.(5.3), where δ_E is the difference between the uncorrected jet energy and the parton energy, as defined in Chapter 5.

6.4.3 The Phase Space

The details of the phase space for single-lepton $t\overline{t}$ events are given in Appendix B, and only the main points will be summarized here. To calculate the probability $P(x)$ in Eq.(6.21), an integration must be performed over 20 variables, corresponding to the vector momenta of the six final-state particles (four quarks, a lepton and a neutrino, giving 18 variables), and the longitudinal momenta of the incident partons (2 varialbles). Inside the integrals there are 15 δ-functions. Four for total energy and momentum conservation, eight for the jet angles, and three for the electron's

momentum vector. The calculation of $P(x)$ therefore involves a five dimensional integral. The integral will be performed numerically, and a judicious choice of the five variables of integration is therefore very important.

A possible choice that would require no transformation of variables would be the absolute values of the four quark momenta and the longitudinal momentum of the neutrino. However, this choice has the disadvantage that most of the time the random sampling would be done where the probability is very small. The reason for this is that the matrix element $|M|^2$ is negligible, except near the four peaks of the Breit-Wigners (BW) corresponding to the two top and the two W masses. A better choice of integration variables would therefore appear to be the top and W masses, and the absolute value of momentum of one of the quarks. With this choice, the numerical sampling can be performed only near the BW peaks, and within the limits of resolution of one of the jets. In fact, the integration function that multiplies the BW terms is very smooth, so that even a one-point integration is almost accurate enough to yield a reliable estimate.

As shown in Appendix B, the phase space as a function of $(\overrightarrow{\Omega}_{jets}, \rho_1, M_1, m_1, M_2, m_2, \overrightarrow{p}_e)$ is given by:

$$
\begin{aligned}
d\Phi_6 = & [\delta(E_{q_1} + E_{q_2} - \sum_{i=1}^{6} E_i)] \ [\delta(p^z_{q_1} + p^z_{q_2} - \sum_{i=1}^{6} p^z_i)] \ \frac{d^3\overrightarrow{p}_e}{(2\pi)^3 2E_e} \frac{d\rho_1}{(2\pi)^3 2E_\nu} \prod_{i=1}^{4} \frac{\rho_i^2 d\Omega_i}{(2\pi)^3 2E_i} \\
& \times \frac{dm_1^2}{|2E_1 \frac{\rho_2}{E_2} - 2\rho_1 cos\theta_{12}|} \frac{dM_1^2}{|2E_1 \frac{\rho_3}{E_3} - 2\rho_1 cos\theta_{13} + 2E_2 \frac{\rho_3}{E_3} - 2\rho_2 cos\theta_{23}|} \\
& \times \frac{dm_2^2}{|2E_e \frac{p^z_\nu}{E_\nu} - 2p^z_e|} \frac{dM_2^2}{|2E_e \frac{\rho_4}{E_4} - 2\rho_e cos\theta_{e4} + 2E_\nu \frac{\rho_4}{E_4} - 2\rho_\nu cos\theta_{\nu 4}|} \\
= & \frac{4}{(2\pi)^4} \ \Phi_6 \ [\delta(E_{q_1} + E_{q_2} - \sum_{i=1}^{6} E_i)] \ [\delta(p^z_{q_1} + p^z_{q_2} - \sum_{i=1}^{6} p^z_i)] \\
& \times d^3\overrightarrow{p}_e \ d\rho_1 dm_1^2 dM_1^2 dm_2^2 dM_2^2 \prod_{i=1}^{4} d\Omega_i
\end{aligned}
\tag{6.28}
$$

with

$$
\begin{aligned}
\Phi_6 = & \frac{4}{(4\pi)^{14}} \frac{1}{E_e E_\nu} \prod_{i=1}^{4} \frac{\rho_i^2}{E_i} \\
& \times \frac{1}{|E_1 \frac{\rho_2}{E_2} - \rho_1 cos\theta_{12}|} \frac{1}{|E_1 \frac{\rho_3}{E_3} - \rho_1 cos\theta_{13} + E_2 \frac{\rho_3}{E_3} - \rho_2 cos\theta_{23}|} \\
& \times \frac{1}{|E_e \frac{p^z_\nu}{E_\nu} - p^z_e|} \frac{1}{|E_e \frac{\rho_4}{E_4} - \rho_e cos\theta_{e4} + E_\nu \frac{\rho_4}{E_4} - \rho_\nu cos\theta_{\nu 4}|} \quad ,
\end{aligned}
\tag{6.29}
$$

where $\rho_i = |\overrightarrow{p}^i_{jet}|$, $m_i = M^i_W$ and $M_i = m^i_t$ (event masses).

6.4.4 Calculation of P(x) for $t\bar{t}$ Events

Combining all the pieces, the differential probability $P(x)$ for single-lepton $t\bar{t}$ events can be written as:

$$
\begin{aligned}
P_{t\bar{t}}(x) &= \int d^n\sigma(y) dq_1 dq_2 f(q_1) f(q_2) W(y,x) \\
&= \int \frac{(2\pi)^4 |M|^2 f(q_1) f(q_2) W(y,x)}{4\sqrt{(q_1 \cdot q_2)^2 - m_{q_1}^2 m_{q_2}^2}} d\Phi_6 dq_1 dq_2 \\
&= \int |M|^2 \, \frac{f(q_1)}{|q_1|} \frac{f(q_2)}{|q_2|} \, W(y,x) \, \Phi_6 \, d\rho_1 dm_1^2 dM_1^2 dm_2^2 dM_2^2 \\
&\quad \times \delta(|q_1| + |q_2| - \sum_{i=1}^{6} E_i) \, \delta(q_1 + q_2 - \sum_{i=1}^{6} p_i^z) \, dq_1 dq_2 d^3 \overrightarrow{p}_e \prod_{i=1}^{4} d\Omega_i \quad .
\end{aligned}
\tag{6.30}
$$

The masses and transverse momenta of the initial partons were neglected in the final step of Eq.(6.30). The q_i therefore stand for the longitudinal momenta of the incident partons. The integration over q_1 and q_2 eliminates the two δ-functions in Eq.(6.30). Integration over the momenta of the electrons, and over the solid angles of jets, eliminates the δ-functions associated with $W(y,x)$ (see Eq.(6.27)).

Since there is no way to know which jet is associated with which quark, all possible combinations that can lead to the observed final state in the detector must be included in the calculation. In addition, there are generally two neutrino solutions to the kinematics, both of which must be also included. The final expression for the

$t\bar{t}$ probability is given by:

$$\boxed{P_{t\bar{t}}(x) = \sum_{comb\ \&\ \nu} \int d\rho_1 dm_1^2 dM_1^2 dm_2^2 dM_2^2\ |M|^2\ \frac{f(q_1)}{|q_1|}\frac{f(q_2)}{|q_2|}\ \Phi_6\ \prod_{i=1}^{4} \frac{1}{\sigma_i\sqrt{2\pi}} \exp\left[-\frac{(\rho_i - p_i^x)^2}{2\sigma_i^2}\right]} \tag{6.31}$$

The sum is over the 12 possible assignments of jets and quarks, and over the two neutrino solutions (consistent with energy and momentum conservation).

The integration over the mass variables in Eq.(6.31) is done using Gaussian integration with a Breit-Wigner kernel, and the integration over ρ_1 is performed using adaptive Gaussian integration.

Chapter 7

Performace of the Method in Simulated Experiments.

In this chapter, our procedure will be tested using an ensemble of experiments simulated with a Monte Carlo (MC) technique. In Section 7.1 and 7.2, we will describe the simulated event samples, and in Section 7.3 we will study the response of the method using ensemble tests.

7.1 MC Samples Defined in this Analysis.

For this analysis, the event selection will be base in the "precut" sample defined in the published DØ measurement of the mass of the top quark in single-lepton $t\bar{t}$

events. The selections for this sample are:

- jets: $\geq$4 jets, $E_T^{jets} > 15$ GeV and $|\eta^{jets}| < 2$
- leptons: $E_T^{lepton} > 20$ GeV, $|\eta^e| < 2$ and $|\eta^\mu| < 1.7$
- missing $E_T > 20$ GeV
- W selections: $E_T^W > 60$ GeV and $|\eta^W| < 2$

Because at this point our method can only deal with events with 4 jets, we have to restrict the sample further, and choose only those events that have exactly 4 jets. This extra selection criterion reduces our sample by an additional 30% relative to the precut sample. This is true for both signal and background, and means that the ratio of signal over background will remain approximately constant. The precut sample in the DØ data has 91 events, which gives 64 events with extacly 4 jets.

The previous analysis used events in the precut sample that had a $\chi^2 < 10$ for the kinematic fit to a $t\bar{t}$ hypothesis. This reduced the sample from 91 to 77 events. Because we do not use kinematic fitting, we do not need this selection criterion here.

Using Neural Network (NN) analysis, DØ found 29 good $t\bar{t}$ events in the sample of 77 events. The rest was supposedly background, composed of 80% W+jets, and

20% multi-jet production, which we will refer to as "QCD". According to this breakdown, we define the size of Sample 1 as follows:

$$\frac{91}{77} \times 0.70[29(S) + 48(B)] = 24(S) + 40(B) \tag{7.1}$$

$$40(B) = 32(W\text{+jets}) + 8(\text{multijets or "QCD"}) \tag{7.2}$$

The W selections in the "precut" sample were introduced for two reasons. The $|\eta_W| < 2.0$ selection was applied because outside of that region the agreeement between the W+jets simulation (VECBOS) and the W+jets data was very poor. The selection $E_T^W > 60$ GeV was used to reject the multijet background. The size of Sample 2 in this analysis is defined by loosening the W requirements, as follows:

- $\frac{24}{0.62} = 39$ (signal events)
- $\frac{32}{0.51} = 63$ (W+jets)
- $\frac{8}{0.22} = 36$ (QCD)

Where the denominators determining the number of events of each kind correspond to the effect of the W selections for each event-type, and the numerators are the numbers estimated for Sample 1 in Eq.(7.2).

7.2 Event simulation.

All the simulated event samples are the same as generated previously for use in the published measurement of the mass of the top quark by DØ [45], and are characterized below.

- Signal.

  The $t\bar{t}$ events were simulated using the Herwig event generator [51]. Samples were generated for top-quark masses of 140, 170, 175, 180 and 190 GeV. The events where then passed through the DØ detector simulation.

- W+jets background.

  The W+jets background was simulated using the VECBOS Monte Carlo event generator [52], and also processed through the DØ detector simulator.

- Multijet background.

  This background corresponds to QCD processes were one of the jets mimics an electron. There is no reliable(precise) QCD event generator, and for this reason data was used to characterize this background. QCD events without good electrons in the final state were selected from the data, and the electron identification criteria were loosened to provide false electrons. This defined a multijet sample, with one jet mimicking an electron, and this is what was used

for simulating background from multijet production.

7.3 Test of Linearity.

As a first step to test the performance of our method, we studied the dependence of the output (extracted) mass as a function of the input mass of the top quark ("linearity"). For this purpose, we used $t\bar{t}$ single-lepton events generated at different values of the mass of the top quark (m_t). Ignoring background, samples of 1000 events were analyzes using the likelihood method discussed in Chapter 6. For each sample, the most probable value of mass of the top quark was extracted by maximizing the likelihood.

Using the standard DØ corrections decribed in Section 4.3.1, the most probable value of the mass of the top quark was extracted for samples of 1000 $t\bar{t}$ events generated with masses for the top quark of 160, 175 and 190 GeV. The results are plotted as a function of the generated mass in Figure 7.1. A linear fit shows that the response does not have a slope of 1.0, which would be expected for the ideal case.

The same linearity test was also performed using the transfer functions described in Chapter 5, the results are ploted in Figure 7.2. Here, a linear fit shows that the reponse is consistent with a slope of 1.0.

Because we obtained a slope of unity using the transfer function, we conclude

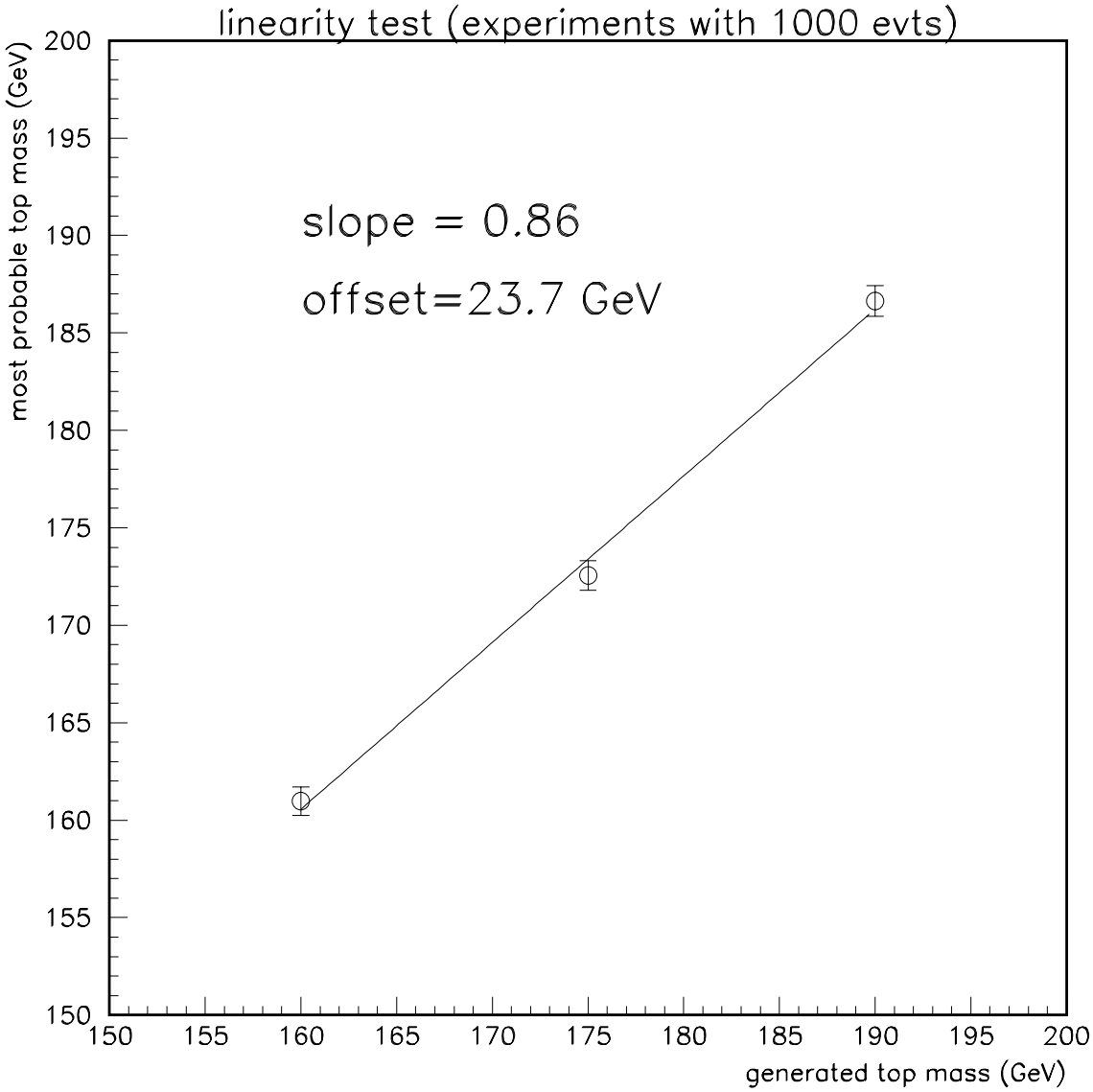

Figure 7.1: Most probable values of the mass of the top quark obtained for simulated experiments of 1000 events, generated with a m_t=160, 175 and 190 GeV. The standard DØ jet energy corrections were used in this study.

that the slope of 0.86 obtained in Figure 7.1 is a feature of the standard DØ energy corrections, and not of the method. This means that it is important not just to correct the mean value of the jet energy to obtain the correct mean for the parton energies (as done in the standard DØ corrections), but to consider the distribution of the difference in energies, as discussed in Chapter 5.

In what follows in this chapter, we will describe ensemble tests using the standard DØ corrections in Sections 7.4 and 7.6. In Section 7.6, an ensemble test will be performed using the tranfer functions.

7.4 Ensemble Tests with Sample 1.

To test the performance of the new method, experiments were simulated with 24 signal ($t\bar{t}$), 32 W+jets and 8 QCD events (according to Section 7.1). An equal number of electron and muon events were used for the signal and W+jets background. A mass of the top quark of 175 GeV was used to generate these experiments. (The muon events were treated as if they had the resolution of the electron samples.)

For each experiment, the events were combined in one likelihood function, and the most probable value of the mass of the top quark obtained maximizing the likelihood as described in Chapter 6. Examples of likelihood functions for four such experiments are shown in Figure 7.3.

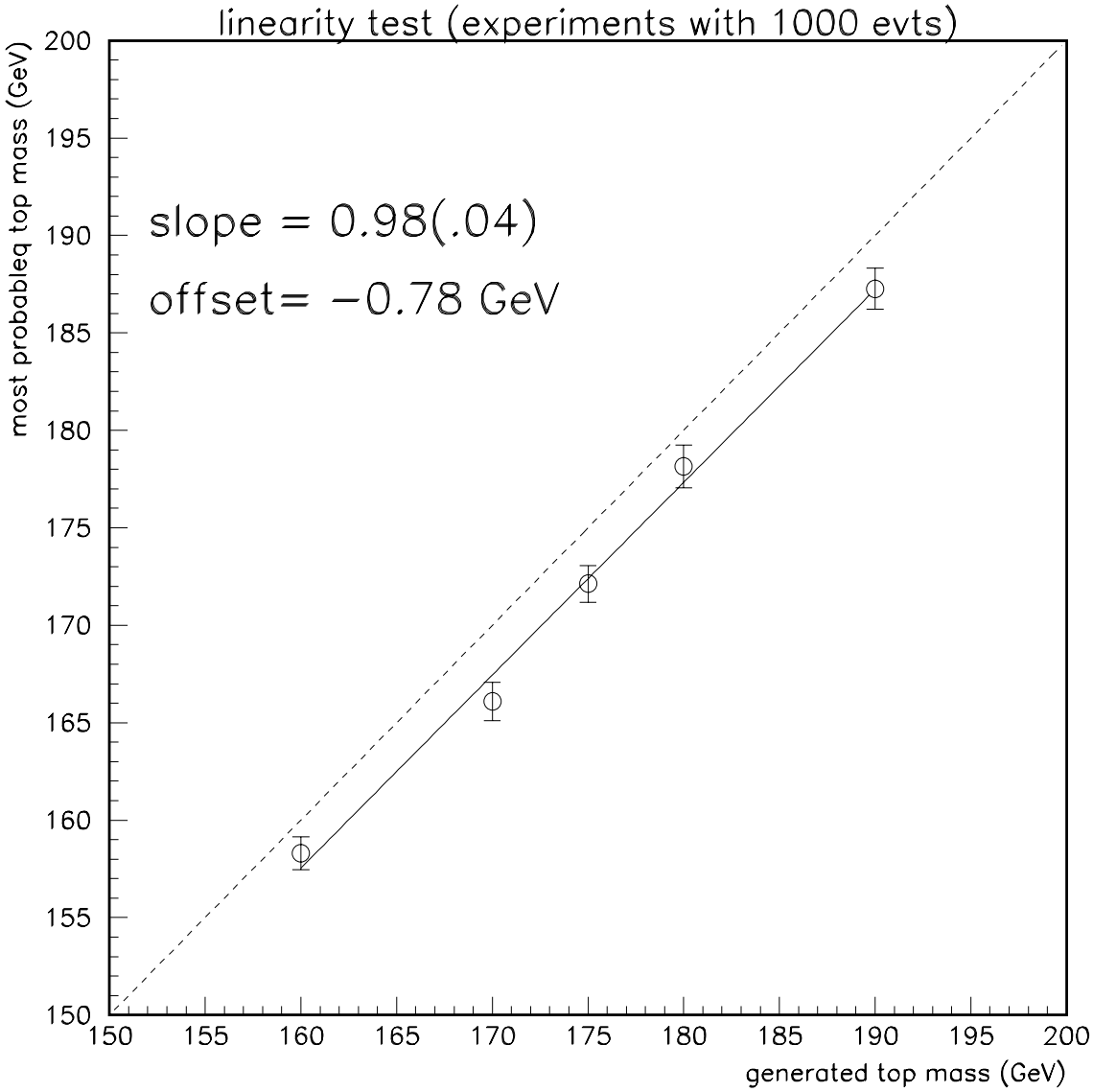

Figure 7.2: Most probable values of the mass of the top quark obtained for simulated experiments of 1000 events, generated with a m_t=160, 170, 175, 180 and 190 GeV. The complete transfer functions were used in this study.

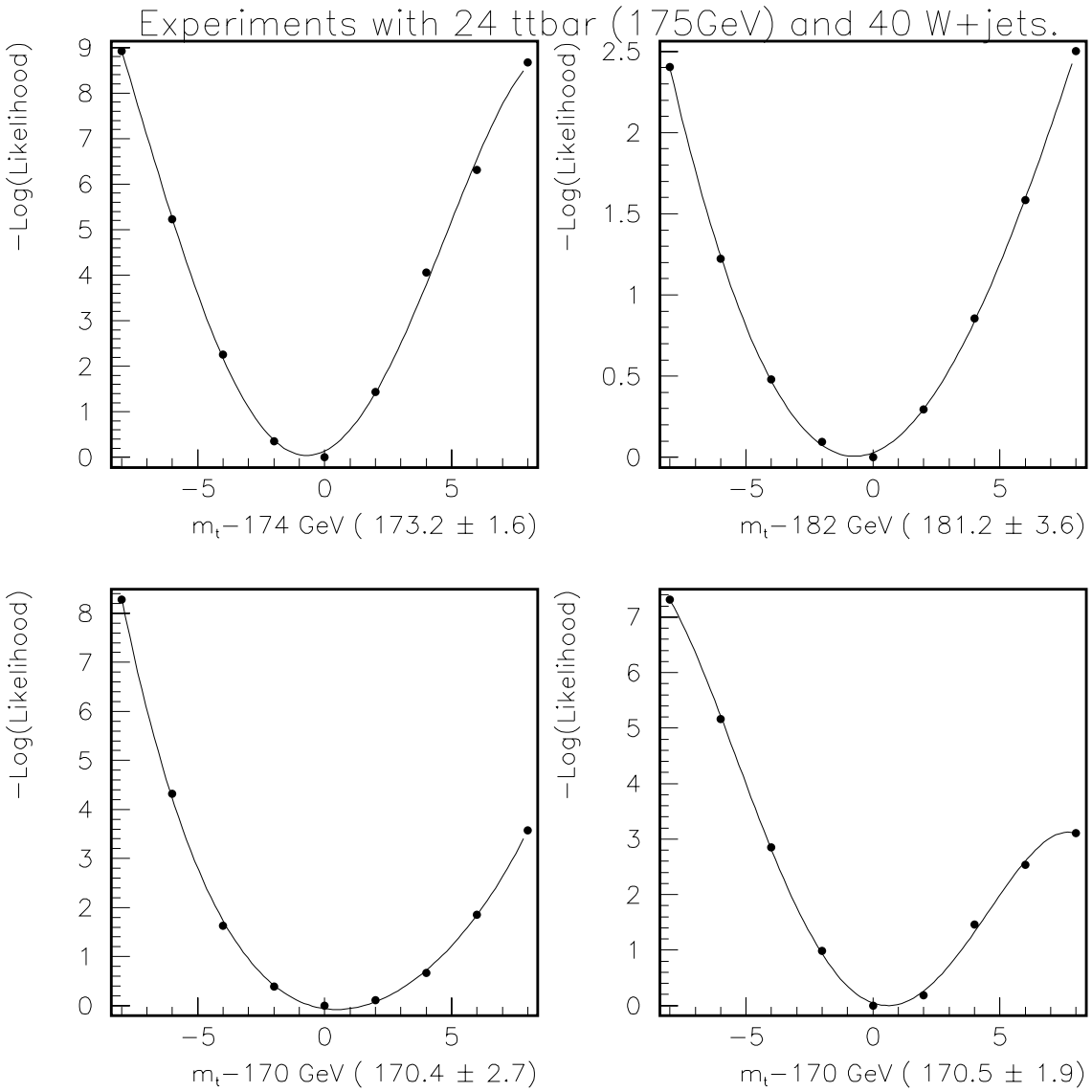

Figure 7.3: -ln(Likelihood) for 4 Monte Carlo experiments with 24 signal events and 40 background events, all generated at $M_t = 175$ GeV. The numbers in parentheses indicate the most probable value of the mass of the top quark for each experiment. The x-axis on the plots has been offset to give the minimum always around $x = 0$ and a constant was subtracted to the likelihood function for convenience.

The distribution of the most probable mass for each experiment is shown in Figure 7.4. For each experiment, an estimation of the uncertainty in the extracted mass is obtained from the width of the likelihood function (one standard deviation on the mass corresponding to a 0.5 change in the logarithm of the likelihood). Using this estimation, the significance of the difference between the most probable mass in each experiment and the generated (input) top-quark mass can be calculated, the distribution in this "pull" parameter is also shown in Figure 7.4. The distribution in the uncentainties for each experiment is shown in Figure 7.5.

The width of the distribution in Figure 7.4 represents the expected statistical uncertainty that this analysis technique will provide when used to extract the mass of the top quark in DØ Run I data. The RMS of 5.3 GeV, divided by the slope of the response curve $5.3/0.86 = 6.5$ GeV, should be compared with 8.0 GeV, obtained in the corresponding ensemble test for the Neural-Network analysis published by DØ. This result suggests that, compared to the previous analysis of the same data, there is a significant reduction expected in the statistical uncertainty on the extracted mass, compared to the previous analysis of the same data.

The fact that the pull distribution in Figure 7.4 gives an RMS consistent with 1.0, means that our estimations of the widths of the likelihoods for single events are reasonable. Several aproximations have been made in our likelihood calculation (e.g., perfect measurement of jet angles, perfect measurement of energies of electrons

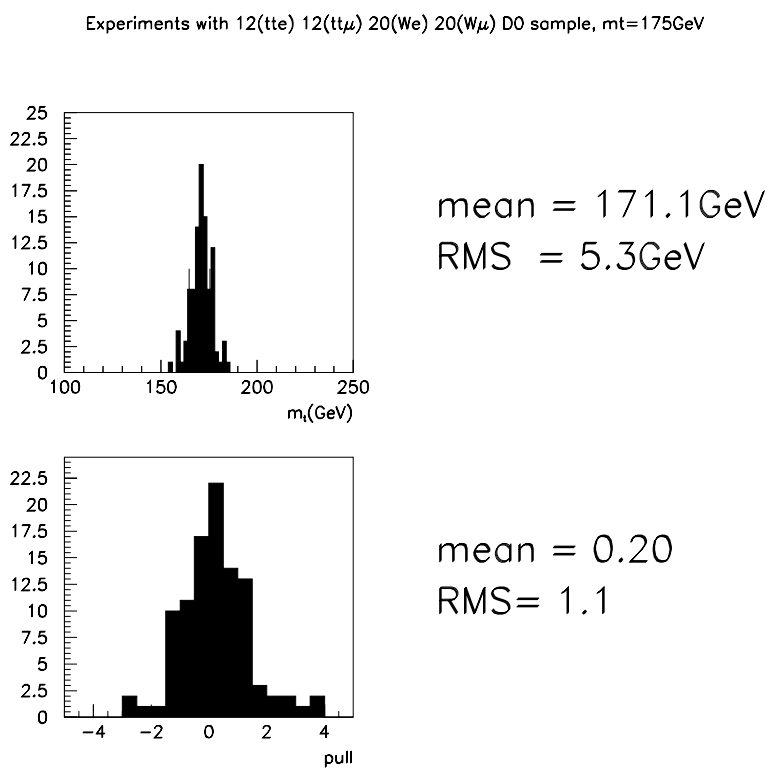

Figure 7.4: Esemble tests with Sample 1. The upper plot shows the results for the most probable mass extracted in different MC experiments, and lower plot shows the pull distribution in the mass.

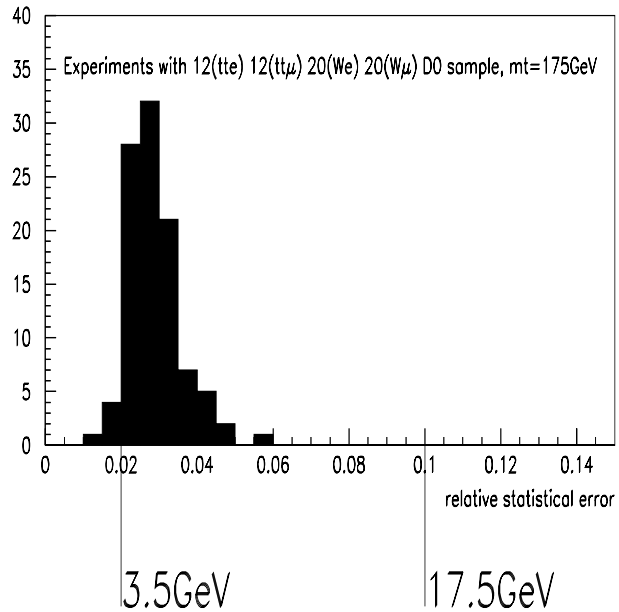

Figure 7.5: Esemble test with Sample 1. The displayed statistical uncertainty is obtained from the width of the likelihood for each experiment.

and muons), and our preliminary results suggest that these are also approximately valid.

7.5 Ensemble Tests with Sample 2.

Sample 2, defined in Section 7.1, has similar selection criteria as Sample 1, but without the extra W requirements. This gives an expected number of 40 signal, 63 W+jets, and 61 multijet events for each experiment. Another series of ensemble tests was performed assuming these statistics.

The distribution in the most probable masses for experiments using Sample 2

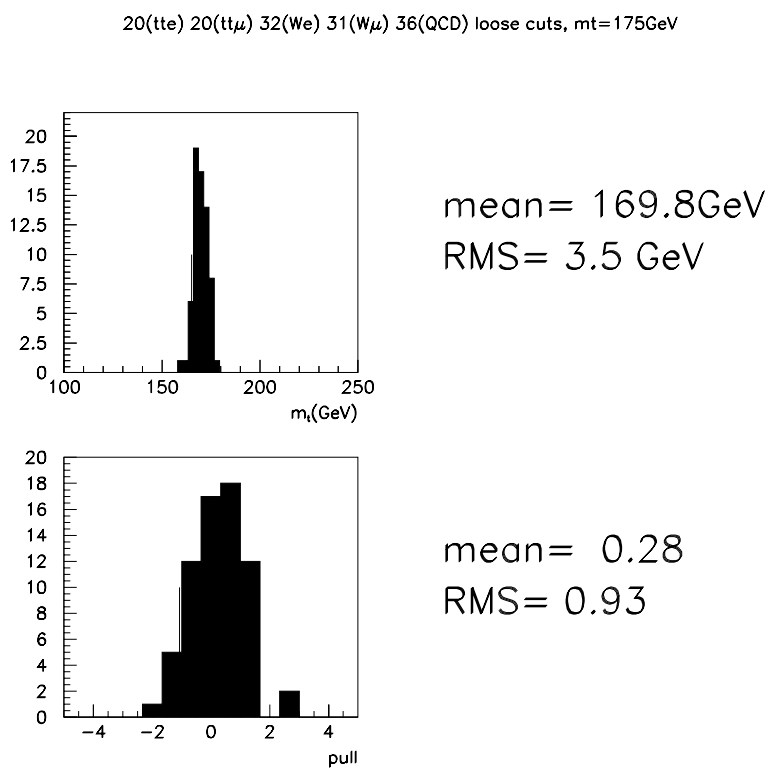

Figure 7.6: Esemble test with Sample 2. The upper plot shows the results of the most probable mass obtained in different experiments, and the lower plot shows its pull distribution.

is shown in Figure 7.6, together with the pull distribution in the extracted mass. The distribution in the statistical uncertainty for each experiment is displayed in Figure 7.7. The width of the distribution in the most probable masses is 3.6 GeV. This should be compared to 5.6 GeV obtained for Sample 1. This improvement suggests that the additional selections on the W should be studied further to judge the possibility of loosening them. This is problematic because the the W+jets background would have to be understood in a region were the VECBOS simulation does not reproduce the W+jets data very well, as discussed in Ref. [45]. In addition, the impact of the multijet background, for which there is no precise simulation, will also have to be studied in greater detail.

7.6 Esemble Tests with Sample 1 and Transfer Functions.

Thus far, all the sets of simulated experiments used the standard DØ corrections. As indicated before, these corrections have the deficiency that they provide a response slope on 0.86, which can be improved when using the transfer functions of our method.

A set of simulated experiments of Sample 1 were analyzed as before, using the

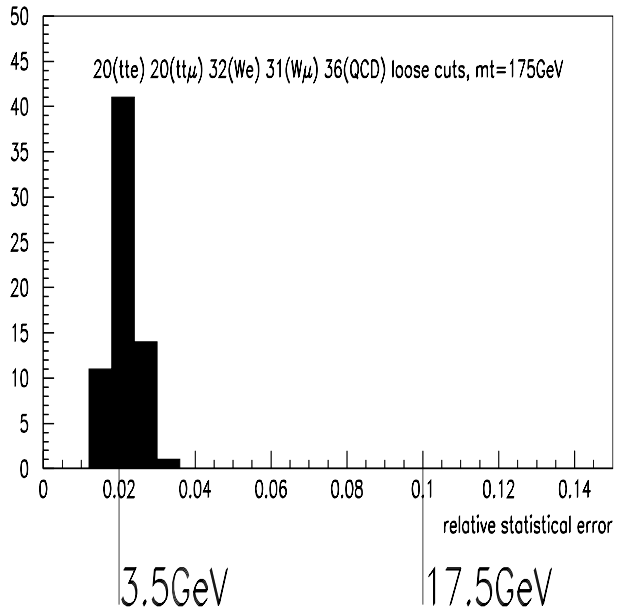

Figure 7.7: Esemble test with Sample 2. The displayed statistical error is obtained from the width of the likelihood for each experiment.

same method, but now with the transfer functions intead of the DØ energy corrections. The distribution for the most probable mass of the top quark in each experiment is shown in Figure 7.8. The width of this distribution is 5.0 GeV, and because the response slope is 1.0, there is no correction required to this width, and it can be compared directly with the 8.0 GeV obtained in the published analysis.

Using the transfer function to account for the energy smearing of the partons in the hadronization process, therefore offers an improvement in the result, reducing significantly the expected statistical uncertainty on the mass of the top quark in Run I data. However, these transfer functions were derived using simulated events,

and a study is therefore required to determine if the procedure is consistent with the observations in the data. This will be checked in the near future on samples of γ+jet and Z+jets events.

7.7 Measurement of the Mass of the W boson.

Once the probability is calculated, the likelihood can be expressed as a function of any parameter in the differential cross section. Thus far, we have considered the likelihood only as a function of the mass of the top quark, with all other parameters fixed to their expected values. In this section the likelihood will be maximized as a function of the mass of the W boson (M_W), in order to check the output value of M_W.

We will concentrate on the hadronic decay, which will reflect the validity of our jet energy corrections. An example of the likelihood as a funtion of M_W in the hadronic channel is shown in Figure 7.9 for a sample of 40 $t\bar{t}$ MC events. A total of 1000 Monte Carlo experiments, each with 24 $t\bar{t}$ events, were generated to determine the mass of the W boson in the hadronic branch of the top decay, and the results for a fixed value of $M_t = 175$ GeV are shown in Figure 7.10. Although a detailed study of the power of the method to confirm M_W still remains to be demonstrated, the example shows excellent potential for performing an internal check of jets energies

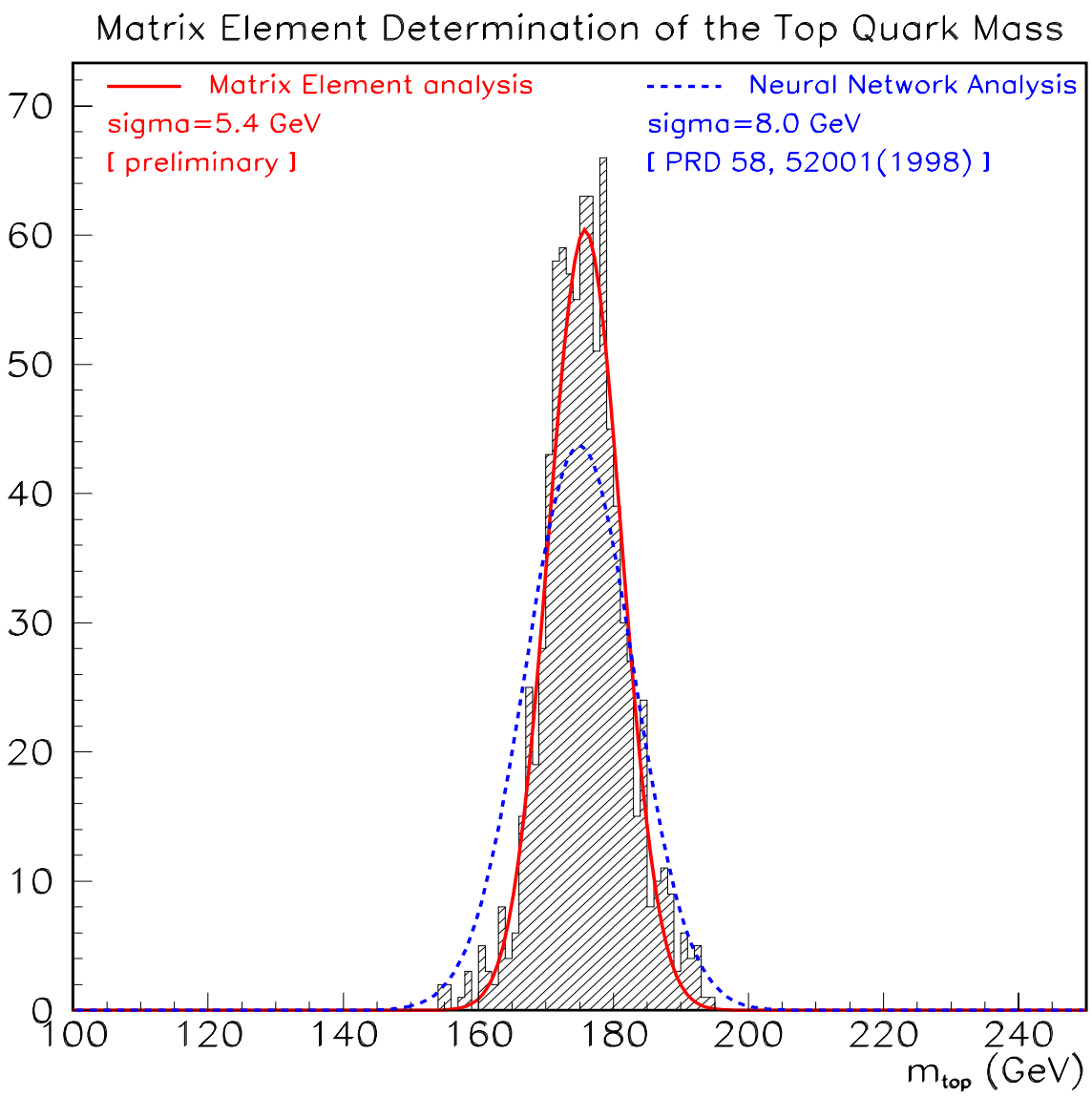

Figure 7.8: Esemble tests with Sample 1 using the transfer functions to account for the hadronization process. The hatched histogram is the distribution of most probable masses for each experiment, the Gaussian curve fitted to this distribution has a σ=5.5 GeV and is also shown here. The other Gaussian in the plot, with σ=8.0 GeV and the same total area, corresponds to the results obtained in the previous analysis by DØ [45] and is here only to compare the result of this test with those of an equivalent test done for the Neural Network analysis.

in the measurent of $t\bar{t}$ events.

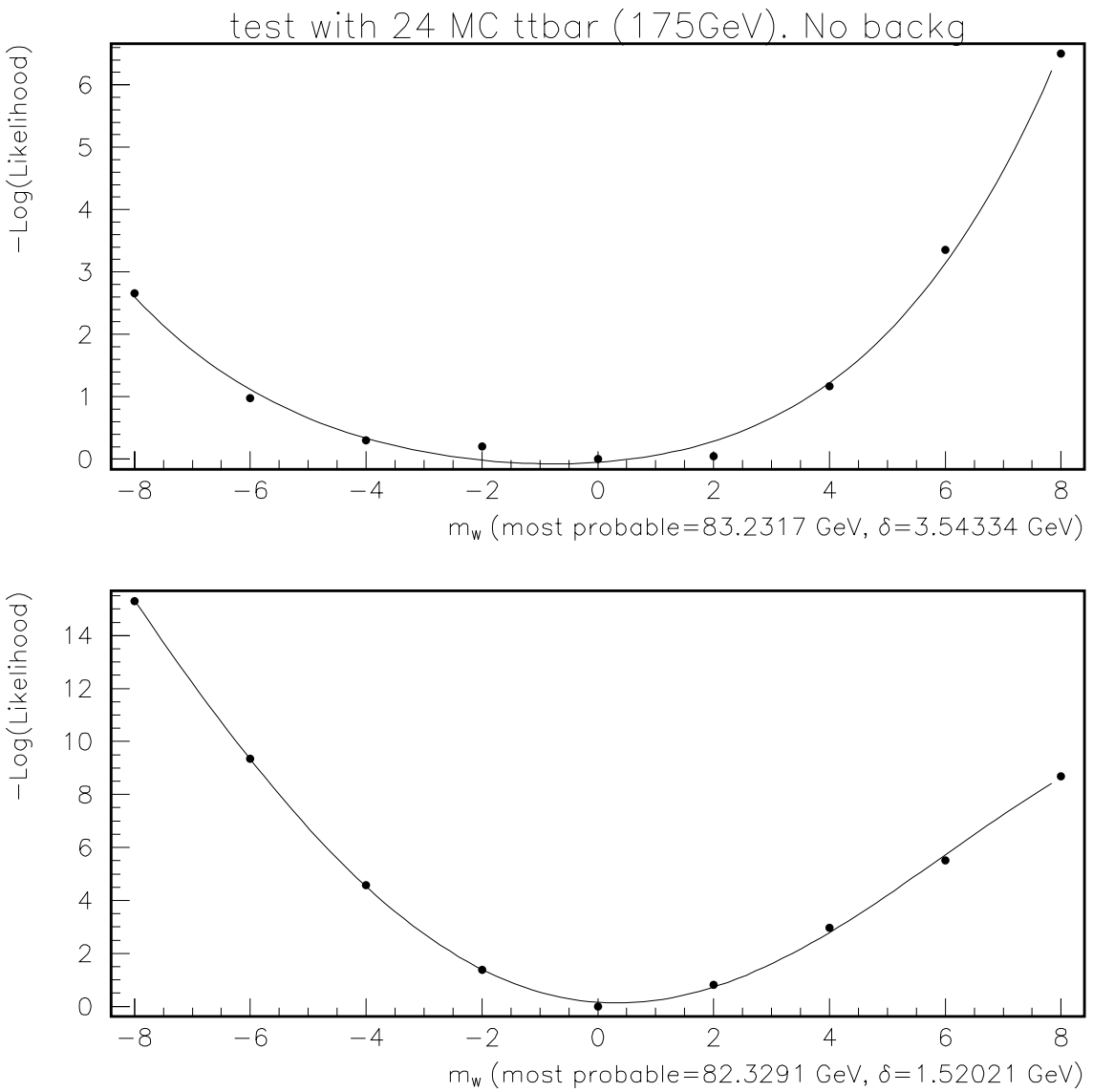

Figure 7.9: Two examples of likelihood as a function of the mass of the W boson in the hadronic channel for a sample of 24 signal $t\bar{t}$ events with no background.

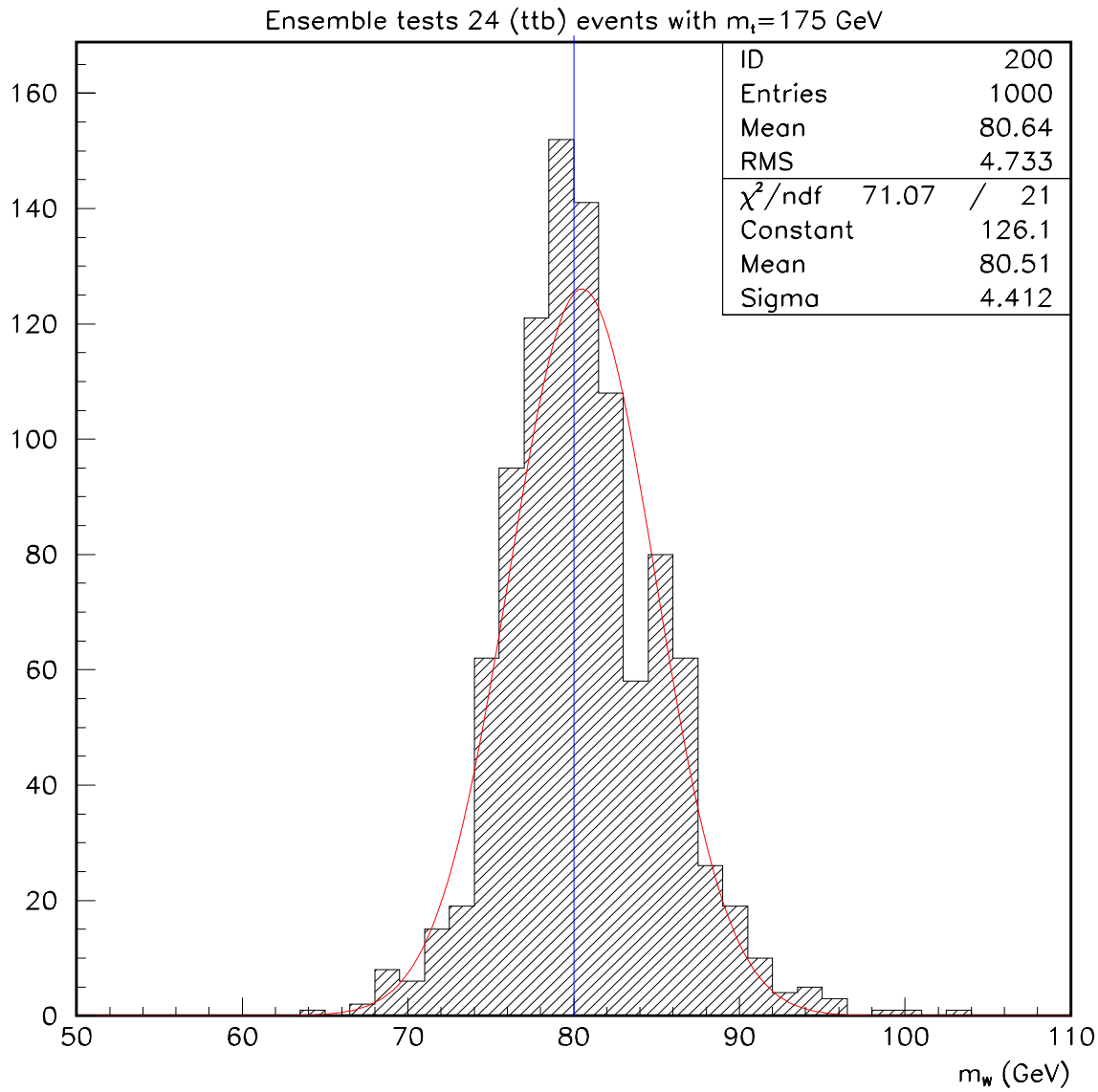

Figure 7.10: Ensemble tests for the determination of the mass of the W boson in the hadronic branch of the $t\bar{t}$ event. Each experiment is simulated using 24 signal $t\bar{t}$ events and no background, with $M_t = 175$ GeV.

Chapter 8

Conclusions

In this dissertation we have described a new technique developed to obtain the mass of the top quark (m_t) in $t\bar{t}$ events, in which one of the top (t) quarks decays into a lepton (either an electron or a muon), a jet from a b quark and a neutrino, and the other t decays into three jets (one from a b quark and two from the decay of the W into light quarks). The technique has been demonstrated to work very well with Monte Carlo events (in Chapter 7).

There is still much to be done in several areas in order to gain a better understanding of the effect of the background on the mass response of the analysis (see Section 7.3), the impact of the changes in jet energy scale in the data when using the transfer functions (see Chapter 5), and the nature of the systematic uncertainties (not discussed in this thesis). Nevertheless, there is good evidence that this method

can yield a more precise measurement of the mass of the top quark with the existent DØ data collected during Run I at the Tevatron.

Our technique also has potential for checking the mass of the W boson (m_W) in the hadronic decay modes of the W in $t\bar{t}$ events. A detailed study of this issue is yet to be performed, but the evidence in Section 7.7 suggests that a measurement is feasible with the existing data. This would improve the understanding of the jet energy scale and, in that way, reduce the current systematic uncertainty in the measurement of the mass of the top quark.

In order to avoid bias, it was decided not to use the $t\bar{t}$ data from DØ to tune the new analysis. As discussed in Chapter 7, all studies were performed with Monte Carlo simulated experiments. Nevertheless, when we first presented these studies to the DØ collaboration, we processed the $t\bar{t}$ data through the preliminary analysis package, to check that results from the MC were consistent with those from data. This was done using the standard DØ jet energy corrections, and the results are shown in Figure 8.1. The first two plots, in the upper part of the figure, show the likelihood as a function of m_t and m_W for a set of 46 electron+4 jets events in the DØ sample. The quoted uncertainties correspond to changes of 0.5 in the logarithm of the likelihood functions. The lower part of Figure 8.1, has the same analysis, but now also including 41 events with muon + 4 jets. (As mentioned in Chapter 6, the resolution in the muon momentum measurement has not yet been taken into

proper account.) These results should not be regarded as DØ's measurement of m_t and m_W, but only as an indication that the data behave in a way similar to MC simulations. (The statistical uncertainty reported by DØ for the currently accepted and published analysis of lepton + jets events is $\delta_{m_t} = 5.6$ GeV.)

Other measurements at DØ can also be improved with this technique. In particular, a measurement of the W helicity in $t\bar{t}$ events can be performed if the likelihood is maximized for the value of the helicity parameter instead of m_t, and DØ is already pursuing this possibility [50].

In this thesis, we have proposed a method for extracting the mass of the top quark using all the measured variables in $t\bar{t}$ events. We consider this the most efficient way to extract such information and to separate signal from background in an interesting group of events immersed in a larger sample of background. The technique should be considered in approaching similar problems of this kind. In particular, searches for the Higgs boson in Run II at the Tevatron should provide an interesting opportunity to apply this method.

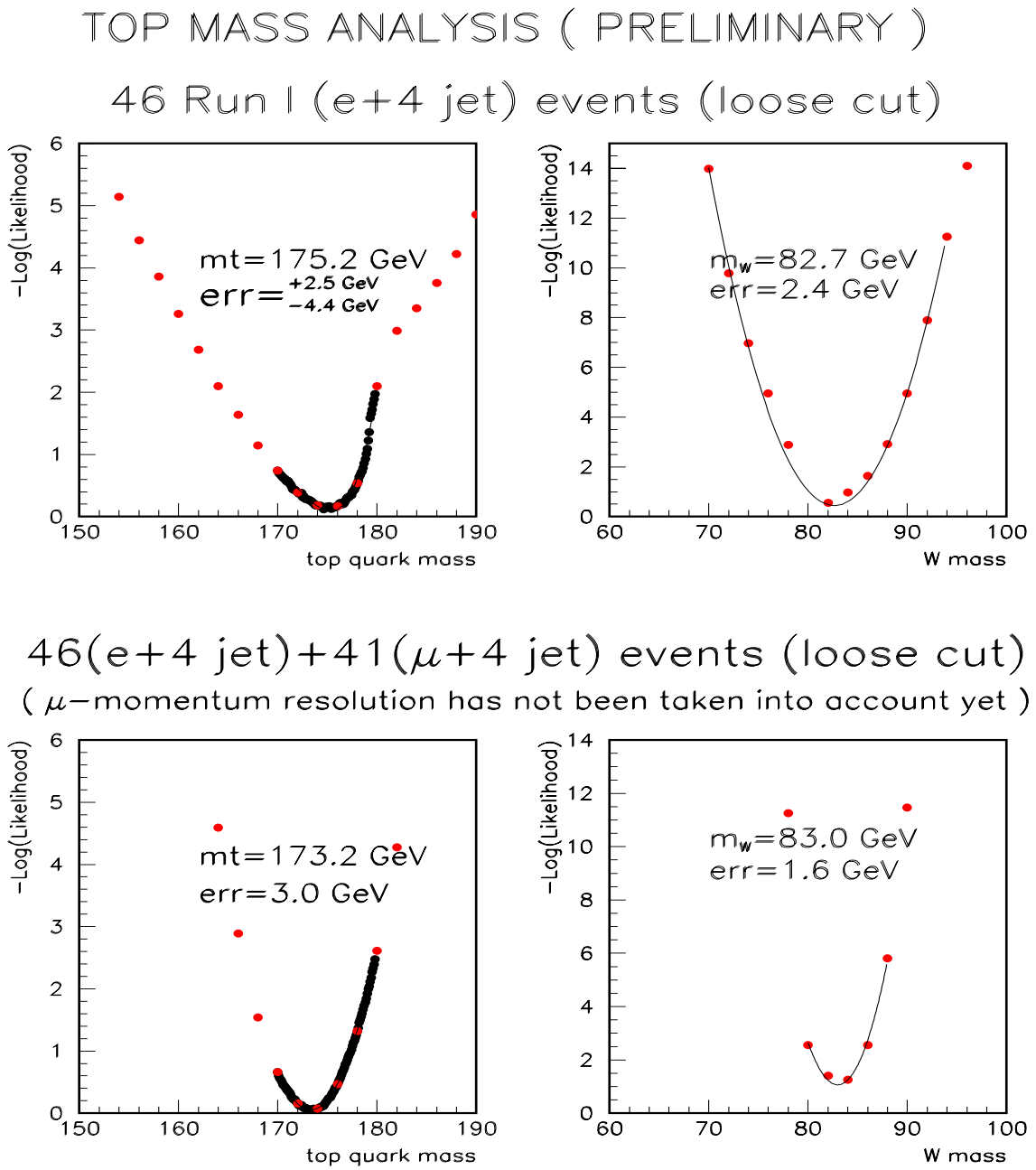

Figure 8.1: Top left(right): Likelihood as a function of $m_t(m_W)$ for 46 e + 4 jets events in the DØ Run I data. Bottom left(right): Likelihood as a function of $m_t(m_W)$ for 46 e+4 jets and 41 muon+4 jets events in DØ Run I data.

Appendix A

Understanding the improvement in the calculation of the top-quark mass using the full matrix element

A.1 Introduction

The method presented in this thesis suggests that an improvement in the measurement of the mass of the top quark can be realized relative to previous methods. Such an improvement raises the natural question as to which feature of the new technique is primarily responsible for the difference? This is the question we address in this Appendix [53].

A.2 The model.

A simple example was developed to understand the exact origin of the statistical improvement. This model consists of simulated events, in which each measurement is characterized by a Gaussian probability distribution.

Associated each event i there is a probability distribution for the variable x defined by two paramenters, the width σ_i and a mean x_i. The width σ_i is generated randomly with a Gaussian probability with mean $< \sigma_i >= a$ and a standard deviation $\delta_{\sigma_i} = b$. Once σ_i is determined for an event, the mean of the probability distribution for that event is selected randomly with another Gaussian distribution with mean $< x_i >= 1$ and width σ_i. In this way, a probability distribution for the variable x in the event i is constructed

$$P_i(x) = \frac{1}{\sqrt{2\pi}\sigma_i} \exp \frac{-(x - x_i)^2}{2\sigma_i^2} \quad , \tag{A.1}$$

with each event normalized to unit area.

A.3 Two possible paths for the analysis.

Two different ways to estimate the mean value $< x >$ of the one dimensional distribution of x_i will be studied, using samples of 30 events, that is, $i = 1, 2, 3, ..., 30$

.

Method I defines x_i as the most probable value of x given by the maximum of $P_i(x)$ defined in Eq. A.1. The estimator $\mathcal{X}_I$ of $< x >$ becomes simply the average of all the x_i in the sample of events:

$$\mathcal{X}_I = \frac{1}{30}\sum_{i=1}^{30} x_i \quad . \tag{A.2}$$

Method II uses not only the x_i, but also the width of the distribution. All the probabilities for a sample of events are multiplied together giving a probability for the whole sample

$$\mathcal{L}(x) = \prod_{i=1}^{N} P_i(x) \quad . \tag{A.3}$$

The value $\mathcal{X}_{II}$, where the probability reaches its maximum ($\mathcal{L}(\mathcal{X}_{II}) = \mathcal{L}_{max}$), is then the estimator of $< x >$.

Although the procedure would be correct for any resolution function, when $P_i(x)$ is Gaussian, this method is equivalent (and agrees with) the simpler prescription of weighting:

$$< x >= \frac{\sum x_i(\frac{1}{\sigma_i^2})}{\sum(\frac{1}{\sigma_i^2})} \tag{A.4}$$

A.4 The result.

As we mentioned, the tests of this simple model are always performed considering samples of 30 events. Each of these samples is called an experiment, and an estimator of $< x >$ is obtained for each experiment, with both methods described in Section A.3. The dispersion in the results of a set of experiments provides a measure of the uncertainty of a single experiment.

The first test is performed assuming that all the events have the same width of $\sigma_i = 0.2$, for $i = 1, 2, 3, ..., 30$. The results are shown in Fig. A.4. As expected, there is no difference at this point between the results for the two techniques.

The next, and more interesting, test is performed for events with different uncertainties. For each event, a mean x_i value and its uncertainty are determined as explained in Section A.2, assuming $a = 0.2$ and $b = 0.1$. The result for the two methods are shown in Fig. A.4. A clear reduction in the dispersion is achieved when Method II is used instead of Method I.

A.5 Conclusion.

Method I treats every event in a way similar to that in Ref.[45], where a fitted mass was obtained for each event, and the information on the uncertainty for each particular event was ignored.

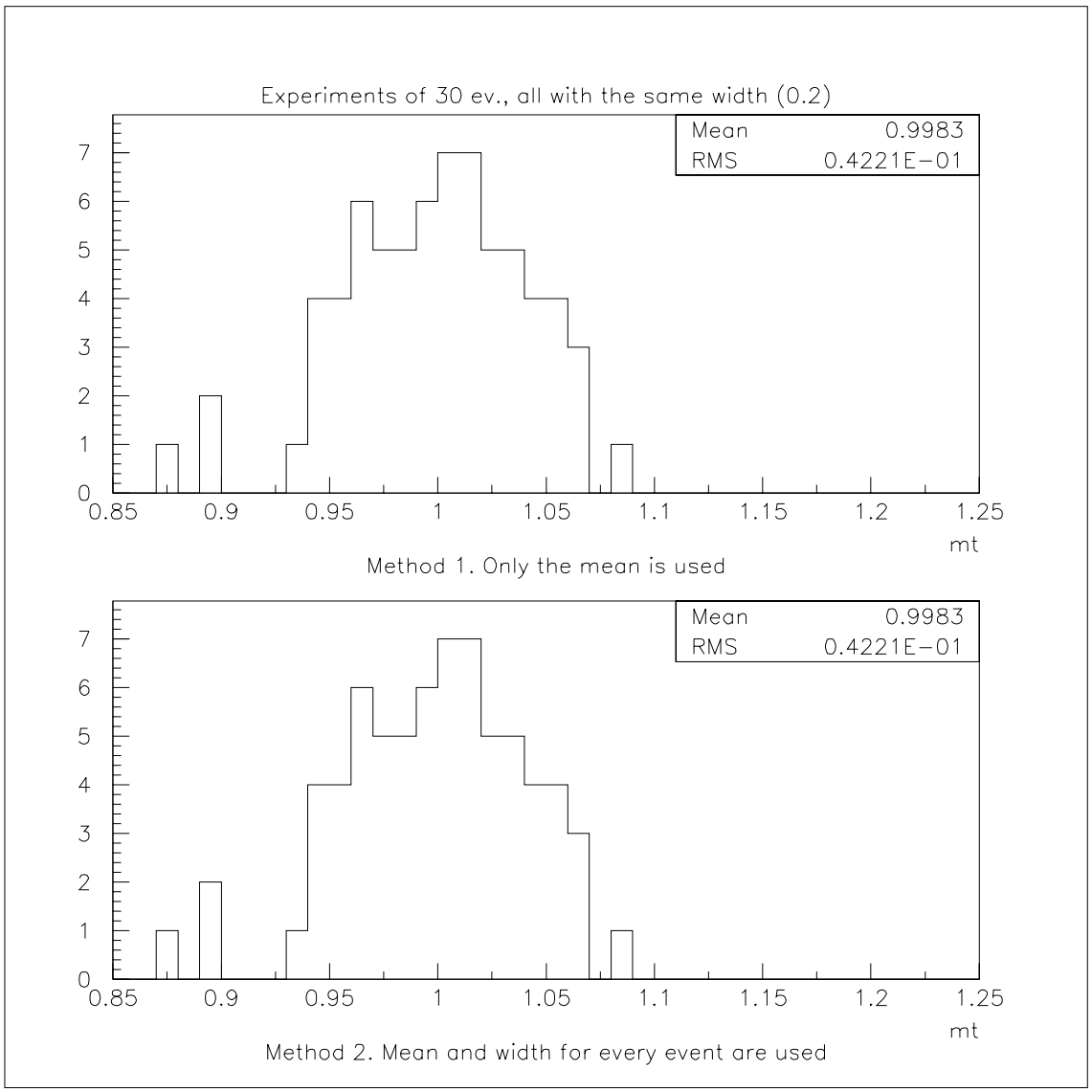

Figure A.1: Histrograms of estimators of $< x >$ obtained from 80 samples of 30 events using Method I (top) and Method II (bottom). All events have the same width for their probability distributions. As expected, the plots show no difference between these two procedures.

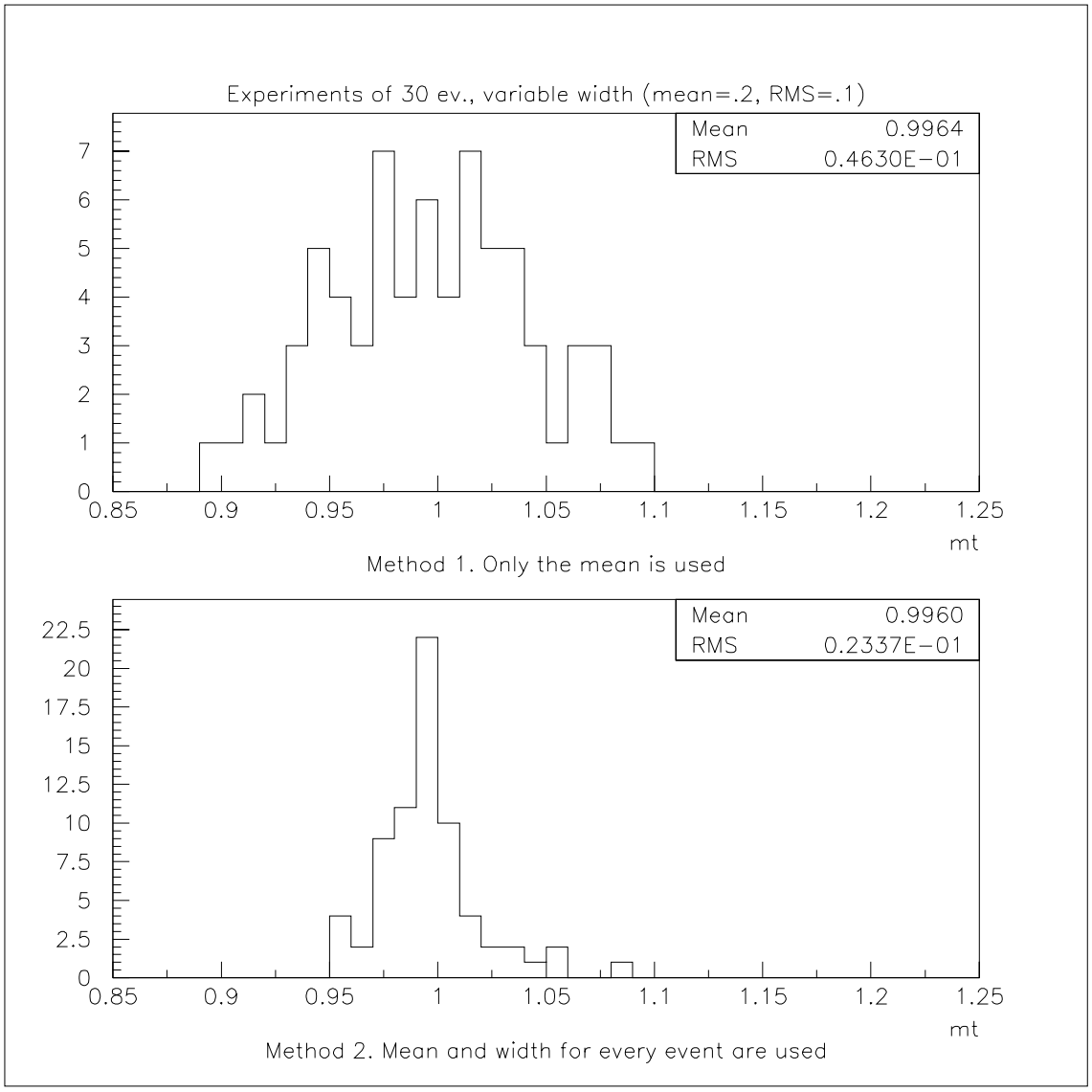

Figure A.2: Histrograms of estimators of $< x >$ obtained from 80 samples of 30 events using Method I (top) and Method II (bottom). The input events have large differences in uncertainties.

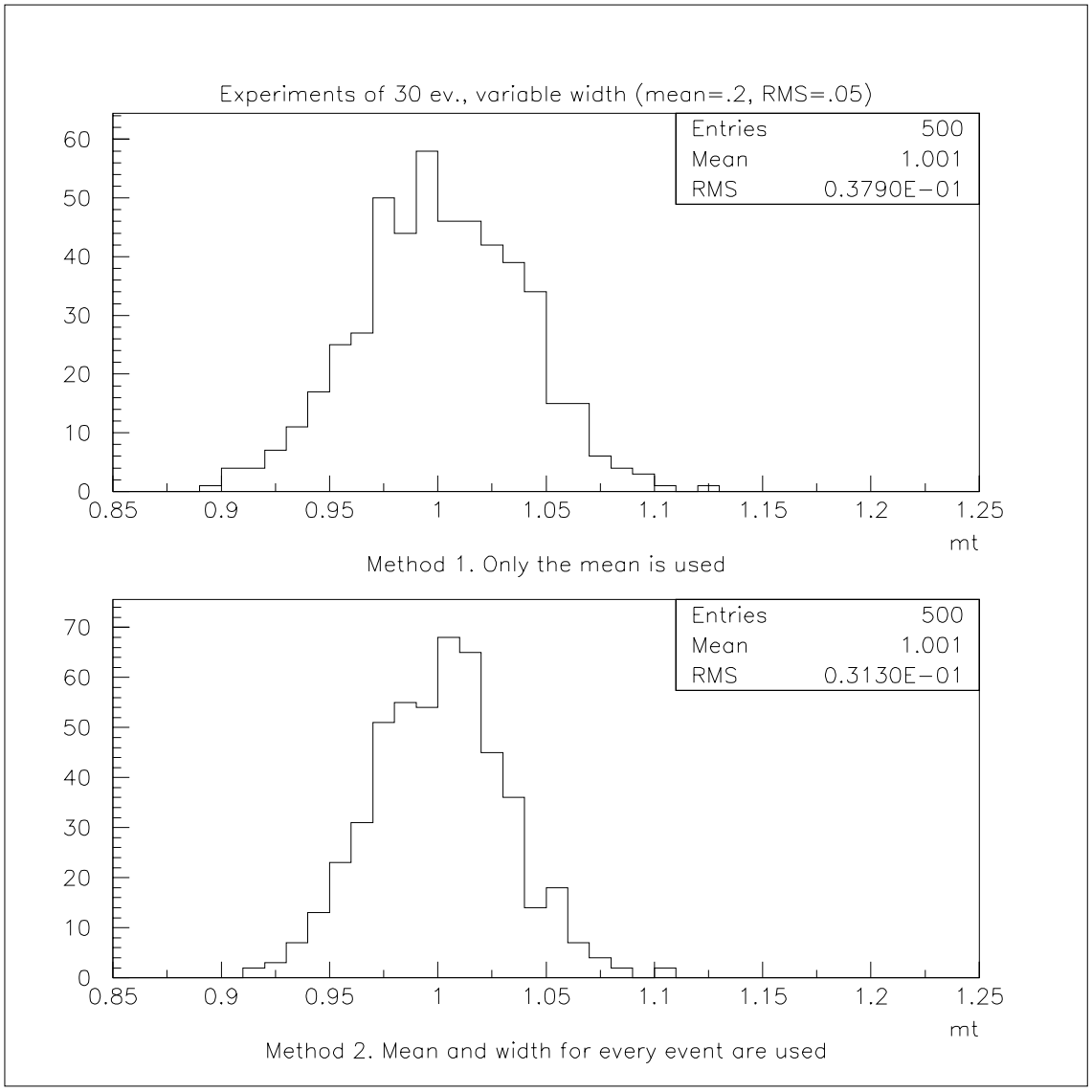

Figure A.3: Histrograms of estimators of $< x >$ obtained from 80 samples of 30 events using Method I (top) and Method II (bottom). The input events have small differences in uncertainties.

Method II, on the other hand, is similar to the analysis technique in this thesis. A probability is obtained as a function of the mass of the top quark for each event, and the probability functions for all the events in the sample are then combined, as in Eq. A.3.

A clear difference in the dispersion follows from the effective weighting by the uncertainty of the measurement. This additional information implemented in the analysis in this dissertation is the likely reason for the improvement over Ref. [45].

Thus, the difference resulting between the two analyses in this simple example is totally consistent with the fact that in a sample of measurements of a random variable, where each measurement has a different uncertainty, the optimal estimator of the mean is not a simple average, but rather a weighted one.

For the case of $t\bar{t}$ events, different configurations can have different measurement errors, and yield probability distributions that are often not even symmetric. The calculation of a probability as a function of the mass of the top quark for individual events is one way to take this difference into proper account.

We have not specified to what extent the uncertainty on the mass varies for the $t\bar{t}$ events observed by DØ and used in the analysis of Ref. [45]. Clearly, if the variation in the uncertainty is small, then the difference between the two techniques is less important. To ilustrate this point another test was done, identical to the one in Fig. A.4, but now taking b=0.05. The results are shown in Fig. A.4.

Appendix B

Phase Space Calculation for Single Lepton $t\bar{t}$ Events

For $q_1 q_2 \to t\bar{t}$ events like the one in Fig.B.1 the Lorentz invariant phase space (see Ref. [21]) is characterized by the particles momentum ($\overrightarrow{p}_{q's}$, $\overrightarrow{p}_e$, $\overrightarrow{p}_\nu$).

$$d\Phi_6(q_1+q_2;p_1,p_2,p_3,p_4,p_e,p_\nu) = \delta^4(q_1+q_2-\sum_{i=1}^{6} p_i)\prod_{i=1}^{6}\frac{d^3\overrightarrow{p}_i}{(2\pi)^3 2E_i} \quad . \qquad \text{(B.1)}$$

As was discussed in subsection 6.4.3 to integrate the probability it is very convinient to change variables from the particles momentum to ($\overrightarrow{\Omega}_{jets}, \rho_1, M_1, m_1, M_2, m_2, \overrightarrow{p}_e$), where $\overrightarrow{\Omega}_{jets}$ is the jet's solid angle, $\rho_i = |\overrightarrow{p}_{jet_i}|$ is the module of the momentum of the i-th jet, and (M, m) are the top and W masses.

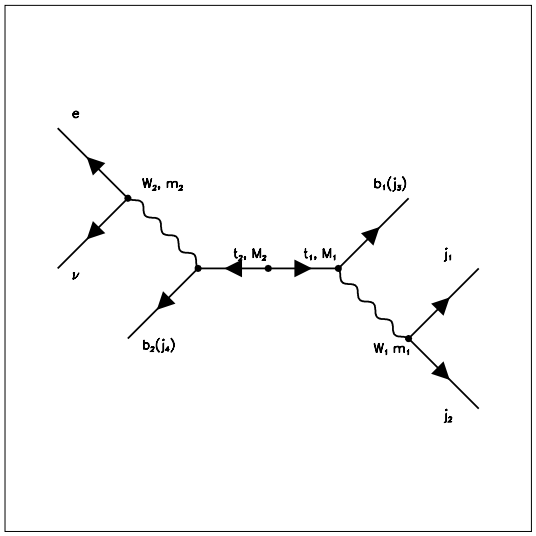

Figure B.1: Feymann diagram for the single-lepton $t\overline{t}$ event.

One way to perform the transformation of variables is by calculating the Jacobian of the transformation. A simpler way is to use the recursive character of the phase space as described in Ref. [21] . The idea is to 1) group particles into a composite particle, 2) introduce a mass delta for the composite particle, and 3) integrate the delta over the variables of individual particles. The all hadronic branch gives

$$\begin{aligned}\prod_{i=1}^{3}\frac{d^3\overrightarrow{p}_i}{(2\pi)^3 2E_i} &= \delta(p_{W_1}^2 - m_1^2)dm_1^2\ \delta(p_{t_1}^2 - M_1^2)dM_1^2\ \prod_{i=1}^{3}\frac{d^3\overrightarrow{p}_i}{(2\pi)^3 2E_i} \\ &= \frac{dm_1^2\ dM_1^2\ d\rho_1}{\left|\frac{\partial p_{W_1}^2}{\partial \rho_2}\right|\ \left|\frac{\partial p_{t_1}^2}{\partial \rho_3}\right|}\ \prod_{i=1}^{3}\frac{\rho_i^2 d\Omega_i}{(2\pi)^3 2E_i}\end{aligned} \tag{B.2}$$

in the last step the deltas were integrated with respect to ρ_2 and ρ_3 using the

relation:

$$\int f(x)\delta[g(x)]dx = \frac{f(a)}{|g'(a)|} \quad \text{, with} \quad g(a) = 0 \quad . \tag{B.3}$$

The value of the partial derivatives is

$$\begin{aligned}
\frac{\partial p_{W_1}^2}{\partial \rho_2} &= \frac{\partial (p_1 + p_2)^2}{\partial \rho_2} \\
&= \frac{\partial}{\partial \rho_2}(m_1^2 + m_2^2 + 2E_1E_2 - 2\rho_1\rho_2 cos\theta_{12}) \\
&= 2E_1\frac{\rho_2}{E_2} - 2\rho_1 cos\theta_{12}
\end{aligned} \tag{B.4}$$

and

$$\begin{aligned}
\frac{\partial p_{t_1}^2}{\partial \rho_3} &= \frac{\partial (p_1 + p_2 + p_3)^2}{\partial \rho_3} \\
&= \frac{\partial}{\partial \rho_3}(m_1^2 + m_2^2 + m_3^2 + 2\,p_1 \cdot p_2 + 2E_1E_3 - 2\rho_1\rho_3 cos\theta_{13} + 2E_2E_3 - 2\rho_2\rho_3 cos\theta_{23}) \\
&= 2E_1\frac{\rho_3}{E_3} - 2\rho_1 cos\theta_{13} + 2E_2\frac{\rho_3}{E_3} - 2\rho_2 cos\theta_{23} \quad .
\end{aligned} \tag{B.5}$$

For the lepton branch the integration of the deltas is done over ρ_4 and the

neutrinos longitudinal momentum p_ν^z. The derivatives are

$$\begin{aligned}\frac{\partial p_{W_2}^2}{\partial p_\nu^z} &= \frac{\partial (p_e + p_\nu)^2}{\partial p_\nu^z} \\ &= \frac{\partial}{\partial p_\nu^z}(m_e^2 + m_\nu^2 + 2E_e E_\nu - 2p_e^z p_\nu^z - 2\overrightarrow{p}_e^t \cdot \overrightarrow{p}_\nu^t) \\ &= 2E_e \frac{p_\nu^z}{E_\nu} - 2p_e^z\end{aligned} \tag{B.6}$$

and

$$\begin{aligned}\frac{\partial p_{t_2}^2}{\partial \rho_4} &= \frac{\partial (p_e + p_\nu + p_4)^2}{\partial \rho_4} \\ &= \frac{\partial}{\partial \rho_4}(m_e^2 + m_\nu^2 + m_4^2 + 2\, p_e \cdot p_\nu + 2E_e E_4 - 2\rho_e \rho_4 cos\theta_{e4} + 2E_\nu E_4 - 2\rho_\nu \rho_4 cos\theta_{\nu 4}) \\ &= 2E_e \frac{\rho_4}{E_4} - 2\rho_e cos\theta_{e4} + 2E_\nu \frac{\rho_4}{E_4} - 2\rho_\nu cos\theta_{\nu 4} \quad .\end{aligned} \tag{B.7}$$

Finally two of the deltas in Eq.B.1 are integrated with repect to the neutrinos transverse momentum giving a value of one. The other two deltas will be integrated later with respect to the initial parton's logitudinal momentum and energy. Combining everything together the phase space for $t\overline{t}$ events is

$$
\begin{aligned}
d\Phi_6 = \delta(E_{q_1} + E_{q_2} - \sum_{i=1}^{6} E_i) \;\; \delta(p^z_{q_1} + p^z_{q_2} - \sum_{i=1}^{6} p^z_i) \;\; \frac{d^3 \overrightarrow{p}_e}{(2\pi)^3 2E_e} \frac{d\rho_1}{(2\pi)^3 2E_\nu} \prod_{i=1}^{4} \frac{\rho_i^2 d\Omega_i}{(2\pi)^3 2E_i} \\
\times \frac{dm_1^2}{|2E_1 \frac{\rho_2}{E_2} - 2\rho_1 cos\theta_{12}|} \frac{dM_1^2}{|2E_1 \frac{\rho_3}{E_3} - 2\rho_1 cos\theta_{13} + 2E_2 \frac{\rho_3}{E_3} - 2\rho_2 cos\theta_{23}|} \\
\times \frac{dm_2^2}{|2E_e \frac{p^z_\nu}{E_\nu} - 2p^z_e|} \frac{dM_2^2}{|2E_e \frac{\rho_4}{E_4} - 2\rho_e cos\theta_{e4} + 2E_\nu \frac{\rho_4}{E_4} - 2\rho_\nu cos\theta_{\nu 4}|} \quad .
\end{aligned}
\tag{B.8}
$$

Bibliography

[1] CDF Collaboration, F. Abe et al., Phys. Rev. Lett. **74**, 2626 (1995).

[2] DØ Collaboration, S. Abachi et al., Phys. Rev. Lett. **74**, 2632 (1995).

[3] C. Quigg, "The State of The Standard Model", opening lecture at Conference on the Physics Potential and Development of Muon Colliders and Neutrino Factories, San Francisco, December 15-17, 1999, hep-ph/0001145.

[4] DØ Collaboration, B. Abbott et al., Phys. Rev. Lett. **80**, 2063 (1998).

[5] CDF Collaboration, F. Abe et al., Phys. Rev. Lett. **82**, 271 (1999).

[6] S. Willenbrock, Rev. Mod. Phys. **72**, 1141(2000).

[7] S. Abachi et al., Nucl. Inst. Methods **A338**, 2422 (1995).

[8] Leon M. Lederman, Scientific American, **264(3)**, 48, 1991.

[9] Helen T. Edwards, Ann. Rev. Nucl. Part. Sci., **35**, 605, 1985;

[10] FNAL, Design Report Tevatron I projects. FNAL internal note, 1984.

[11] FNAL, A Report of the Design of the Fermi National Accelerator Laboratory Superconducting Accelerator, FNAL internal note, 1979.

[12] M. P. Church and J. P. Mariner, Ann. Rev. Nucl. Part. Sci., **43**, 253, 1993.

[13] D. Mohl, G. Petrucci, L. Thorndahl and S. van der Merr, Phys. Rep., **C58**, 73, 1980.

[14] P. Rice-Evans, Spark, Streamer, Proportional and Drift Chambers, The Richelieu Press, London, 1974, Chap. 10.

[15] F. Sauli, CERN Report 77-09, 1977.

[16] F. Sauli in Experimental Techniques in High Energy Physics, edited by Thomas Ferbel (Addison-Wesley, 1987), p.79.

[17] A.R. Clark et al., Nucl. Instrum. Methods **315**, 193 (1992).

[18] A.R. Clark et al., Nucl. Instrum. Methods **279**, 243 (1989).

[19] R. Avery et al., IEEE Trans. Nucl. Sci. **NS-40**, 573 (1993)

[20] J. F. Detoeuf et al., Nucl. Instrum. Methods **A265**, 157 (1988); **A265**, 310 (1989).

[21] Particle Data Group, Phys. Rev. **D50**, 1173 (1994).

[22] S. J. Wimpenny et al., Nucl. Instrum. Methods **A279**, 107 (1989).

[23] M. Abolins et al., Nucl. Instrum. Methods **A280**, 36 (1989).

[24] C. Gerber et al, "Muon Momentun Determination", DØ Note 2140, 1994.

[25] DØ Collaboration, B. Abbott et al., Phys. Rev. D 60, 072002 (1999).

[26] M. Abolins et al., IEEE Trans. Nucl. Sci., **36(1)**, 384, 1989.

[27] M. Abolins, D. Edmunds, P. Laurens and B. Pi, Inst. Meth., **A289** 543, 1990.

[28] M. Abolins et al., "The Level One Framework", DØ Note 328; DØ Note 705 (1988), unpublised.

[29] D. Cutts et al., "Operation of the DØ Data Adquisition System; the new genetation" . Proceedings of the Conference on Computing in High-Energy Physics, Tsukuba, Japan, March 1991.

[30] J.T. Linnemann et al., "The DØ Software Trigger", Proceedings of the Conference on Computing in High-Energy Physics, Annecy, France, 1992. CERN 92-01.

[31] Adam Para et al., "The DØ Offline Production and Analysis", Proceedings of the Conference on Computing in High-Energy Physics, Annecy, France, 1992. CERN 92-01.

[32] R. Engelmann et al., Nucl. Inst. Meth., **A216** 45, 1983.

[33] M. Narain, "Electron Identificantion in the DØ Detector", Carl H. Albright et al. editors, "The Fermilab Meeting: DPF 92" **2** 1678, World Scientific, November 1992.

[34] M. Narain, "Electron Identification in the DØ Detector", DØ note 1584, 1992.

[35] Scott Snyder, Ph.D. thesis "Measurement of the Top Quark Mass at DØ" SUNY, Stony Brook (1995) unpublished.

[36] D.E. Groom et al., The European Physical Journal C 15, 1 (2000).

[37] H.T. Diehl and D. Hedin, "DØ Muon Level 2 Filter", DØ Note 1325, (1992).

[38] OPAL Collaboration, P.D. Acton et al., Z. Phys. C 58, 405 (1993).

[39] ALEPH, D. Buskulik et al., Z. Phys. C 57, 17 (1992)

[40] DELPHI Collaboration, P. Abreu et al., Z. Phys. C 53, 555 (1992).

[41] L3 Collaboration, O. Adriani er al., Phys. Lett. B 292, 463 (1992).

[42] Elvira, D. , "Jet Energy Scale at D0" D0 Note 3287 (2001), unpublished.

[43] F. Hsieh and H. Lan, "Post-CAFIX Jet Corrections For Top Mass Analyses", DØ Note 3055, 1996 (unpublished)

[44] F. Hsieh "Study of the Jet Energ Scale Using $\gamma + 1$ jet Events", DØ Note 3130, 1996 (unpublished).

[45] B. Abbott et al., Phys. Rev. D 58, 52001 (1998).

[46] M. Carena et al., Report of The Higgs Working Group - Physics at Run II Workshop, http://fnth37.fnal.gov/higgs.html

[47] B. Abbott et al., Phys. Rev. Letters 80, 2063 (1998).

[48] F.A. Berends, H. Kuijf, B. Tausk and W.T. Giele, Nucl. Phys. B 357, 32(1991).

[49] G. Mahlon, S. Parke, Phys. Lett. B 411, 133 (1997);
G. Mahlon, S. Parke, Phys. Rev. D 53, 4886 (1996).

[50] F.Canelli , J.Estrada and G. Gutierrez, DØ Note 3891 (2001), unpublised.

[51] G. Marchesini, B.R. Webber, G. Abbiendi, I.G. Knowles, M.H. Seymour and L. Stanco, Computer Phys. Commun. 67 (1992) 465

[52] F.A. Berends, H. Kuijf, B. Tausk and W.T. Giele, Nucl.Phys.B357:32-64,1991.

[53] J. Estrada and G. Gutierrez, DØ Note 3811 (2000).